Unravelling the photophysics of charge generation and transport processes by using ultrafast spectroscopic methods

DISSERTATION

zur Erlangung des Doktorgrades
an der Fakultät für Mathematik, Informatik und Naturwissenschaften
Fachbereich Chemie
der Universität Hamburg

vorgelegt von

Vandana Tiwari

Hamburg, Deutschland

October 2020

Abstract

Our world today is in an era of a great revolution in technology and stewardship to conserve our environment. One of the primary goals of our generation is to satisfy the exponentially increasing energy demands in an environmentally sustainable way for all to benefit. Even today, most of our requirements in terms of chemical energy (i.e. food) on this planet are generated by photosynthesis, which is fundamentally driven by series of elementary reactions performing initial charge separation after absorption of solar radiation. This process typically involves initial energy and electron transfers processes followed by charge separation leading to free charge carrier generation, which is used for chemical conversion and energy storage. Inspired by nature, an enormous number of materials, from complex molecular systems like polymers, to hybrid organic-inorganic systems like perovskites, have been designed to achieve efficient photovoltaic and photo-catalytic systems for capturing light energy and produce electricity and chemical energy, respectively. To gain direct control over the photo-induced charge generation process, a comprehensive understanding of the underlying elementary processes is imperative. This information can be obtained by clear spectroscopic identification of the involved molecular states as well as the dynamics of their inter-conversion, which will enable us to find the important molecular coordinate(s) in the relevant regions of the complex potential energy landscape. This thesis focuses on developing a detailed understanding of charge generation and transport

processes in natural and celebrated synthetic systems using ultrafast spectroscopic techniques: femtosecond transient absorption (TA) and two-dimensional electronic spectroscopy (2DES).

In isolated photosystem II (PSII) reaction center (RC), charge generation is a multiphasic process. I have extracted the time-components associated with each step by TA and 2DES at 20 K. In addition, I have distinctly captured the lifetime of the electronic coherence of the radial pair and the coherence between electron donor and acceptor at the initial step as 600 fs and 400 fs, respectively. The observed long-lived coherences are vibrational in nature. The functional role of coherent vibrations in charge generation is further explored in the most celebrated synthetic hybrid system of perovskite ($CH_3NH_3PbI_3$). With 2DES, I have solved the long-standing question in the field of perovskites, i.e, determined the role of organic cations in the performance of perovskite. The coherent vibrations in photoexcited perovskite reorients the organic cation, which acts like an electrostatic shield facilitating the stabilization of charges in the form of polaron. This process is one of the important factors leading to the high performance of these materials. To further advance our understanding of the transport of charges to their respective electrodes, I have studied prototypical doped polymeric systems, which are used as the electron transport layer between electrodes and photoactive layers. Employing 2DES, I capture the electronic coupling between the ion-pairs formed in the precursor solutions of molecular doped polymers, which is detrimental to the performance of the material with respect to charge generation and carrier transport. Additionally, I show that with systematic variation of side-chain in polymers, one can tune the strength of the coupling as well as population dynamics, which highlights the different nature of these interactions. I have also explored how different methods of preparation invoke different interaction amongst dopant and polymers ions. Finally, to understand the role of elementary photoinduced processes in photo-catalysis, I have studied the prototypical Cu(I)-based system for the role of

ligand pre-twisting in the preparation of photocatalytic triplet state. Using femtosecond broadband TA, I have resolved the excited state dynamics of the pre-distorted complex in single crystals. The lattice strain induced pre-twisting in the complex leads to faster relaxation followed by accelerated triplet generation.

The detailed understanding of ultrafast processes gathered in this thesis will pave the way towards developing a rational approach for designing and tuning materials for photovoltaic and photocatalytic application.

Kurzfassung

Unsere heutige Welt befindet sich in einer Ära der großen technologischen Revolution, die die Aufgabe hat, unsere Umgebung zu erhalten. Eines der Hauptziele unserer Generation ist es, den exponentiell steigenden Energiebedarf auf umweltverträgliche Weise zu decken, damit möglichst viele Lebewesen davon profitieren können. Noch heute wird die chemische Energie (d. H. Lebensmittel) auf diesem Planeten durch die Photosynthese erzeugt. Diese wird im Wesentlichen durch eine Reihe von Elementarreaktionen angetrieben, die nach Absorption der Sonnenstrahlung zunächst eine Ladungstrennung durchlaufen. Dieser Prozess beinhaltet zunächst Energie- und Elektronentransfer, die zur einer Erzeugung eines freien Ladungsträgers führen. Letzteres wird zur Umwandlung von Molekülen genutzt um so Energie zu speichern. Durch die Natur inspiriert wurde eine enorme Bandbreite an Materialien entwickelt, die von komplexen molekularen Systemen wie Polymeren bis hin zu hybriden organisch-anorganischen Systemen (z. B. Perowskite) reicht. Diese photovoltaische und photokatalytische Systeme erfassen das Sonnenlicht und produzieren Elektrizität bzw. chemischer Energie. Um eine direkte Kontrolle über den photoinduzierten Ladungserzeugungsprozess zu erlangen, ist ein umfassendes Verständnis der zugrunde liegenden Elementarprozesse unerlässlich. Diese Informationen können durch eindeutige spektroskopische Identifizierung der beteiligten Molekülzustände sowie durch die Dynamik ihrer gegenseitigen Umwandlung erhalten werden, wodurch wir die

wichtigen Molekülkoordinaten in den relevanten Regionen der komplexen potenziellen Energielandschaft finden können. Diese Arbeit konzentriert sich auf die Entwicklung eines detaillierten Verständnisses der Ladungserzeugungs- und Transportprozesse in natürlichen und bekannten synthetischen Systemen unter Verwendung ultraschneller spektroskopischer Techniken: Femtosekunden-Transientenabsorption (TA) und zwei-dimensionale elektronische Spektroskopie (2DES).

Im isolierten Reaktionszentrum (RZ) des Photosystems II ist die Ladungserzeugung ein mehrstufiger Prozess. In dieser Arbeit wurden die Zeitkomponenten dieses Prozesses durch TA und 2DES bei 20 K extrahiert. Außerdem habe ich die Lebensdauer der elektronischen Kohärenz des Radikalpaars und die Kohärenz zwischen Elektronendonor und Akzeptor in Anfangsschritten als 600 fs und 400 fs erfasst. Kohärenzen die eine höhere Lebensdauer haben sind an Vibrationsschwingungen gekoppelt. Die Rolle kohärenter Schwingungen bei der Ladungserzeugung wird beim weit verbreiteten synthetischen Hybridsystem von Perowskit untersucht ($CH_3NH_3PbI_3$). Mit 2DES habe ich die langjährige Frage auf dem Gebiet der Perowskite gelöst: Welche Rolle spielen die organische Kationen bei dem Wirkungsgrad von Perowskiten. Durch die kohärente Schwingungen in photoangeregtem Perowskit richten sich die organischen Kationen neu aus. Die Ausrichtung ermöglicht eine elektrostatische Abschirmung, die eine Stabilisierung von Ladungen, in Form von Polaron, gewährt. Dieser Prozess ist einer der wichtigsten Faktoren, der zu einer höheren Leistung dieser Materialien führt. Um unser Verständnis des Ladungstransports zu den Elektroden weiter zu verbessern, habe ich dotierte Polymersysteme, die als Elektronentransportschicht zwischen Elektroden und photoaktiven Schichten verwendet werden, untersucht. Mit 2DES fange ich die elektronische Kopplung zwischen den Ionenpaaren, die in den Vorläuferlösungen von dotierten Polymeren gebildet werden, ein. Dieser Prozess hat einen direkten Einfluss auf die Effizienz des Materials der Ladungserzeugung und des Ladungsträgertransports.Zusätzlich zeige ich, dass man mit systematischer Variation

der Seitenkette des Polymers, die Stärke der Kopplung sowie die Populationsdynamik eingestellt werden kann. Ich habe auch untersucht, wie verschiedene Herstellungsverfahren die Wechselwirkungen zwischen Fremdatomen und Polymerionen beinflussen. Um die Rolle elementarer photoinduzierter Prozesse bei der Photokatalyse zu verstehen, habe ich schließlich das prototypische Cu(I)-basierte System für die Rolle der Liganden bei der Herstellung des photokatalytischen Triplettzustands untersucht. Mit Breitband femtosekunden TA habe ich die Dynamik des angeregten Zustands des Cu(I)- Komplexes in einem Einkristallen aufgelöst. Durch die Gitterverformung induzierte Ligand-Verdrehung im Komplex führt zu einer schnelleren Relaxation, gefolgt von einer beschleunigten Bildung des Triplettzustandes.

Das detaillierte Verständnis der in dieser Arbeit gesammelten ultraschnellen Prozesse wird den Weg für die Entwicklung eines rationalen Ansatzes für das Entwerfen und Erstellen von Materialien für photovoltaische und photokatalytische Anwendungen ebnen.

Acknowledgments

Finally I got this opportunity, after five continuous years of hard work, to acknowledge the people who have helped me throughout. I would like to start by thanking Prof. R. J. D. Miller for ushering me to the PhD journey. Under his supervision I have successfully been able to submit my thesis. He introduced me to laser driven science world, which was a completely new field for me. He has been extremely patient to my naive questions and always understanding to my blank face during discussions. I am amazed with his command on the subject, which I can only hope to have some day. I would also like to thank Prof. U. Hahn for agreeing to supervise me and supporting me in all my troubles. I am filled with both, honor and gratitude, to thank them for their guidance.

My deepest gratitude goes to Dr. A. Jha for mentoring me throughout my PhD. He has been a mentor, a friend and a perfect lab partner to me. He has helped me transition from a trained synthetic chemist to an ultrafast spectroscopist. He introduced me to Dr. Duan who welcomed me to his 2D lab (now mine) and helped me get acquainted. Contrary to his nature Dr. Duan has always been very patient with me in lab. To be around such excellent mentors has contributed to my own development as a scientist.

I had a delightful PhD experience, all thanks to cheerful and helpful environment in my group. Somehow it was very easy to ask help from people in my group and

I never had any sort of disappointment. Special mention to Dr. F. Telkamp, Dr. V.I. Prokentyn, Dr. A. Mark, Mr. Andrey Krutilin, Dr. M. Katsiaflaka, Ms. Hyein Hwang, Dr. S. Azim, Dr. G. Singh and Dr. G. Chatterjee.

I would also like to extend my thanks to the IMPRS school for funding my PhD and MPSD for hosting my research. All department in MSPD like IT, Purchasing, HR, Health, etc. made life a lot easier. They made sure that at MPSD we should think about problem but science. I am also thankful to university of Hamburg for providing me the right platform to do my research.

I am also indebted to Prof. Arwen Pearson for allowing me to perform some experiments in her labs. Dr. Marta helped get things done easily and fast in her lab. In addition I would like thank my collaborators Dr. M. Throwart for his support in 2D data modelling, Dr. X. Lin for modelling our perovskite data, Dr. Dr. Pabitra Nayak and Dr. Henry Snaith for providing perovksites samples, Prof. Henning Sirringhaus and Dr. Ian Jacobs for helping with all doped polymer samples, Prof. Roberta Croce for reaction center samples, Dipl.-Chem. Christian Schmidt and Dr. Thomas Hackl for NMR data collection and processing.

PhD is very demanding and being so far from family and country becomes overwhelming ever now and then, but thanks to my friends I always came through. I would like to thank Dr. Garima Singh for forcing me to push my limits, like to be in clubs till morning, drink till you passsout, dance till your feet hurts, etc. She has always made me feel at home on this, completely, new land. Special mention to my friend Mrs. Tanu Shukla for constantly reminding my purpose of staying in Germany and setting my priorities straight. I am also thankful to my friend, Mr. Fernando A. Rodrigrez for adding a new dimension. I have known him for the shortest period of time but share a strong bond. This list cannot end without mentioning soon to be doctor Ms. Melby Johnny. She always have great stories to share and she is full of color.

Contents

List of Figures

xviii

xix

List of Tables

Chapter 1

Introduction

With the advancement in technologies and increase in the demand of energy by exploding human population, search for an abundant, reversible, and eco-friendly source of energy became inevitable. This drew the interest of researchers towards solar energy, a potential candidate considering the prevailing situation when our non-renewable energy sources are consumed at a much faster rate than the replenishing rate. If we can capture even a portion of solar energy available to us on earth and then convert it into useable form, our energy requirements can surely be actualized. To provide a quantitative picture, the amount of solar energy that reaches earth's surface is about 3×10^{24} J every year, which is equivalent to more than 1000 times the global energy consumption.[1] Therefore, we surely have enough energy to grab. Although, we would like to efficiently convert it into a more applicable form, such as heat, chemical or electrical energy. When it comes to trapping solar energy, photosynthesis has always been an inspiration. It refers to the process used by green plants and other photosynthetic organisms (called as photoautotrophs) to convert light energy into chemical energy, which in turn can be used by the organisms (heterotrophs) to fuel their activities. Therefore, it is essentially the solar energy, which is trapped

1

by photosynthesis process and then, is converted from one form to another while moving in the food chain. For over billions of years nature has employed photosynthesis to harvest and utilize solar energy continuously as the major source of energy for all life on earth. To execute the process, photoautotrophs contain photosynthetic systems, which are complex machineries performing manifold steps to ensure the charges generated by light absorption (i.e. photoinduced charge generation) are efficiently separated and transported to accomplish one of the most important and complex redox chemical reaction of water oxidation. This critical process produces the molecular oxygen we breathe and the food we eat. To perform these important and synthetically extremely challenging reactions in tandem, nature has designed efficient photosynthetic assemblies, which operate inside the thylakoid membranes of plants and cyanobacteria, see figure 1.1(a). In photosynthetic assemblies, different molecular systems are rationally placed such that all the involved chemical reactions are coupled to each other thermodynamically as well as kinetically. Hence, we can say, our nature is the most amazing chemist that perfectly knows how to design a system and integrate it with the necessary physical processes to perform the desired function. Thus, the understanding of natural photosynthetic processes has always been a broad and fascinating research topic in itself.

1.1   Natural to biomimetic systems

The natural photosynthetic machinery performing light dependent reactions can be broadly divided into three parts: (1) antenna complex, absorbs solar light and funnels the energy to the center; (2) reaction center complex, performs series of energy and charge transfer reactions and (3) catalytic center (OEC i.e. oxygen evolving complex, it is also the part of reaction center complex), performs water oxidation reaction,[2, 3] as shown in figure 1.1(a).
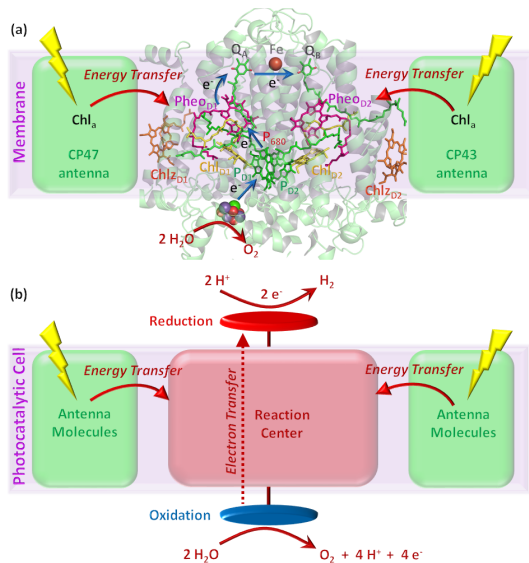
Figure 1.1: Schematic depicting chain of various energy and electron transfer pathways after light absorption in photosynthetic natural and biomimetic systems. (a) In natural systems, antenna complexes (shown here as chlorophyll binding proteins, CP47 and CP43) with broad absorption in visible region of light spectrum; (b) Simplified illustration of biomimetic systems to perform water oxidation process. It essentially has three parts: light absorbers (antenna molecules), charge generation sites (RC) and catalytic sites (oxidation and reduction). This assembly is called as photocatalytic assembly.

Photosynthetic machinery is extremely organized to unify complementary units. Every unit in the photosystems performs its specific function in a synchronous manner. Since the photosystems contains numerous complex molecular networks dec-

orated in active protein matrix, it is difficult as well as impractical to summarize specific details of each unit here. However, a coarse depiction of this natural assembly can surely provide the inspiration of how different functional units are assembled to perform the process of charge generation and its separation to perform catalysis. To summarize the overall machinery, a schematic representation is shown in figure 1.1(b). This schematic sketches the basic inspiration for designing the bioinspired molecular frameworks for solar light harvesting.[4–8] Essentially, to design any photocatalytic cell using molecular assemblies, three different molecular units with specific functions are needed. Light absorption unit, shown as antenna molecules in figure 1.1(b), should capture the solar light that reaches the earth surface, and hence, it needs to have absorption in broad spectral range with high absorption coefficient. The absorption unit should efficiently transfer the absorbed energy to next unit, i.e., charge generation unit, shown as reaction center in figure 1.1(b). At the charge, generation unit primary process of charge transfer and then their separation happen. The separated charges are then utilized at the redox catalytic centers to perform oxidation and reduction reactions. As can easily be envisaged, each molecular unit needs to perform different set of photophyscial or chemical processes. Thus, it is essential to develop a detailed understanding towards the physical and chemical processes employed by the nature to perform these specific functions.

1.2 Solar harvesting system: *different approaches*

As is clear from the above section, the objective behind studying natural systems is to understand the underlying operating mechanisms of solar energy conversion. The fundamental conclusions drawn from the nature can then be implemented to engineer artificial systems in laboratories having similar or better efficiency, which can be integrated in cost-effective devices operating with solar power. Broadly, there

are two ways by which solar energy can be harvested to power most of the needs of human kind:[9]

- Photovoltaics

- Photocatalysis

In photovoltaics, light absorption by photo-materials results into the generation of charges, which are transported in to the external circuit to perform electrical work. While in photocatalysis, photon energy is used to drive a chemical reaction.[10] It must be noted here that there are also other ways to capture solar energy, such as solar thermal (light to heat), photo-electrocatalysis (which can be performed using hybrid of photovoltaics and catalytic assembly) etc. In this thesis, I have kept the discussion limited to the photovoltaics and photocatalysis. Either way there are various fundamental processes, such as energy transfer, electron transfer, proton transfer, and proton-coupled electron transfer, which are involved to complete the overall process of energy conversion. The characteristic timescale for these underlying processes varies from femtoseconds (10^{-15} s) or picoseconds (10^{-12} s) to nanoseconds (10^{-9} s) or microseconds (10^{-6} s), or even longer. It is quite remarkable that all the solar conversion processes involve similar set of physical and chemical processes, it usually includes light absorption, charge generation, charge separation, and transportation. In addition, the processes providing hurdles in the path for efficient energy conversion are similar, like charge-trapping, recombination, and excited state relaxation losses. Therefore, assessment of photosystems (natural and prevailing synthetic systems) for these processes from electronic dynamics perspective will pave the way towards better understanding of solar light harvesting. In this thesis, I have focused on the evaluation of the key photoinduced electronic processes operating in in natural as well as emerging solar energy technologies, which are discussed in following sections.

1.3 Materials for charge generation

The quest for efficient charge generation materials has gathered enormous attention by chemists and material scientists. This quest involves testing the existing materials for charge generation properties, as well as developing new materials, although with limited rationale. The current generation of materials involves low-bandgap inorganic semiconductors, quantum dots, small molecular systems, as well as polymeric systems. Hybrid systems interfacing these different materials have also been very popular. There have been constant parallel efforts towards understanding and improving the charge generation efficiency from these different materials.

Molecular materials are a great alternative to natural system for studying photoinduced processes because they are less complex and provide great flexibility in terms of designing. A molecule should possess the fundamental property of absorbing photon and then, how to tune the molecular design for a specific process is just limited to human imagination. Although this imagination should be supplemented with the detailed perspective of the underlying process. In addition to design-flexibility, the molecular materials are equipped with other excellent advantages like solution-processability, large area fabrication, etc. The use and performance of these materials have been quite limited mainly because photodynamic parameters have not been fully explored yet, especially at ultrafast time scale, i.e., femtoseconds (10^{-15} s) to picoseconds (10^{-12} s). In order to replace the existing silicon-ruled commercial electronic market by organic materials, power conversion efficiency (PCE) of molecular materials needs to be improved.[11] To overcome all the limitations and to push the limits of existing molecular materials various studies have been done, both at fundamental and applied level. In the pursuit of efficient charge generation using molecular materials, two classes of systems have gained limelight: conjugated organic polymers and hybrid organic-inorganic perovskites.

1.3.1 Conjugated organic polymers

Organic semiconductors possess unique features that offers great advantages compared to inorganic semiconductors: 1) flexibility in design, which provides a handle for tuning the electronic properties; 2) large absorption coefficient required for making thin electronics, 3) less intrinsic defects, as they are composed of saturated electron system.[12–15] Due to these advantages, conjugated organic polymer based bulk-heterojunction (BHJ) solar cells have been one of the promising directions. A schematic of BHJ solar cell with various underlying photopysical processes is depicted in figure 1.2.

Conjugated organic polymers have intrinsically very low conductivity ($10^{-14}Scm^{-1}$) due to extremely low intrinsic charge carrier concentration (large band-gap in the range of 2-3 eV i.e. $E_g >> k_BT$, and hence no thermally activated charge carriers are available).[16] Similar to inorganic semiconductors, charge carrier concentration in organic systems can significantly be increased by doping resulting into higher conductivities ($> 10^3Scm^{-1}$).[17–20] Doping has enabled researchers to construct the conducting organic materials for efficient and cheaper electronic devices. For the realization and efficiency of organic based devices, a controlled and stable doping is required. There are various means by which doping can be achieved: metal, gases, or halides. However, small dopants tend to diffuse and form separate domains causing thermal instability. An alternative approach is to use similar molecule (aromatic) as dopant, which are compatible with the polymer moiety and therefore, molecular doped transport layer materials produce stable organic electronics.[14]

Organic semiconductors either donates an electron (p-type) from highest occupied molecular orbital (HOMO) to the lowest unoccupied molecular orbital (LUMO) of the dopant, as shown in figure 1.3(a), or accepts an electron from dopant as in n-type doping (figure 1.3(b)). In general, the principle of doping in organic semiconductors is
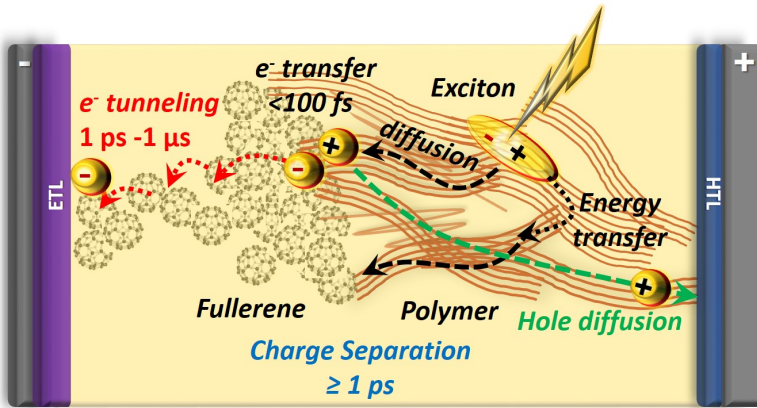
Figure 1.2: Schematic of processes triggered after photon absorption in bulk-heterojunction (BHJ) solar cell. The absorbed photons by polymers generate excitons that diffuse using various energy transfer pathway before they decay or perform charge transfer on interface with electron acceptor (fullerene). The charges may then separate and reach the respective electrodes via tunneling or diffusion. Here ETL refers to electron transport layer and HTL to hole transport layer.

similar to that of inorganic semiconductors: doping creates new defect states between the fundamental band-gap easing the charge generation process. Nature of charges generated, bound or free, varies and depends on the energetics of donor and acceptor pairs.[14, 21–23]

Molecular doping has shown promising results in improving the performance of organic electronics, especially organic light-emitting devices.[11] However, the fundamental understanding towards molecular doping is under debate. Important here is to address the cause of poor doping efficiency, i.e., the number of free charge carriers

8
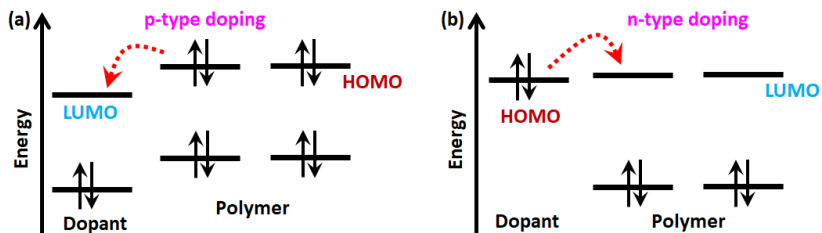
Figure 1.3: Energy diagram depicting the electronic states of dopant and polymer, which are involved in electron transfer: (a) p-type doping (electron is transferred from HOMO of the polymer to the LUMO of the dopant); (b) n-type doping (electron is transferred from HOMO of the dopant to the LUMO of the polymer). The polymer and dopant energy levels are arbitrarily chosen.

created per dopant molecule, organic semiconducting materials compared to inorganic counterparts.[21] To achieve substantial charge carriers, typical dopant concentrations used are of the order of 1-10 % in organic semiconductors. This effectively increases the intrinsic charge carrier concentration but has an adverse effect on mobility and external output. Therefore, it is imperative to achieve higher doping efficiency with lower dopant concentration. This requires the precise understanding towards the origin and strength of the dominating interactions in the course of the doping process.

1.3.2   Perovskites

Organic-inorganic perovskites are amongst the most successful materials for charge generation using photovoltaics.[24–27] On a laboratory scale, power conversion efficiencies (PCEs) of perovskite-based photovoltaic cells are already competing with those of conventional and well-established thin-film photovoltaic technologies.[28] These are described as hybrid materials because in addition to the three-dimensional inorganic

sublattice structure (consisting of metal and halides) they also have short chain organic cations like methylammonium[29] $(CH_3NH_3)^+$. This family of materials share a crystal structure of calcium titanate, ABX_3, as shown in figure 1.4. Perovskite based photovoltaics emerged as an innovation in the dye solar cell technology[30] and within a very short span of time became the "Champion" material for solution processed solar-cells.
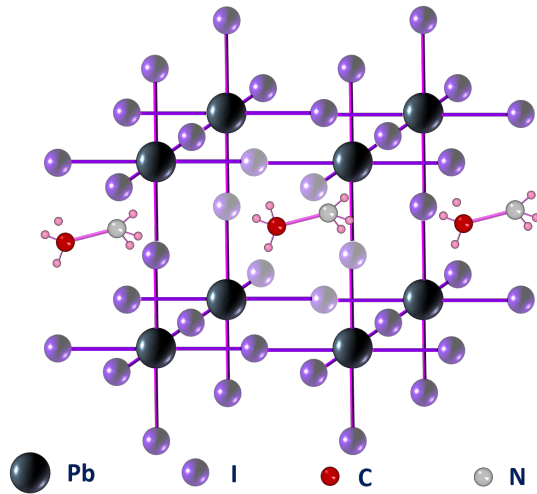
Figure 1.4: Crystal structure of hybrid organic-inorganic perovskite (ABX_3). Here, specific example of methylammonium lead iodide ($CH_3NH_3PbI_3$) has been depicted.

Perovskites have shattered the conventional belief that high crystallinity is required for high solar-conversion efficiency, as these materials have shown high solar cell performance with structural disorderness (polycrystallinity).[31] Globally researchers are trying to apprehend the origin of the high performance in MHPs but is far from being understood.[32, 33] Carrier cooling mechanism, nature of charge carriers, mid-

gap states, stability etc. are few interesting research directions.[34,35] In addition, the functional role of the organic cation and structural morphology has gathered enormous attention as well. Scientist have been in constant pursuit to have a thorough understanding of the photophysical processes occurring in perovskite to exploit these materials to their fullest potential and for large-scale commercial deployment.

1.4   Photocatalysis

Driving efficient photo-redox chemical transformations is a major challenge for solar-to-fuel conversion systems. General interest in this area remained a sideline until 1970s when oil crisis impelled researchers around the world to seek alternatives to conventional fossil fuels.[36] The profound concerns over environmental impacts by burning fossil fuels was another motivation.[37] During this period, several seminal work were report that propelled the field of solar-to-fuel conversion. First of these results was report on O_2 evolution on TiO_2 from the Bell Lab.[38] In another ground-breaking work by Fujishima and Honda, UV light induced H_2O oxidation over TiO_2 electrodes produced H_2 production.[39,40] This work is considered the stepping stone in the field of photocatalysis. The success of TiO_2 boosted the research towards finding the inorganic semiconductors to perform photocatalysis in the visible part of the solar spectrum.

In molecular systems, transition metal-complexes are the most popular materials for photocatalysis. Earth-abundant metal complexes based on iron and copper with their low- cost and non-toxicity, have recently been very attractive alternative to conventional rare elements like ruthenium and iridium-complexes as photocatalysts.[41-44] Iron has successfully been employed to design catalysts for various chemical reactions. Similarly, copper(I) based complexes have been recognized to present desirable photo-catalytic properties similar to popular ruthenium(II) based complexes. Greater
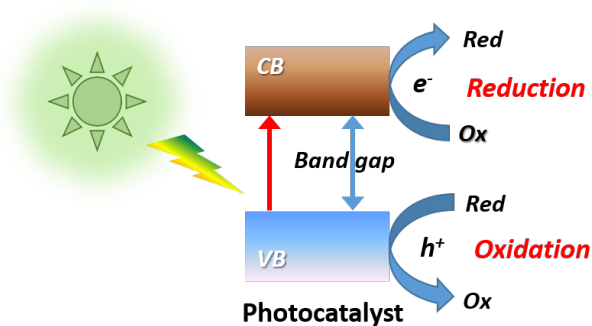
Figure 1.5: Cartoon describing the photocatalysis using excitonic systems. In molecular systems, valence band (VB) and conduction band (CB) are replaced by molecular electronic states.

abundance, lower toxicity, strong reducing power and long excited state lifetimes make it as an attractive alternative.

Understanding photo-induced charge-transfer reactions are vital for efficient photocatalysis and thus, both experimentalists as well as theoreticians have been trying to systematically formulate structure-reactivity correlations. In photoredox catalysis, charge-transfer process precedes the catalytic step and hence, is one of the key factors dictating the efficiency of catalytic conversions. To achieve direct control of photo-induced charge transfer process, detailed spectroscopic characterization of involved molecular states and the dynamics of their inter-conversion are imperative. Through such an exercise we would equip ourselves to focus on the relevant regions of the complex potential energy landscape and identify few important molecular coordinate(s).

1.5 Experimental techniques

As described in the earlier sections, photoinduced charge generation involves series of photo-chemical and physical processes occurring in different timescales (femto-to micro-seconds). To capture each process in real time, we need experimental techniques with time-resolution better than the respective processes to be captured. Thus, capturing processes that happens in ultrafast timescales (femto- to pico-seconds) had been extremely challenging in the past. With the advent of laser and following developments, it is now feasible to study chemistry happening in ultrafast timescale. The definition of term 'ultrafast' is not absolute but relative, and depends on the timescale of the processes, like solvent diffusion, relaxation, etc. In Chapter 2, I have briefly discussed the various photoinduced processes in molecular systems with their respective timescales. To investiage these processes in real time, various experiments with different light-matter interactions as probe have been designed. Figure 1.6 depicts the different constituent frequencies of the light that are used to probe specific molecular observables.

Time-resolved experiments rely on the principles already established through flash photolysis, an excitation pulse (pump) that initiates the chemical reaction and a delayed probe pulse to monitor the progress of the chemical reaction with time. In general, time-resolved measurement are performed using pump-probe scheme and is very versatile due to the availability of broad spectrum for pump and probe pulse. The frequency of pump pulse used for excitation is tuned to populate the respective higher energy level, called resonant excitation. The availability of ultrashort pulses in different frequency range has also made possible to pump as well as probe the different molecular parameters.

Ultrafast spectroscopic methods have been extensively used to study the photoinduced processes. I have summarized here few of the recent experimental works.
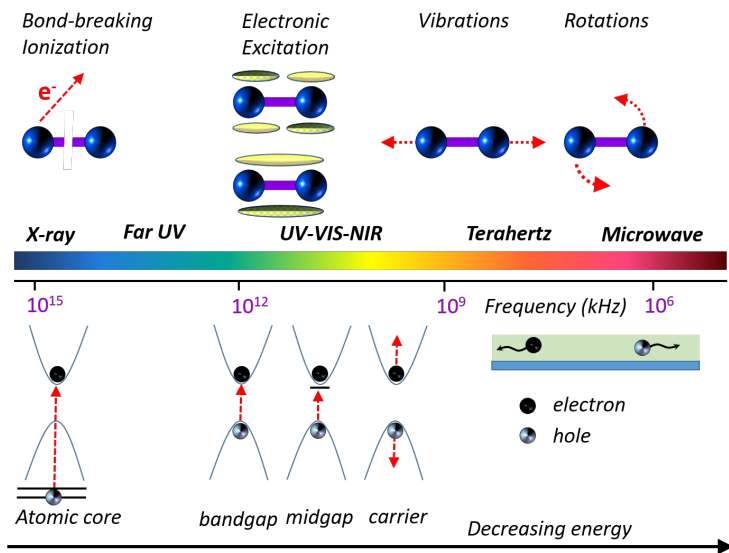
Figure 1.6: The electromagnetic spectrum showing different regions of interest in the context of molecular parameters that can be studied with the respective light-matter interactions.

Identifying the transient species, like ion pairs and exciplexes, is of prime importance. Infrared (IR) light is sensitive to molecular vibrations and time-resolved IR (TRIR) and Raman (TR) has been used widely to probe intermediates formed in many chemical reactions, like electron transfer. In a typical donor-acceptor complex (DAC) photoinduced charge generation process is followed by charge separation (CS) process. On the basis picosecond TRIR, formation of two distinct forms of ion pairs were proposed: i) tight ion par (TIP) generated by charge-transfer excitation of ground-state DACs, and ii) loose ion pair (LIP) formed by the bimolecular photoin-

duced CS. Apart from different decay dynamics in TIPs and LIPs, faster in former, they cannot be distinguished as the electronic spectra were essentially the same.[23] In order to access time-dependent structural dynamics, ultrashort pulses with energies up to hard X-rays are employed.[45] Femtosecond hard X-rays can be generated either by the method used in synchrotrons or by the technique used in X-ray free electron lasers (XFELs). Both technologies are excellent in their way to extract the structural dynamics of the system. The energies used in these kind of experiments are usually high as it involves extracting electron from core of the atom. Thus, their use are limited to mostly inorganic crystals.[46] First measurement highlighting the ability of high harmonic generation (HHG) has been published by Steve Leone group in 2017.[47] They used soft x-rays (XUV), as a probe, for accessing inner shell core orbitals to valence states transitions and followed the evolution of valence electronic structure during a photoinduced process. They employed UV pulse (4.8 ev) to initiate the ring opening process in 1,3-cyclohexadiene (CHD) and probe the course of reaction with XUV pulse, spanning the 230-310 ev region. Molecular crystals posses greater challenges because of the high structural complexity and lower damage thresholds, also they are larger in unit cell size. To solve the problem researchers employ electron source, which have higher cross section, to probe structural changes in molecular systems.[48] Ishikawa et al. (2015) have shown that how the high dimensional problems can be reduced to few selected key modes, which are couple to charge transfer.[49]

Time resolved studies in the "standard" range have been studied in depth over the past several decades. This makes them go-to experiment to study the dynamics of materials with solar energy conversion potential. The processes happening in attosecond regime have not been unraveled completely yet and therefore, attosecond spectroscopy is been actively developed. As such they are not been used to probe solar-conversion materials but for fundamental studies of atoms, solid states, etc. In addition, there are other new fields emerging for comprehensive understanding of

ultrafast dynamics like time-resolved single molecule spectroscopy and microscopy. They have enable us to extract vital information regarding the local electro-optical properties of material.[50–53]

The need of hour is to incorporate the information from several techniques for example, TRIR, X-ray absorption, electron-diffraction based techniques, and to complement information obtained with traditional transient absorption and emission studies in order to provide an absolute picture of the system. Today although spectroscopy is solving many enigmas, there are still some limitations associated with current techniques. To fill the gaps one need to model the system under study. In this work, all the mentioned theoretical modeling have been performed by my colleagues, which is mentioned specifically as it comes along. In summary, designing novel experimental and computational methods to unravel the detailed nature of the excitation and the dynamical interplay of excited states is imperative for conceptual leap in our understanding of the photophyscial processes.

1.6 Thesis outline

The goal of this work is to provide an acute picture of charge generation and transport processes in contemporary molecular systems. In order to do that I have formulated the thesis as follows:

Chapter 2 is completely focused to guide readers, briefly, to the science behind techniques that I have employed. A basic knowledge of quantum mechanics is given prior to explaining the after effects of light-matter interaction. Transient absorption and 2D electronic spectroscopy have been explained in details along with the set-up used in our lab.

As I described in the current chapter the process of light induced charge generation are inspired by nature, therefore, in Chapter 3 I have studied a biological system:

Reaction Center (RC) core complex. With broadband TA and 2D electronic spectroscopy, I have tried to trace the charge transfer pathway in RC at cryo temperature.

Chapter 4 includes study of charge generation in MHP at room temperature. In this chapter, I have specifically probed the perovskite photophysics for the role of organic cations during the polaron formation.

Chapter 5 is a detailed study of another important class of molecular material: molecular-doped polymers. I have revealed the fundamental reasons for their poor performance. In addition, I have systematically studied the dependence of electronic interaction on various factors like, side chain and processing conditions by 2D electronic spectroscopy.

Chapter 6 is a case study of pseudo Jahn-Teller distortion phenomena in Copper(I) complex, a prototypical photo-catalyst. I have compared the structural distortions following photoinduced charge transfer in copper complex for solution vs molecular crystal by femtosecond transient absorption spectroscopy.

In chapter 7 I have concluded the thesis by summarizing the novel findings and have explained the future directions to this work.

Chapter 2

Ultrafast spectroscopy: Theory and experiments

In this chapter, I have introduced the methods I used to study the charge transfer processes. In order to understand the techniques, a basic understanding of quantum mechanics and both, linear and nonlinear spectroscopy is mandatory. My attempt is not to give a comprehensive but general overview of these topics. Anyone without a prior understanding of the field should also be able appreciate the science explained in this thesis.

2.1   Quantum dynamics : an overview

The principal goal of any spectroscopic study is to understand the electronic properties of the material under study by probing the interaction-induced changes in the light field as a result of light-matter interaction. The amplitude of electromagnetic radiation used to perturb the system oscillates and the temporal envelope of the laser pulse evolves with time, time-dependent Schrödinger equation is used to describe the

Hamiltonian of the system interacting with light.[54]

2.1.1   Nonlinear Spectroscopy

Spectroscopy refers to the study of microscopic properties of matter using electromag-
netic radiation. The conventional spectroscopic techniques gives information about
the dynamical and structural properties of matter (chemical or biological). An spec-
troscopic study is called linear when the observable depends linearly on the intensity
of incident light field. In quantum language, it can be understood as *"one photon
in and one photon out"* experiments. Nonlinear spectroscopy, on the other hand,
refers to the study of field-matter interaction-induced signal which involves multiple
incident light fields separated by time delays. As a result one can correlate different
spectral features and disentangle complex spectra. The advancement in spectroscopic
techniques has enabled nonlinear spectroscopy to probe molecular dynamics and pho-
toinduced processes in broad spectrum range.[55]

The nonlinear spectroscopic techniques that I have employed for study uses op-
tical pulses to probe the structural and dynamical properties of matter.[54, 56–63] In
these techniques, multiple light fields coherently act on the sample and a macroscopic
oscillating polarization is generated which radiates signal. The signal is generated in
a specific phase-matching direction.[55, 64] In principle, all the optical properties of the
matter are associated with polarization which oscillates with same frequency as the
incoming field and can be given by:

$$P = P^{(1)} + P_{NL} \tag{2.1}$$

where $P^{(1)}$ is the linear polarization and P_{NL} is the nonlinear polarization. At intense
light fields χ itself depends on electric field (E) and thus the polarization is given as

power series of E.

$$P_{NL} = P^{(2)}(r,t) + P^{(3)}(r,t) + \cdots \tag{2.2}$$

$$\Rightarrow P(r,t) = \epsilon_0 \chi^{(1)} E(t) + \epsilon_0 \chi^{(2)} E^2(t) + \epsilon_0 \chi^{(3)} E^3(t) + \cdots \tag{2.3}$$

$$= \epsilon_0 \left(\chi^{(1)} E(t) + \chi^{(2)} E^2(t) + \chi^{(3)} E^3(t) + \cdots \right) \tag{2.4}$$

where $\chi^{(1)}$ is the linear susceptibility and can be described by linear polarization $P^{(1)}$, ϵ_0 is the permittivity of free space. $\chi^{(2)}$ and $\chi^{(3)}$ denote second- and third- order nonlinear susceptibility, respectively. This nonlinear relationship between polarization and electric field occurs only at strong field. These strong electric fields associated with the laser pulse start to scale with the existing field between charges constituting matter, like electrons and nuclei, modulating the optical properties of the material.[65] The electric field pulse can be described as:

$$E(r,t) = E(r)e^{-i\omega t} + c.c. = \sum_n E_n e^{-i\omega_n t} + c.c.$$
$$= \sum_n A_n e^{ik_n r - i\omega_n t} + c.c. \tag{2.5}$$

This can be incorporated into the polarization, $P^{(n)}(r,t)$ which will be give the following:

$$P^{(n)}(r,t) = \sum_n P_{(n)} e^{-i\omega_n t} + c.c. \tag{2.6}$$

where the summation extends over all the positive and negative frequencies (ω_n) The wavevector k_n and the frequency ω_n of incident fields describes the wavevector (k_{sig}) and the frequency (ω_{sig}) of the polarization which radiates signal. We can write the complex amplitudes of the nonlinear polarization by taking Fourier transform on $P^{(2)}(\omega_n)$ and $P^{(3)}(\omega_n)$:

$$P^{(2)}(\omega_{sig}) = \chi^{(2)}(\omega_{sig}; \omega_p, \omega_q) E(\omega_p) E(\omega_q) \tag{2.7}$$

$$P^{(3)}(\omega_{sig}) = \chi^{(3)}(\omega_{sig}; \omega_p, \omega_q, \omega_r) E(\omega_p) E(\omega_q) E(\omega_r) \tag{2.8}$$
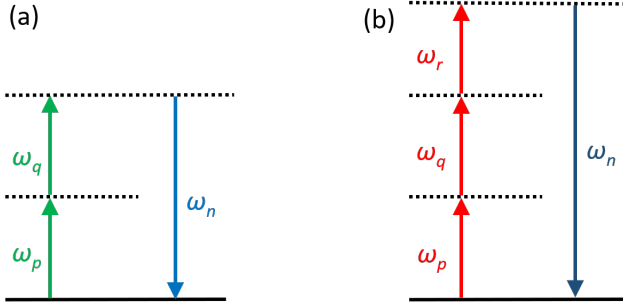
Figure 2.1: Illustration of nonlinear optical mixing process:(a) Sum-frequency generation $\chi^{(2)}$, (b) third harmonic generation $\chi^{(3)}$.

The second-order susceptibility $\chi^{(2)}$ gives rise to second order nonlinear responses in nonlinear optics (equations (2.9) to (2.11)).

$$P^{(2)}(2\omega) = \epsilon_0 \chi^{(2)}(2\omega; \omega, \omega)E(\omega)^2 \quad \text{(SHG)} \tag{2.9}$$

$$P^{(2)}(\omega_1 + \omega_2) = \epsilon_0 \chi^{(2)}(\omega_1 + \omega_2; \omega_1, \omega_2)E(\omega_1)E(\omega_2) \quad \text{(SFG)} \tag{2.10}$$

$$P^{(2)}(\omega_1 - \omega_2) = \epsilon_0 \chi^{(2)}(\omega_1 - \omega_2; \omega_1, \omega_2)E(\omega_1)E^*(\omega_2) \quad \text{(DFG)} \tag{2.11}$$

where SHG is second harmonic generation, SFG is sum frequency generation (figure 2.1(a)) and DFG is difference frequency generation process. In addition, optical parametric amplification (OPA) is also a second order nonlinear response. In OPA a pump (high intensity) pulse is mixed with another pulse called seed pulse in a nonlinear crystal and energy at ω_{signal} is amplified with remaining nonincident (ω_{idler}) field generated in different direction.[66]

$$\omega_{pump} = \omega_{signal} + \omega_{idler}$$

OPA is an amplification process where the energy from pump pulse is transferred and no new frequency is generated, unlike DFG and SFG. If the seed and pump pulses are
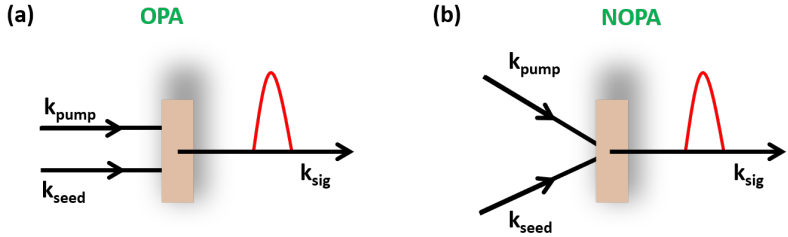
Figure 2.2: Graphical wavevector representation of (a)collinear (OPA) and (b) non-collinear configuration (NOPA).

aligned collinearly it is called optical parametric amplification process while in non-collinear geometry it is called non-collinear optical parametric amplification (NOPA) as shown in figure 2.2.

The third-order nonlinear optical susceptibility $\chi^{(3)}$ is the lowest nonlinear order response for centrosymmetric materials. The four-wave mixing techniques like TA and 2DES described later in this thesis are third-order nonlinear responses generated by $\chi^{(3)}$. Other processes includes third harmonic generation (THG) (figure 2.1(b)) and double quantum coherence. In multi-wave mixing the pulses interact with matter in a sequential fashion (figure 2.6) to generate signal in a particular direction.

2.1.2 Time-dependent perturbation theory

Strong pulses are employed to trigger nonlinear response in the material, but the changes invoked by the incoming electric fields should be weak as such it does not changes the material property. Therefore, the field-matter interaction can be treated by time-dependent perturbation theory which forms the basis of most theoretical

description of spectroscopy[67, 68]

$$\mathcal{H}(t) = \mathcal{H}_0 + \mathcal{H}'(t) \tag{2.12}$$

where $\mathcal{H}_0$ is the time-independent completely solvable Hamiltonian of the system and $\mathcal{H}'(t)$ is a time dependent Hamiltonian operator that describes the interaction between the light field and the matter. $\mathcal{H}'(t)$ is given by the dipole operator of the system and an external electric field interacting with the system:

$$\mathcal{H}'(t) = -E(t) \cdot \mu \tag{2.13}$$

The dipole operator is given by $\mu = \sum_a q_a(r - r_a)$, where a is the total number of nuclei and electrons, q_a are the charges, and r_a are the positions. This operator induces quantum transitions between any two different quantum states. The field used to cause perturbation are weak and therefore the nth-order perturbation theory will be used to describe the nonlinear signal derived from interacting with n electromagnetic fields.

The time evolution of the total Hamiltonian can be described in the density matrix formalism as:

$$\frac{\partial \rho}{\partial \hbar} = -\frac{i}{\hbar}\mathcal{H}\rho + \frac{i}{\hbar}\rho\mathcal{H} = -\frac{i}{\hbar}[\mathcal{H}, \rho] \tag{2.14}$$

equation (2.12) can be written as :

$$-\frac{i}{\hbar}[\mathcal{H}, \rho] = -\frac{i}{\hbar}[\mathcal{H}_0, \rho] - \frac{i}{\hbar}[\mathcal{H}', \rho] \tag{2.15}$$

where the time-dependence of the system is given by commutators.

Substituting the value of $\mathcal{H}'$ in equation (2.15) gives following:

$$-\frac{i}{\hbar}[\mathcal{H}, \rho] = -\frac{i}{\hbar}[\mathcal{H}_0, \rho] - \frac{i}{\hbar}E(t)[\mu, \rho] \tag{2.16}$$

Equation (2.16)) can also be written as:

$$\frac{\partial \rho}{\partial \hbar} = -\frac{i}{\hbar}\mathcal{H}_0\rho - \frac{i}{\hbar}\mathcal{H}'\rho \tag{2.17}$$

In interaction picture time-dependent wavefunction is given by:

$$|\psi(t)\rangle = U_0(t, t_0) |\psi_I(t)\rangle \tag{2.18}$$

where $U_0(t)$ is the time evolution operator with respect to $\mathcal{H}_0$ only and is given by:

$$U_0(t, t_0) = e^{-\frac{i}{\hbar}\mathcal{H}_0(t-t_0)} \tag{2.19}$$

Substituting the value of ψ into the Schrödinger equation:

$$-\frac{i}{\hbar}\mathcal{H} |\psi(t)\rangle = \frac{\partial}{\partial t} |\psi(t)\rangle \tag{2.20}$$

$$-\frac{i}{\hbar}\mathcal{H} \cdot U_0(t, t_0) |\psi_I(t)\rangle = \frac{\partial}{\partial t}(U_0(t, t_0) |\psi_I(t)\rangle)$$
$$= \left(\frac{\partial}{\partial t}U_0(t, t_0)\right) \cdot |\psi_I(t)\rangle + U_0(t, t_0)\left(\frac{\partial}{\partial t}\psi_I(t)\right) \tag{2.21}$$
$$= -\frac{i}{\hbar}\mathcal{H}_0 \cdot U_0(t, t_0) \cdot |\psi_I(t)\rangle + U_0(t, t_0) \cdot \left(\frac{\partial}{\partial t}\psi_I(t)\right)$$

Also $\mathcal{H}'(t) = \mathcal{H}(t) - \mathcal{H}_0$, therefore:

$$-\frac{i}{\hbar}\mathcal{H}'(t) \cdot U_0(t, t_0) |\psi_I(t)\rangle = U_0(t, t_0) \cdot \left(\frac{\partial}{\partial t}\psi_I(t)\right) \tag{2.22}$$

$$\Rightarrow \quad \frac{\partial}{\partial t} |\psi_I(t)\rangle = -\frac{i}{\hbar}\mathcal{H}'_I(t) |\psi(t)\rangle \tag{2.23}$$

where $\mathcal{H}'_I$ is the weak perturbation in the interaction picture and is defined as:

$$\mathcal{H}'_I = e^{-\frac{i}{\hbar}\mathcal{H}_0 \cdot (t-t_0)}\mathcal{H}'(t)e^{\frac{i}{\hbar}\mathcal{H}_0 \cdot (t-t_0)} \tag{2.24}$$

Similarly, the density matrix in the interaction picture can given by:

$$|\psi(t)\rangle \langle\psi(t)| = e^{-\frac{i}{\hbar}\mathcal{H}_0 \cdot (t-t_0)}|\psi(t)\rangle\langle\psi(t)|e^{\frac{i}{\hbar}\mathcal{H}_0 \cdot (t-t_0)} \tag{2.25}$$

$$\Rightarrow \quad \rho(t) = e^{-\frac{i}{\hbar}\mathcal{H}_0 \cdot (t-t_0)}\rho'(t)e^{\frac{i}{\hbar}\mathcal{H}_0 \cdot (t-t_0)} \tag{2.26}$$

Since the time evolution of wavefunction in interaction picture is equivalent to Schrödinger equation (section 2.1.2), same holds true for density matrix in the interaction picture:

$$\frac{\partial}{\partial t}\rho_I(t) = -\frac{i}{\hbar}[\mathcal{H}'_I(t), \rho_I(t)] \tag{2.27}$$

It's power expansion is given by:

$$\rho_I(t) = \rho_I(t_0) + \sum_{n=1}^{\infty} \left(-\frac{i}{\hbar}\right)^n \int_{t_0}^{t} d\tau_n \int_{t_0}^{\tau_n} d\tau_{n-1} \dots \int_{t_0}^{\tau_2} d\tau_1$$

$$[\mathcal{H}_I'(\tau_n), [\mathcal{H}_I'(\tau_{n-1}), \cdots [\mathcal{H}_I'(\tau_1)\rho_I(t_0)]\cdots]] \tag{2.28}$$

In can be written in Schrödinger picture as:

$$\rho(t) = \rho_I(t_0) + \sum_{n=1}^{\infty} \left(-\frac{i}{\hbar}\right)^n \int_{t_0}^{t} d\tau_n \int_{t_0}^{\tau_n} d\tau_{n-1} \dots \int_{t_0}^{\tau_2} d\tau_1$$

$$U_0(t,t_0) \cdot [\mathcal{H}_I'(\tau_n), [\mathcal{H}_I'(\tau_{n-1}), \cdots [\mathcal{H}_I'(\tau_1)\rho_I(t_0)]\cdots]] \cdot U_0^{\dagger}(t,t_0) \tag{2.29}$$

Where $\mathcal{H}_I'(t) = E(t) \cdot \mu$

and we get: $\rho(t) = \rho(0) + \sum_{n=1}^{\infty} \rho^{(n)}(t)$ When we assume that the $\rho(t_0)$ is an equilibrium density matrix and it does not evolve under the system Hamiltonian $\mathcal{H}_0$, we can write $t_0 \to -\infty$. For n^{th}-order density matrix is given by:

$$\rho^{(n)}(t) = \left(-\frac{i}{\hbar}\right)^n \int_{-\infty}^{t} d\tau_n \int_{-\infty}^{\tau_n} d\tau_{n-1} \dots \int_{-\infty}^{\tau_2} d\tau_1 E(\tau_n) E(\tau_{n-1}) \dots E(\tau_1) e^{-\frac{i}{\hbar}\mathcal{H}_0 \cdot (t-t_0)}$$

$$\left[\mu_I(\tau_n), \left[\mu_I(\tau_{n-1}), \dots \left[\mu_I(\tau_1), \rho(-\infty)\right]\cdots\right]\right] e^{\frac{i}{\hbar}\mathcal{H}_0 \cdot (t-t_0)} \tag{2.30}$$

Hence the dipole operator in the interaction picture is given as:

$$\mu_I(t) = U_0^{\dagger}(t,t_0)\mu U_0(t,t_0) \tag{2.31}$$

$$\rho^{(3)}(t) = \left(-\frac{i}{\hbar}\right)^3 \int_{t_0}^{t} d\tau_3 \int_{t_0}^{\tau_3} d\tau_2 \int_{t_0}^{\tau_2} d\tau_1 E(\tau_3) E(\tau_2) E(\tau_1) e^{-\frac{i}{\hbar}\mathcal{H}_0 \cdot (t-t_0)}$$

$$\left[\mu_I(\tau_3), \left[\mu_I(\tau_2), \left[\mu_I(\tau_1), \rho(t_0)\right]\right]\right] e^{\frac{i}{\hbar}\mathcal{H}_0 \cdot (t-t_0)} \tag{2.32}$$

In Schrödinger picture, μ is a time-independent but in interaction picture it is time-dependent since the system evolves in time under $\mathcal{H}_0$. The subscript I denoting interaction picture is commonly disregarded and distinguished from Schrödinger (μ)
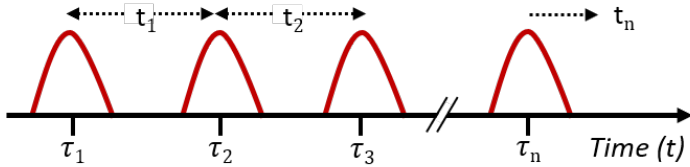
Figure 2.3: Illustration of pulse sequence in n^{th}-order nonlinear process.

by writing $\mu(t)$.

The high order time-dependent polarization is the macroscopic interaction-induced response to the incident light fields and is given by the expectation value of the dipole operator μ:

$$P(t) = Tr(\mu\rho(t)) \equiv \langle\mu\rho(t)\rangle \quad \Rightarrow \quad P^n(t) = \langle\mu\rho^n(t)\rangle \tag{2.33}$$

The 3rd- order polarization can be obtained by substituting the value of $\rho(t)$ in equation (2.33) which yields the following:

$$P^{(3)}(t) = \left(-\frac{i}{\hbar}\right)^3 \int_{-\infty}^{t} d\tau_3 \int_{-\infty}^{\tau_3} d\tau_2 \int_{-\infty}^{\tau_2} d\tau_1 E(\tau_3)E(\tau_2)E(\tau_1) \\ \left\langle \mu(\tau_3), \left[\mu(\tau_2), \left[\mu(\tau_1), \rho(-\infty)\right]\right]\right\rangle \tag{2.34}$$

The time variables can be also written in terms delays and are given as following:

$$\tau_1 = 0$$
$$t_1 = \tau_2 - \tau_1$$
$$t_2 = \tau_3 - \tau_2 \tag{2.35}$$
$$t_n = t - \tau_n$$

Here $\tau_1 = 0$ since the time-zero is arbitrary. Now, equation (2.34) can be expressed

26

in terms of time delays:

$$P^{(3)}(t) = \left(-\frac{i}{\hbar}\right)^3 \int_0^\infty dt_3 \int_0^\infty dt_2 \int_0^\infty dt_1$$

$$E(t - t_3)E(t - t_3 - t_2)E(t - t_3 - t_2 - t_1) \qquad (2.36)$$

$$\left\langle \mu(t_3 + t_2 + t_1), \left[\mu(t_2 + t_1), \left[\mu(t_1), \left[\mu(0), \rho(-\infty)\right]\right]\right]\right\rangle$$

The 3rd-order nonlinear response can be written as convolution of three electric fields:

$$P^{(3)}(t) = \left(-\frac{i}{\hbar}\right)^3 \int_0^\infty dt_3 \int_0^\infty dt_2 \int_0^\infty dt_1$$

$$E(t - t_3)E(t - t_3 - t_2)E(t - t_3 - t_2 - t_1) \cdot S(t_3, t_2, t_1) \qquad (2.37)$$

with 3rd-order nonlinear response function:

$$S^{(3)}(t_3, t_2, t_1) = \left(-\frac{i}{\hbar}\right)^3 \left\langle \mu(t_3 + t_2 + t_1), \left[\mu(t_2 + t_1), \left[\mu(t_1), \left[\mu(0), \rho(-\infty)\right]\right]\right]\right\rangle$$

$$(2.38)$$

The response function is defined for only positive times t_n only. Evaluation of the commutators for the nth-order nonlinear response function $(S^{(n)}(t_n, t_{n-1}, \cdots t_1))$ gives 2^n terms. Within these terms there are pairs of conjugate complex of each other. Therefore, it is sufficient to consider only 2^{n-1} terms. 2^n terms are obtained because the dipole operator acts on both, left (ket side) and right (bra side) of the density matrix operator.

In the next section we can see diagrammatic representation of 3rd-order nonlinear response function in the Liouville space.

2.1.3 Double sided Feynman diagrams

Following are the 3rd order nonlinear response we get:

$$\langle\mu(t_3+t_2+t_1)[\mu(t_2+t_1),[\mu(t_1,[\mu(0),\rho(-\infty)])]]\rangle =$$

$$+\langle\mu(t_3+t_2+t_1)\mu(t_2+t_1)\mu(t_1)\mu(0)\rho(-\infty)\rangle \qquad \Rightarrow \quad R_4$$

$$-\langle\mu(t_3+t_2+t_1)\mu(t_2+t_1)\mu(t_1)\rho(-\infty)\mu(0)\rangle \qquad \Rightarrow \quad R_1^*$$

$$-\langle\mu(t_3+t_2+t_1)\mu(t_2+t_1)\mu(0)\rho(-\infty)\mu(t_1)\rangle \qquad \Rightarrow \quad R_2^*$$

$$+\langle\mu(t_3+t_2+t_1)\mu(t_2+t_1)\rho(-\infty)\mu(0)\mu(t_1)\rangle \qquad \Rightarrow \quad R_3 \qquad (2.39)$$

$$-\langle\mu(t_3+t_2+t_1)\mu(t_1)\rho(-\infty)\mu(0)\mu(t_2+t_1)\rangle \qquad \Rightarrow \quad R_3^*$$

$$+\langle\mu(t_3+t_2+t_1)\mu(t_1)\rho(-\infty)\mu(0)\mu(t_2+t_1)\rangle \qquad \Rightarrow \quad R_2$$

$$+\langle\mu(t_3+t_2+t_1)\mu(0)\rho(-\infty)\mu(t_1)\mu(t_2+t_1)\rangle \qquad \Rightarrow \quad R_1$$

$$-\langle\mu(t_3+t_2+t_1)\rho(-\infty)\mu(0)\mu(t_1)\mu(t_2+t_1)\rangle \qquad \Rightarrow \quad R_4^*$$

where $R_1^*, R_2^*, R_3^*, R_4^*$ are conjugate complex of R_1, R_2, R_3, R_4, respectively. Diagrammatic representation is a simplified method of book-keeping of all the contributions to a particular nonlinear signal. It allows us to interpret the microscopic origin of a nonlinear signal with a particular frequency and wavevector of detection.

Double-sided Feynman diagram is the graphical representation of the field-matter interaction on the bra and ket side of the density matrix (ρ) with time-evolution in upward direction. An example showing double-sided Feynman diagram is presented in Figure 2.4. The vertical line represents the time evolution on the bra and ket side of the density matrix. Time is increasing from bottom to top direction. The arrows represents interaction with the light field. The right side denotes the interaction is on the bra side of the density matrix while the left side that of the ket. The first field- interaction causes the perturbation of the density matrix. After the third light-field interaction signal field is generated, which is different in character and therefore represented by dashed arrow. The arrows pointing in the right direction have an
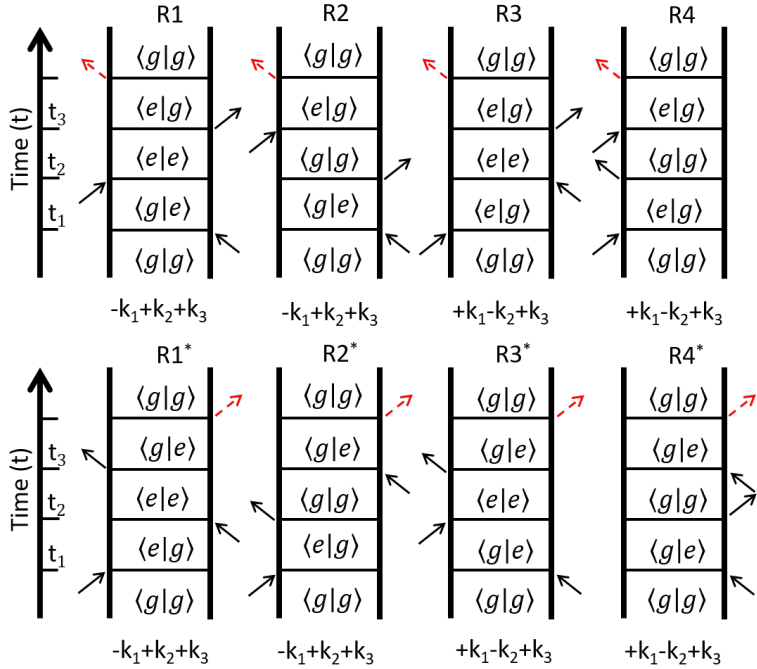
Figure 2.4: Diagrammatic representation of Double sided Feynman Diagram showing 3rd response in Liouville space.
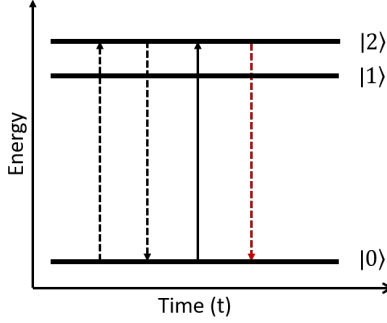
Figure 2.5: Representation of the Ladder diagram with pulse sequence indicating the incident laser fields and delay times.

electric field with $e^{-i\omega t + ikr}$ and the arrows pointing in the left direction have an electric field with $e^{+i\omega t - ikr}$. The arrows pointing towards the system and corresponds to absorption, while the arrows pointing away corresponds to emission. The system evolves freely under $\mathcal{H}_0$ between interactions. In every case the last interaction (signal) originates from Equation (2.33)

$P^n(t) = \langle \mu \rho^n(t) \rangle$

and represents emission of light from the non- equilibrium state, which results in the creation of population state.

Ladder diagrams are another way of keeping track of the contributions to a particular nonlinear signal, as shown in Figure 2.5. Here the energy states are given by horizontal lines arranged vertically. The time propagation of the field-matter interaction follows left to right on the x-axis. Vertical arrows corresponds to the absorption while downward arrows to the emission between the states. Solid lines indicates action on the ket side whereas dotted lines to the bra side.

30

2.1.4 Phase-matching

Third-order nonlinear spectroscopy, like TA and 2DES can be described by few or all eight correalation functions contributing to $S^{(3)}$ as shown by double-sided Feynman diagram[54,55] (figure 2.4).

$$S^{(3)} = \left(-\frac{i}{\hbar}\right)^3 \sum_{a=1}^{4} [R_a - R_a^*]$$ (2.40)

With diagrammatic representation we saw how the sequence of input fields dictate the frequency (ω_{sig}) and direction (k_{sig}) of the radiated signal field:

$$\omega_{sig} = \sum_n \pm\omega_n$$ (2.41)

$$k_{sig} = \sum_n \pm k_n$$ (2.42)

Therefore, it is important to select a perfect phase matching condition for a valid Liouville space pathways. For 2D photon echo spectroscopy the incoming incidents fields generates signal field in two directions: *rephasing* pathway and the echo signal (mirror images) in *nonrephasing* direction, when the phase matched condition is satisfied. In figure 2.4 R1, R2 and their complex conjugates $R1^*$, $R2^*$ are emitted in rephasing direction while R3, R4, $R3^*$, $R4^*$ are radiated in nonrephasing direction. For rephasing pathways:

$$\omega_{sig} = -\omega_1 + \omega_2 + \omega_3$$ (2.43)

$$k_{sig} = -k_1 + k_2 + k_3$$ (2.44)

and for nonrephasing pathways:

$$\omega_{sig} = +\omega_1 - \omega_2 + \omega_3$$ (2.45)

$$k_{sig} = +k_1 - k_2 + k_3$$ (2.46)

The four independent correlation functions generated in 2DPS can be summarized
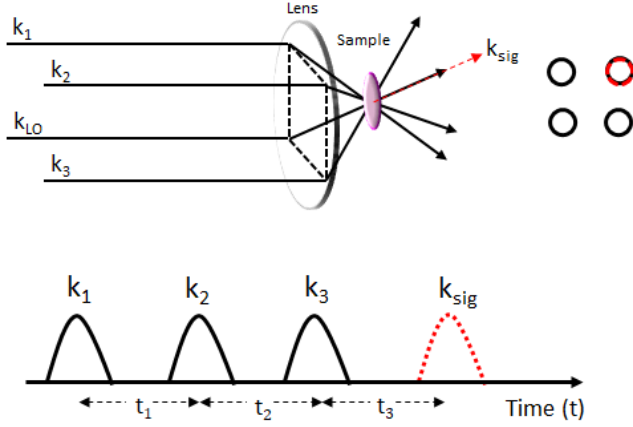
Figure 2.6: Figure showing phasing matching in 2DES with pulses aligned in BOX-CAR geometry. In heterodyne detection the signal is generated in the same direction as the LO.

Response	ω_{sig}	k_{sig}	τ_2 population
$R1$	$-\omega_1 + \omega_2 + \omega_3$	$-k_1 + k_2 + k_3$	excited state
$R2$	$-\omega_1 + \omega_2 + \omega_3$	$-k_1 + k_2 + k_3$	ground state
$R3$	$+\omega_1 - \omega_2 + \omega_3$	$+k_1 - k_2 + k_3$	excited state
$R4$	$+\omega_1 - \omega_2 + \omega_3$	$+k_1 - k_2 + k_3$	ground state

Table 2.1: Summary of phase matching condition for various 3rd-order nonlinear signal generated in 2DPE spectroscopy.
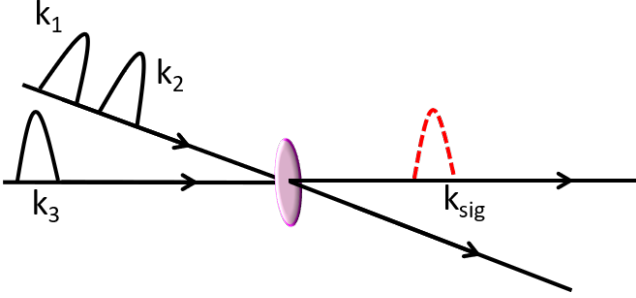
Figure 2.7: Phase-matching configuration for TA spectroscopy.

as: The aborptive 2D spectra is given by sum of the rephasing photon echo and nonrephasing spectra:

$$R(t_3, t_2, t_2) = Re[R^R(t_3, t_2, t_2) + R^{NR}(t_3, t_2, t_2)] \tag{2.47}$$

In our lab we have employed BOXCAR geometry, as shown in figure 2.6, to collect the 2DPE spectra and therefore we are able to collect the absorptive spectra and rephasing and nonrephasing spectra as well. For TA spectroscopy following are the frequency and wavevector conditions:

$$\omega_{sig} = \pm\omega_1 \mp \omega_2 + \omega_3 \tag{2.48}$$

$$k_{sig} = \pm k_1 \mp k_2 + k_3 \tag{2.49}$$

In TA spectroscopy the 3rd-order nonlinear signal is generated in the same direction as the probe (figure 2.7).

2.2 Photophysics

When a molecule absorbs electromagnetic radiation (photon), it gets promoted to higher energy states. Depending on the energy difference between ground energy state and excited energy state, called band gap energy, molecules can absorb radiations from different part of the electromagnetic spectrum. After absorption of radiation (UV/Vis), molecules get pumped with great amount of energy, which is many fold greater than the room temperature energy ($k_B T$). Therefore, the molecules redistribute its excess energy within it's own degrees of freedom or to the surrounding (bath), in order to reach the thermal equilibrium.[69]

Understanding of photophysical processes requires a prior knowledge of molecule's electronic structure, which gives information about the energies of state. Total energy of the system can be calculated by employing time-independent Schrodinger's equation:

$$\mathcal{H}\Psi(r, R) = E\Psi(r, R) \tag{2.50}$$

where $\Psi(r; R)$ is the total molecular wave function, r and R represent the coordinates of all electrons and nuclei, respectively. E is the energy and H is Hamiltonian of the system, which is defined as

$$\mathcal{H} = T_N + T_e + U_{ee} + U_{NN} + U_{Ne} \tag{2.51}$$

The first two terms in eqn. (2.2) are kinetic operators for nuclei and electrons, respectively. The last three terms in the equation corresponds to the potential energy operator for Columbic interaction (attraction and repulsion) between electrons with electrons, nuclei with nuclei, nuclei with electrons, respectively.

For a general system composed of m electrons and n nuclei we need to solve the full Schrodinger equation for $3\times(m + n)$ degrees of freedom. Therefore, for larger system (more then two electrons) solving equation (2.50) quickly becomes obstinate.

However, there is some approximation which when applied could help us solve the Schrodinger equation for multi-electron system. This is called Born-Oppenheimer Approximation (BOA).[70,71] It essentially takes into account the large mass difference between electrons and nuclei. Consider an electron and a proton both having the same kinetic energy now, since $T = \frac{1}{2}mv^2$ for equal energies electron is moving 43 times faster than the proton. Such a huge difference in speeds suggests that the electrons can respond almost instantaneously for a particular nuclear displacement. Therefore, instead of trying to solve the Schrodinger equation for all the particles simultaneously, we consider the nuclei to be fixed in position and solve the Schrodinger equation for the electrons at that particular nuclear arrangement. As a consequence, the total molecular wave function can be separated into electronic and nuclear part:

$$\Psi(r, R) = \chi_N(R)\psi_e(r; R) \tag{2.52}$$

where χ_N represents the nuclear wave function and ψ_e electronic wave function. Here electronic component depends on the co-ordinates of electron (r) and parameterically on the nuclear co-ordinates (R) as well. This means that the electronic wave function needs to be solved for each nuclear configuration. As a result of BOA, Hamiltonian of the system can now be written as

$$\mathcal{H}\psi_e(r, R) = E(R)\psi_e(r; R) \tag{2.53}$$

The electronic eigenfunctions are calculated for a fixed nuclear position and calculations is repeated for diferent nuclear arrangements. The curve obtained is energy as a function of inter-nuclear distance, called *potential energy surface* (PES). An extension to BO separation is Frank-Condon principle. Large disparity in masses causes an electronic transition to occur within a stationary nuclear framework. As such the nuclei are frozen during actual transition, but reorganizes once the electrons have adopted their final distribution. Now, since the overall probability of the electronic

transition is governed by the overlap of the nuclear wave functions on the two electronic states, the electronic transition will not occur from ground vibrational level of the ground electronic state to the ground vibrational level of the excited electronic state.

2.2.1 Photophysical pathways

When a molecule absorbs light radiation, it acquires new states which has a finite lifetime. The processes a molecule undergoes after excitation are explained conveniently with reference to a generic energy level scheme called Jablonski diagram,[69] as shown in figure 2.8.

Generally, a molecule is found in its electronic ground state, at room temperature, which is usually a closed-shell singlet, that is, total spin is zero, denoted by S_0. Often the vibrational modes of the molecule are also in their ground states. Light absorption promotes the molecule to higher energy electronic states, assuming that the photon energy chosen is in resonance with energy gap between ground and excited energy state (here S_0 to S_2). Here I would like to mention that electronic states are not well separated as in the figure shown. For the sake of convenience, such explanation is chosen, as it would help readers understand the concept.

Following absorption there are various options (pathways) available to the molecule for releasing the excess energy. We will focus on the most probable ones. One process that tops the list is **intramolecular vibrational relaxation** (IVR). This a non-radiative fast process whereby a molecule remains in its electronic state (here S_2) but *redistributes* its vibrational energy from initially excited mode (hot states) to other vibrational modes and/or *relaxes* by dropping to ground vibrational level (called **vibrational relaxation**, VR), by dumping energy to the environment.

Another ultrafast process that immediately follows or competes with IVR is **in-**
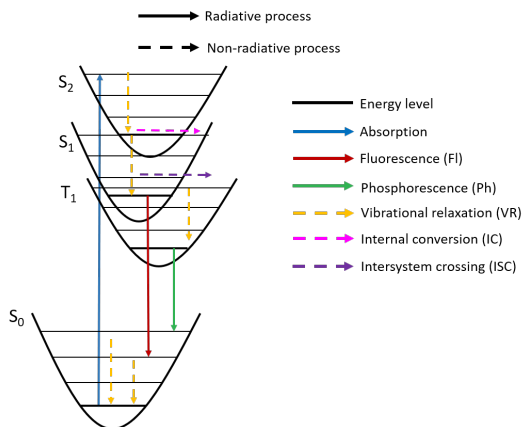
Figure 2.8: Jablonski diagram showing different photophysical pathways.

ternal conversion (IC), also a non-radiative process. Under this process a transition occurs between electronic states. In accordance with energy conversion law, the transition occurs from low vibrational levels of S_2 to higher vibrational levels of S_1 that have same total energy. Now the molecule can again undergo IVR, which will lead to thermal distribution of vibrational levels of S_1. At this point, there is a possibility of another IC to highly excited vibrational levels of S_0, but such processes are usually much slower than S_2 to S_1 internal conversion because the energy separation between S_0 andS_1 is much greater than between S_1 and S_2.

As a result there are other processes competing the relatively slow S_1 to S_0 internal conversion. One of these is **fluorescence**. The rate for this radiative process is usually much faster than non-radiative internal conversion S_1 to S_0 rate, which makes fluorescence more favored pathway for giving away the excess energy. Lifetime of a molecule in S_2 is not long enough to undergo fluorescence. As explained by **Kasha's rule**: essentially all of the fluorescence originates from S_1, irrespective to

Process	Timescales
IVR	10^{-15}
VR	10^{-12}
IC	10^{-15} - 10^{-12}
Fluorescence	10^{-09} - 10^{-07}
Phosphorescence	10^{-06}

Table 2.2: Timescale of various photophysical processes.

the initial excited state.[72]

Another pathway available from S_1 is triplet excited state(a state in which two electrons have parallel spin). As per selection rule these are spin forbidden transition, since the spin multiplicity is different, therefore are referred as weak transitions. A non-radiative transition between electronic states of different spin multiplicity is called **intersystem crossing** (ISC).This process The yield and timescale of this transition vary greatly and depends on the strength of spin-orbit coupling. Under this mechanism, a molecule depopulates from ground vibrational level of S_1 state to excited vibrational level of T_1 state. Once the system reaches thermal vibrational distribution in T_1, further relaxation back to S_0 can occur non-radiatively via another intersystem crossing. Alternatively, it may occur radiatively through **phosphorescence**.[73] The timescales of these photophysical processes have been given in Section 2.2.1.

Finally, there are number of other processes that occur in some molecules. Non-radiative processes that converts the original molecule to a completely different chemical species are known as **photochemistry**. Also, electron transfer processes, where a molecules de-excites by transferring energy to another molecule, detail of this process will be discussed later.

2.3 Transient absorption spectroscopy

It is one of the most conventional nonlinear spectroscopy,[74,75] it involves two light fields. One beam is used to excite the system to higher (excited) energy level, called pump beam, while the second beam is used as a probe. The time delay between pump and probe beam maps out the excited state dynamics. It is very a conventional but a potent technique to study the chemical reaction dynamics.Transient absorption signal is a third-order nonlinear response arising from three time-ordered interaction with incident field of the sample, two pump interactions and one probe interaction. A schematic of transient absorption set-up is shown in figure 2.10. Pump pulse used in experiments are generally in resonance with the absorption of the sample. A weak intensity white light continuum is used as probe in the TA set-up, this is to ensure there is no multi-photon absorption and the excited state population remains undisturbed.

Experimentally, a transient absorption signal is obtained by measuring the optical density (OD) of the sample after interaction with the pump laser, OD_{ON}, corresponding to the absorption of the sample in the excited state minus the absorption spectrum of the sample in the ground state, OD_{OFF}.

$$\Delta A = OD_{ON} - OD_{OFF} \tag{2.54}$$

$$= -log\frac{I_{ON}}{I_{OFF}} \tag{2.55}$$

where, I_{OFF} and I_{ON} are intensities of probe beam before and after pump beam interaction. A transient absorption spectrum can be obtained by plotting differential optical density as a function of wavelengths and time delay $(\Delta A(\lambda, \tau))$. Kinetic information is extracted from the spectrum by taking a trace along delay time, while trace along wavelength gives out transient absorption spectrum.
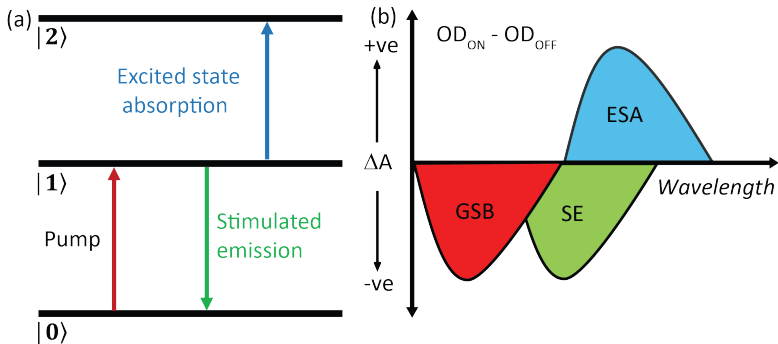
Figure 2.9: Cartoon representation: (a) Transitions in pump-probe spectroscopy, where $0 \rightarrow 1$ and $1 \rightarrow 2$ transitions are in resonance with the probe pulse and can have different frequency (b) Signals in 2D spectrum: ESA corresponds to excited state absorption, SE and GSB corresponds to stimulated and ground state bleach signal, respectively.

Transient absorption signal is a convolution of various different signals, distinguished by the region of appearance and sign of the signal. Figure 2.9 shows all the possible signals which might appear in a TA spectrum. Positive signal refers to increase in ΔA while negative signal means decrease in ΔA. In order to comprehend the spectrum it is imperative to understand first, the origin as well as the nature of the photophysical processes generating signals in a TA spectrum.

Ground state bleach (GSB): Upon photoexcitation, the fraction of molecules (0.1 to 10 %) from ground state to higher energy states. Thus, probe encounters less population after pump compared to population without pump. i.e., $OD_{ON} < OD_{OFF}$. As result a negative signal in the (ΔA) spectrum is observed in the wavelength region

of ground state absorption of the molecule under study.

Excited state absorption (ESA): After excitation by the pump beam, the system can also absorb energy from certain region of the probe spectrum to reach even higher optically allowed energy levels. This results in low transmittance of the probe beam at wavelengths resonant to the excited state transition, that is, $OD_{ON} > OD_{OFF}$. Therefore, ESA signals appears as a positive signal in the TA spectrum. Any excited state process can, principally, be monitored by observing the spectral evolution of ESA features corresponding to different excited states. In case of photo-product formation, within the timescale of measurements, a positive feature is observed that may not decay if the lifetime is long enough.

Stimulated emission (SE): As discussed earlier, an excited molecule can radiatively or non-radiatively decay to a lower energy level by a process known as spontaneous emission. However, interaction of the probe beam with molecule in the excited state can also result into stimulated emission from optically allowed transitions. The emitted photon in SE travels in the same direction as the probe beam leading to an increase in the number of photons impinging on the detector. As a result, it appears as a negative signal in a TA spectrum ($OD_{ON} < OD_{OFF}$). SE signal can be used to interpret relaxation processes in the system under study, but mostly is overlapped with the GSB (discussed above) which makes it difficult to observe.

In addition, there is a fourth possible contribution to the TA spectrum, called product absorption. Following excitation of the system by light, reaction may occur that results into another state, like triplet state. Absorption by such a transient product appear as a positive signal in the TA spectrum.

2.3.1   Transient absorption set-up

Ultrashort coherent pulses used in transient absorption measurements were generated using a commercial femtosecond laser, PHAROS, by Light conversion. It is Nd based laser system and the wavelength of output beam is 1030 nm. Temporal resolution of the pulse coming out of this laser system is 190 fs with 1000 mW output power at 1 kHz repetition rate. The laser beam was soon divided in two parts by a flip mirror. One side of the laser table has been used to develop transient absorption set-up while the other side for 2D set-up.

A schematic of the transient set-up is shown in figure 2.10. The fundamental beam from the laser, 1030 nm, was divided into two beams by a 80:20 beam splitter (BS1), The major portion of the beam (80%) was used to generate pump line while the minor portion (20%) of the beam was used to generate probe beam.

The probe beam was reflected by dielectric mirrors (DM) and guided by many mirrors (M) before focusing onto a YAG crystal by a convex lens (L1) ($f = 30$ mm) to generate a white light (WL) continuum. Before lens an attenuator (neutral density filter) is placed to control the energy of while the spot size of beam on the crystal is controlled by the translational stage onto which the lens in mounted. The spectrum of supercontinuum generated is shown in figure 2.11 . WL generation is a high order nonlinear process and therfore, requires stability to have less shot to shot variation and high signal to noise (S/N) ratio. To ensure this an aperture is placed before lens (L1) to cut off all the noises, in addition to power and spot-size optimization. The dispersed beam is then collimated by another lens (L2), focal length 20 mm, which is then focussed onto the sample by an off-axis parabolic mirror (OPAM, focal length, $f = 200$ mm).

For the pump beam generation, fundamental beam was first passed through a half waveplate (WP2), to change the polarization direction of light, which then passes
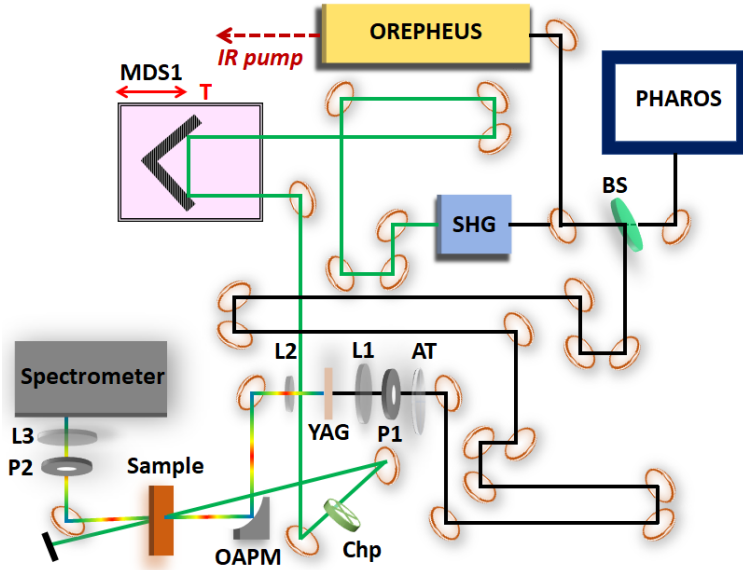
Figure 2.10: Schematic representation of transient absorption set-up in Dwayne Miller's group in Hamburg. Here AT is atteneuator, MDS is motorized delay stage, BS is beam splitter, L is lens, P is pinhole, Chp is chopper, SHG refers to second harmonic generation process.

through a type I BBO crystal (23.4°) for second harmonic generation (SHG). SHG generates 515 nm pulse which is then reflected by dielectric mirrors to get rid of 1030 residual and guided to a computer controlled mechanical delay line (RR, travel length, 30 cm).This is create the delay between pump and probe pulses. The beam is then focused on the sample by convex lens ($f = 400$ mm). Power of pump beam is attenuated by neutral density filters to achieve optimum photons density on the sample.
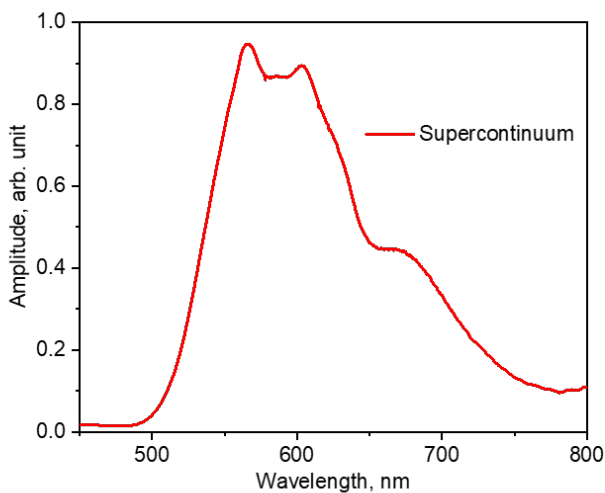
Figure 2.11: Graphical representation of supercontinuum used in transient absorption measurement.

2.3.2 Experimental procedure

For experiments it is made sure that pathlength of both beams are matched. Once that criteria is achieved the spot sizes are measured at sample (solution and film in this thesis). The general rule of thumb is to have pump beam twice the size of probe beam. The spot sizes were calculated by placing apertures of known sizes in the beam path and recording the transmitted intensity of beam using power meter. The full width half maxima (FWHM) beam sizes (in μm) were calculated using the following formulae:

$$w = \sqrt{\frac{2r^2}{\ln(\frac{1}{1-T})}} \qquad (2.56)$$

and

$$spotsize(FWHM) = [w\sqrt{2\ln 2}] \times 10^6 \qquad (2.57)$$

where r is the radius of the apertures in μ and T is the transmittance through the aperture ($T = \frac{I}{I_0}$, I_0 is intensity of unattenuated beam and I is the intensity of beam after passing through pinhole, respectively). The beam sizes at the sample were calculated to be $200\,\mu m$ for pump beam and $100\,\mu m$ for probe beam.

After passing through sample unabsorbed pump beam is blocked while the probe is directed towards a spectrometer (Sciencetech) model 9055 and a high-sensitive CCD linear array camera (EntwicklungsburoStresing). Before entering the spectrograph the first collimated and then focussed with lens. The focussed beams enters the spectrograph through a slit and then dispersed by grating onto a 1D array camera (1 *times* 2068 pixels).

The data acquisition (DAQ) was controlled by a LABVIEW software, developed by Dr. Friedjof Tellkamp. To collect the transient absorption signals, the pump beam (1 KHz repetition rate that means pulses are coming every 1 ms) before reaching the sample, is passed through a mechanical chopper (w/2) which is synchronized to the laser output to block every other pump pulse. Thus, for fixed time delay between pump and probe beam, white light continuum probe pulses encounter pumped (pump on) and unpumped (pump off) samples consequently.

For acquiring a transient data probe pulse is screened for a time period both before and after pump pulse. The probe signal recorded before pump is referred as negative time delays while after pump pulse is called positive time delays. The time at which both pump and probe pulse is matched is called time-zero (T_0). Time-zero is the

onset of a photo induced physical process. A schematic representation of different time delay is shown in figure 2.12.
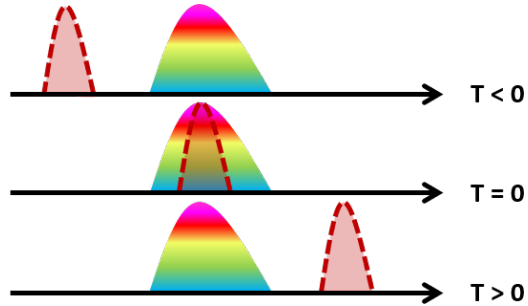
Figure 2.12: Diagrammatic representation of different time delays between pump and probe in transient spectroscopy. The arrow is in the direction of time. Time at which pump pulse overlaps with the probe pulse is defined as time zero T_0.

2.3.3   Temporal resolution

Temporal resolution (also called instrument response function, IRF) is measured by cross correlation experiment.[64] A schematic of this experiment is shown in figure 2.13. To perform this experiment, a pair of polarizer and analyzer (cross-polarizer) is placed in pump and probe path, respectively. The polarization of analyzer, placed after the sample, is selected as such the probe gets completely extinguished. When pump and probe pulses are temporally and spatially overlapped on an substrate, like quartz, the polarization of probe beam is modulated due to birefringence induced by the pump field, as shown in figure 2.13. This process of probe beam rotation polarization occurs only when both pulses (pump and probe) are temporally and spatially overlapped. For broadband probe, cross-correlation signals for every wavelength in the continuum

46

are generated as a function of pump delay.
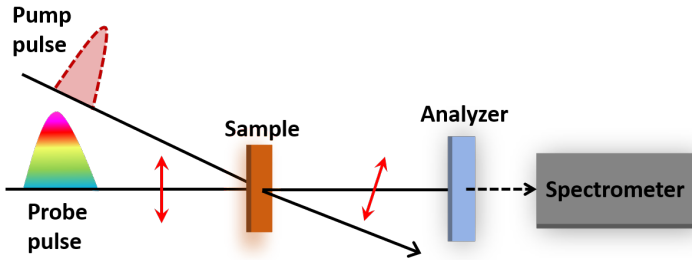
Figure 2.13: Graphical representation of optical Kerr experiment The analyser placed after the sample modulates the polarization of the probe beam to be detected.
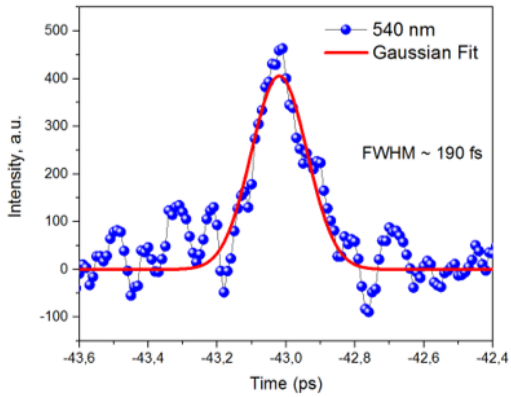
Figure 2.14: Experimental result of cross correlation of the 515 nm pump and white light probe on a 1 mm quartz substrate.

For our experimental set up, the temporal instrument response is a Gaussian, with

a FWHM of 190 fs, as measured on 1 mm thick quartz substrate. This method of detecting the IRF value in a optical set-up is also called optical Kerr effect (OKE). Figure 2.14 shows a typical IRF obtained by determining the cross-correlation between the pump and probe pulses.

2.3.4 Chirp correction

Ultrashort pulses undergo a natural phenomenon known as group velocity dispersion (GVD)[64] when they propagate through materials, in response to wavelength dependence of refractive index of the medium. A chirped broadband probe (480-750 nm) is used in the experiments and thus, the temporal overlap of the pump beam with different wavelength components of the probe is different, i.e. the time-zero is wavelength dependent. Figure 2.15(a) shows a typical 2-D transient absorption plot presenting
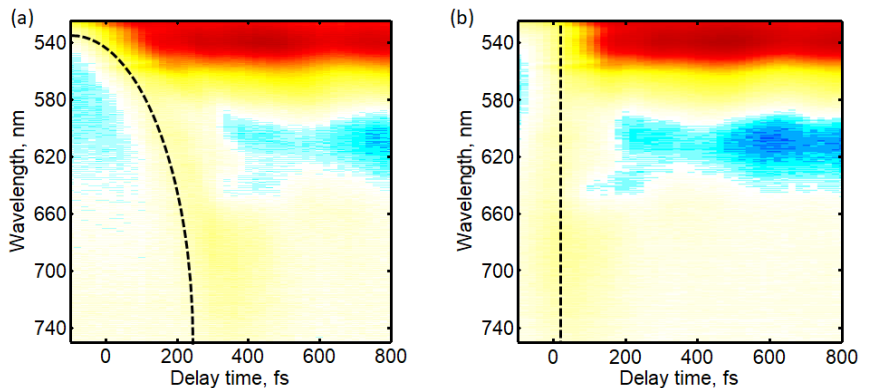
Figure 2.15: Transient absorption data depicting:(a) chirped and (b) chirp corrected spectrum.

absorbance change as function of time and wavelength. Due to intrinsic chirp of the

pulse there is a curvature in the spectrum along the time axis. This manifests the need to do data correction before proceeding to kinetic analysis.

To achieve similar time zero for all wavelengths, a mathematical correction is used which is achieved by fitting the optical Kerr response for different wavelengths in the probe spectral window. The maxima is recorded of peak positions (in time) all wavelength and is plotted against corresponding wavelengths. The curve is fitted using appropriate polynomial function and is subtracted from data to correct the chirp. This permits the reconstruction of a new time corrected matrix. Figure 2.15(b) represents the typical 2D plot obtained after chirp correction.

2.4   Two-dimensional photon echo spectroscopy

Time-resolved optical absorption and emission spectroscopy techniques in the "standard" UV/vis spectral region have gradually reached a level of maturity over the last several decades that today makes them well-established workhorses to study dynamic processes in a wide range of solar energy conversion materials all the way down to the few-femtosecond time-range.

Two-dimensional, called multidimensional spectroscopy is four-wave mixing technique, where three time-interaction of the light field with the sample generates a signal, emitted in the direction different from the incident fields. It aims at determining the complete third order response function from a quantum-mechanical system, like molecules or aggregates.[76] A range of phase-matching geometry based on momentum conservation can be employed to perform these experiments. Proper pulse sequencing and delay ordering between pulses generates the two-dimensional spectrum.[54] Three pulses, 1,2 and 3 are used to generate the signal, while the 4 pulse, called *local oscillator* (LO), is used for detection. This process of detecting a signal is called *heterodyne detection*. Unlike TA spectroscopy, where we use narrow width pulse for excitation,

2D spectroscopy requires a femtosecond pulse (here visible and near infrared) with sufficient bandwidth to excite manifolds of electronic states, simultaneously.

Figure 2.6 shows the schematic of pulse configuration in space and time in a 2D set-up. Delay between pulse 1 and 2 is called *coherence time*, denoted by τ, the time delay, T, between 2 and 3 pulse is referred as *waiting time*, and the delay between pulse 3 and the signal emitted, t, is called *detection time*. 2D spectrum is generated, conventionally, by doing Fourier transformation with respect with τ and t for fixed values of T. Since in 2D spectrum screening is not done just along the detection window but also along the excitation window, it provides more elaborate information about the dynamical behavior of the system under study. Also, 2D spectra show how excitation with one (variable) frequency affects the spectrum at all other frequencies, thus revealing the molecular connections between transitions. In a sense, 2D spectroscopy has added a new dimension to the existing 1D time resolved spectroscopy.

The first pulse when impinges the sample, oscillations induced by the laser field create quantum coherence between the ground and excited states ($|g\rangle \langle e|$). Interaction with second pulse can either create ground state population ($|g\rangle \langle g|$) or excited state population ($|g\rangle \langle e|$). Now, it's the interaction of third pulse that creates a coherence in the ensemble, which in turn radiates signal. The radiated signal field $E(t, \tau, T)$ is measured as a function of time and then Fourier transformed to generate frequency spectrum $E(\omega_t, \tau, T)$. In an array of such spectra each peak will be modulated as function of τ. Fourier transformation of the array with respect to τ will give 2D spectrum $S(\omega_t, \omega_\tau, T)$ correlating changes in the directly detected nonlinear signal field to the indirectly detected excitation frequencies that triggers them.[77]

A conventional 2D spectrum is shown in figure 2.16. Peaks along the diagonal axis corresponds to all the electronic states excited by the laser pulse (here two states, A nad B). This separation between electronic states is possible in 2D spectrum, unlike
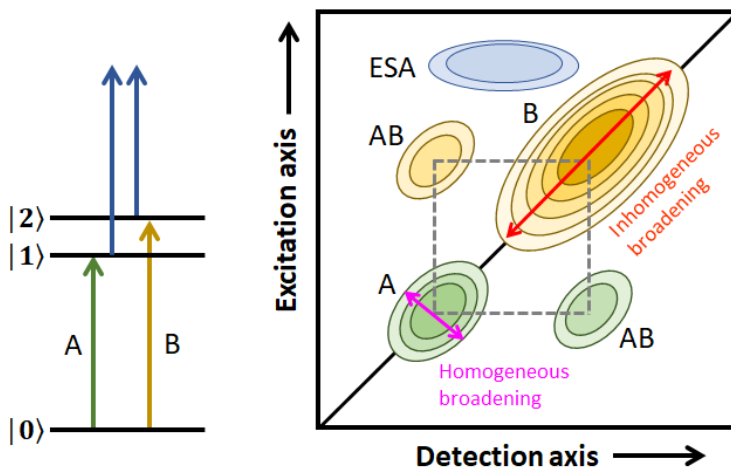
Figure 2.16: Cartoon representation of a conventional 2D spectrum. The electronic picture of a system is depicted on the left side of the diagram. Right side represents the corresponding 2D spectrum of the system. Peaks along diagonal axis represents all electronic states excited by the laser pulse. The presence of off-diagonal peaks (AB) manifest coupling between the electronic states (A and B).

in 1D spectrum where these peaks are convoluted. The presence of cross peaks (here AB) along the anti-diagonal axis represents the coupling between the electronic states. Study of these cross peaks help in understanding the energy (charge) transfer process in the system, an important prospect in this work.

In addition, the linewidth of peak along diagonal axis tells about the inhomogeneous broadening caused by static disorder in the system and the linewidth along the anti-diagonal axis provides information about the homogeneous broadening. The signal generated in 2D spectroscopy , like GSB, ESA and SE, are same as in pump-probe

spectroscopy.

2.4.1   2D set-up

2D set-up in pour lab has four major component :

- Broadband pulse generation

- Pulse compression

- Generation and alignment of four pulses

- Detection

Broadband pulse generation: A pulse with broad bandwidth was generated by a nonlinear process, called non-collinear optical parametric amplification (NOPA). The fundamental beam (1030 nm) is first divided into beams by a (90:10) beam splitter. 10 % of the energy was used to generate the seed beam while 90% of the beam was used to generate pump beam, needed for NOPA beam generation.

The beam in the seed line was allowed to pass through a rectro-reflector (RR) and an attenuator (to control the power of beam). After being reflected by dielectric mirror (M1), seed beam was focused on the YAG crystal by a convex lens (focal length, $f = 30$ mm) to generate a super continuum. To have a handle on the focusing condition on the YAG lens is mounted on a translational stage. Soon after continuum generation the beam is collimated by another convex lens (L2, $= 20$ mm).The beam is then directed by two silver mirrors (M2 and M3) to the NOPA crystal (BBO) for amplification.

For the pump beam, 90% of the fundamental beam is first passed through a half wave plate (WP2), to rotate the polarization direction. It then passes through a type I BBO crystal (23.4°) for second harmonic generation (SHG). This nonlinear process
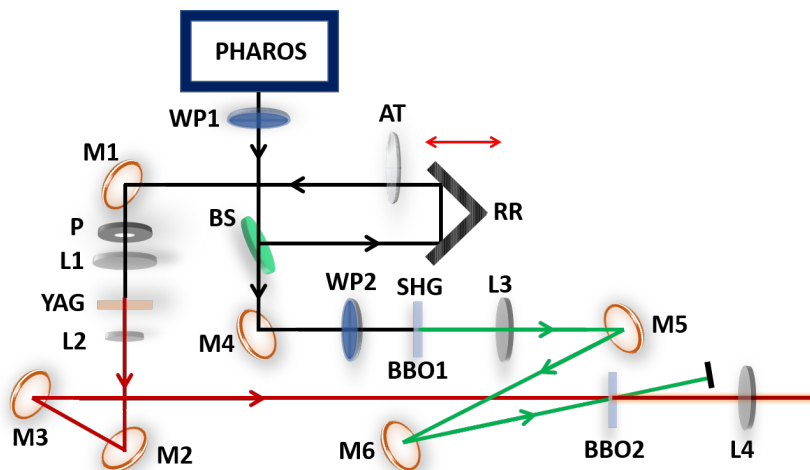
Figure 2.17: Schematics of NOPA design used to generate broadband pulses for 2D measurements. Here WP is wavelate, M is mirror, BS is beam splitter, AT is attenuator, RR is retro-reflector, L is lens, P is pinhole.

generates 515 nm beam. This beam is then focused onto the NOPA crystal by a convex lens (f = 1000 mm), after being directed by two dielectric mirrors. These dielectric mirrors (M5 and M6) highly reflective for 515 nm and therefore, remove all the unconverted 1030 nm beam from the pump beam. Both beams (seed and pump) are focused onto NOPA crystal (BBO with 22.05° cut angle). The polarization of the output signal is then rotated by an achromatic half waveplate, from vertically polarized (s) to horizontally polarized before heading to the compressor.

Pulse compression: Pulse compression, in general, is an imperative step for any time resolved spectroscopy. But for 2D electronic spectroscopy it becomes even more
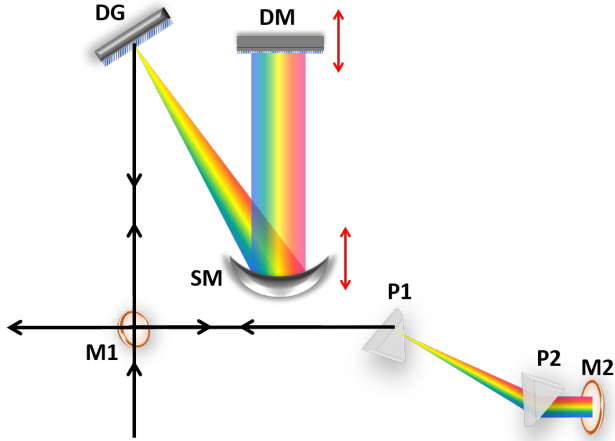
Figure 2.18: Schematic representation of the compressor section in the 2D set-up in our lab. It comprises of three unit: diffractive grating (DG), deformable mirror (DM), and prism pair (P1 and P2). Here SM is spherical mirror.

important. In order to generate PE signal phasing matching is needed in 2D set-up for which phase stability is important.[78] Therefore, it is necessary to compress the pulse to Fourier transform limit before employing it as a light source for 2D experiments.

The NOPA beam possess an intrinsic chirp, due to high non-linearity of processes involved in the generation. Also, the beam passes through a number of dispersive optics which introduces additional group velocity dispersion to the pulse. The schematic of compressor is shown in figure 2.18.

It comprises of three unit: grating optics, a deformable mirror and a prism pair. Firstly, the grating optic (DG, slit $25\mu m$) diffracts the NOPA beam to a spherical mirror (SM). Spherical mirror collimates the diffracted beam onto the deformable

Beam proflie	K-value
Gaussian	0.441
Hyperbola secant	0.315
Lorentzian	0.142

Table 2.3: K-values of different beam profile.

mirror (DM, 19×4 actuators, OKO Technologies) which reflects the beam back to spherical mirror, at slightly different height. Beam is then send back to the diffraction grating. Grating focuses the beam which is then picked up the prism pair (25 mm equilateral F2) for the final compression. First prism (P1) disperses the beam while the second prism (P2) does the collimation and major phase correction in the beam by incorporating variable path length in the beam. A folding mirror steers the beam back through the prism pair allowing for the reconstruction by prism P1. Distance between the dispersive and compressive source is vital to ensure phase correction.[79,80]

Three step pulse compression ensures generation of ultrafast pulse compressed to Fourier-transform limit, determined by time-bandwidth product.

$$\Delta\omega\Delta t \geqslant K \tag{2.58}$$

where $\Delta\omega$ and Δt are spectral bandwidth and temporal resolution measured at FWHM, respectively. K is constant for a particular beam profile. A 40 nm spectrally broad Gaussina beam (K = 0.441) have a temporal resolution of 20 fs (femtosecond).

Here, in our set-up diffraction grating removes all the second order chirp in the pulse. During this process grating induces some higher order chirp which can be easily cleaned by prism compression. These are coarse adjustments in the set-up to get the best compressed beam. While adjusting these optics for compression voltage along all pixels of deformable mirror is set at zero, as such working like a normal

55

mirror. Once the diffraction grating and prism pair have been adjusted to get the best compressed beam, final and fine compression is done by deformable mirror. It corrects the arbitary phase distortions by changing the shape of mirror surface. A generic MATLAB algorithm is used obtain a configuration of deformable mirror which provides maximum signal. All units in the compressor work together to compensate for the chirp in NOPA beam.

Generation and alignment of multiple beams: There are different methods available for generation of multiple beams required in 2D measurements. We have employed the method which uses diffractive optics, described in REF[Dwayne]. The beauty of this method is that, it generates multiple beams from a single beam, therefore maintenance of phase stability becomes easy.

Compressed beam is picked by another mirror and focused onto a customized diffractive optic (DO) by a off-axis parabola (OAP, $f = 100$ mm). Multiple beams are reflected back to the OPA from diffractive optic and gets collimated. $\pm 1^{st}$ order of the diffracted beam, overall efficiency 60%, is used for 2D measurement. Four beams generated in a BOXCAR geometry are arranged as described in figure 2.19. Beams are transversed through different translation stages (MTS1 and MTS2) and focused by OAPM2 (OAP, $f = 40$ mm) onto the sample to generate the photon-echo (PE) signal, illustrated by a red point in the BOXCAR geometry. PE signal generated is very weak and therefore, overlapped with the local oscillator (LO) for heterodyne detection.

During optical transverse, the delay between pulse 1 and 2 can be achieved by moving the MTS2, which allows for the delay scan of the waiting time T. For the same reason, the delay of the coherent time period τ can also be changed by moving MTS1 translation stage. An optical chopper is mounted in the optical path of beam 1 to do differential measurement (pump on/pump off).
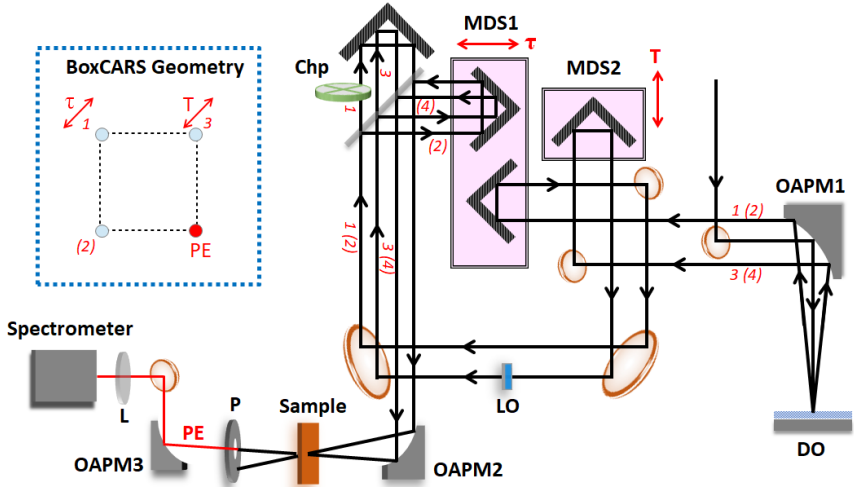
Figure 2.19: Schematic representation of multiple pulse generation in the 2D set-up.

Detection: For DAQ a home built MATLAB software is used, developed by Dr. Valentyn Prokhorenko. A variety of heterodyne detection methods have also been developed over the years, but the so-called Fourier transform spectral interferometry (FTSI) has been most extensively used among them. It is important to separate and extract the information of the signal generated, in terms of phase and amplitude, from the multiple beams interacting to the sample. Here we have used Mach-Zehnder interferometer (figure 2.20) to achieve that goal.

The PE signal generated after three-pulse interaction is mixed with LO. The two fields then interfere with each other, and the total intensity is then detected as:

$$I(\omega) = |E_0(\omega) + E_S(\omega)|^2 \tag{2.59}$$

$$= |E_0(\omega)|^2 + |E_S(\omega)|^2 + 2Re[E_0(\omega)^*|E_S(\omega)] \tag{2.60}$$

where E_S and E_0 are PE signal and LO reference field respectively. The second term of equation (2.60) is very small compared to the last interference term (linearly dependent on reference field). Now with the help of chopper placed in the 2D set-up we can collect differential intensity and can selectively measured the heterodyne signal.
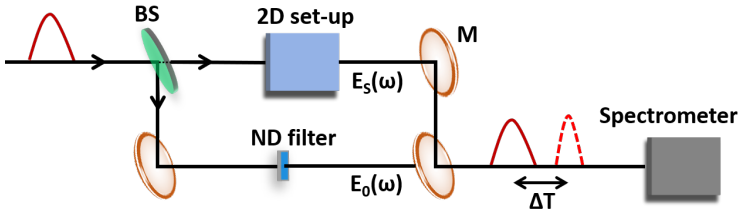
Figure 2.20: General diagrammatic representation of heterodyne detection by Fourier transform spectral interferometer of photon echo signal field generated ($E_S(\omega)$) in 2D experiment. In our set-up ND (neutral density) filter placed in the path of LO generates a fixed delay between the $E_S(\omega)$ and $E_0(\omega)$. Here, BS is beam splitter and M is mirror.

When the reference pulse and signal field are temporally overlapped at the detector, the interference term is likely to be very large. However, in order to enhance the spectral resolution and to selectively eliminate the contribution from the reference pulse spectrum to the measured heterodyne signal, the reference pulse is deliberately made to precede the signal by a fixed time delay ΔT. Here it is achieved by placing a neutral density filter in the LO path. The delay time ΔT is chosen to be large enough to reduce the temporal overlap between the LO and PE signal field but small enough to make the interference signal measurably large. It adds an additional phase factor to the interference signal (ΔT).[54, 77]

Detector includes a monochromator from Scinectech (model 9055) and a 1-D array camera (EntwicklungsburoStresing). Monochromator disperses the interference signal onto high-sensitive CCD linear array camera (1 $times$ 2048 pixels).
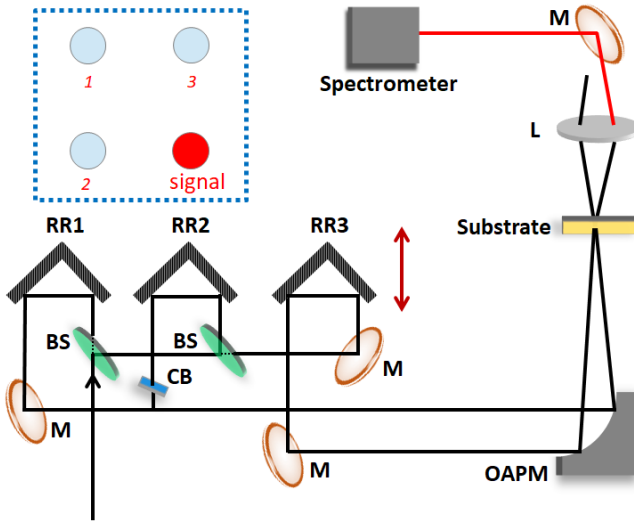
Figure 2.21: Illustration of FROG set-up, inbuilt in the 2D set-up, used for characterization of PE signal.

2.4.2 Pulse characterization

In order to characterize the pulse, Frequency-Resolved Optical Grating (FROG) is used to measure the pulse duration and phase stability. The scheme for FROG is similar to 2D set-up therefore, we do not require an additional unit for pulse characterization.

A conventional schematic of the FROG set-up is presented in figure 2.21. The

configuration of three beams are aligned as BOXCAR geometry and focused by an off-axis parabolic mirror (OAPM, f=40 mm) to the glass plate (usually SF11 or fused silica) to generate the signal. Beams 1 and 2 are coincident in space and time on nonlinear medium and form a grating in the index of refraction of the medium via the nonlinear optical Kerr effect. Pulse 3 is used to diffract off the transiently formed grating by the movable retro-reflector and mapped out at all times the diffracted frequencies of the optical pulse, as measured by the spectrometer (SPEC). A commercial software (FROG3) is used to analyze the FROG trace.

2.4.3   Data processing

The directly measured 2D electronic spectrum shows the absolute magnitude and it should be separated into the real and imaginary part to extract the absorption and transmission information.[54,77] The well-known protocols for the phasing in PE spectroscopy can be divided into interferometric[81,82] and comparative based approaches.[83] In this work, we applied a simple scheme and the theory can be found in V. I. Prokhorenko et al.(2009).[78] It is based on the direct comparison of the spectral profile obtained from transient absorption at zero delay and the PE spectrum, which is retrieved from the heterodyne detection of the PE signal measured at $\tau= 0$, T $= 0$, called **projection slice theorem**. According to this theorem, the projection of the absorptive 2DPE spectra on the detection axis is equivalent to the transient absorption spectrum under same experimental condition. Here, we firstly measure the differential absorption signal for transient absorption experiment, written as:

$$\Delta S_{pp}(\omega) = \mathcal{A}_{pp}(\omega) + \mathcal{A}_{pp}^*(\omega) + S_{pp}(\omega) \tag{2.61}$$

where $\mathcal{A}_{pp}(\omega) = PP(\omega)LO^*(\omega)$ and contains the convoluted spectral product of the TA signal and the LO, and the last term $S_{pp}(\omega)$ corresponds to the homodyne TA

signal. On the other hand, the measured differential PE signal at $\tau = 0$ is given by:

$$\Delta S_{pe}(\omega) = \mathcal{A}_{pe}(\omega)e^{i\omega\Delta T} + \mathcal{A}_{pe}^*(\omega)e^{-i\omega\Delta T} + S_{pe}(\omega), \qquad (2.62)$$

where,

$\mathcal{A}_{pe}(\omega) = PE(\omega)LO^*(\omega)$ and

$S_{pe}(\omega) = |PE(\omega)|^2$

The delay between LO and PE signal is assumed to be:

$\Delta T = \Delta T_0 + \delta t$

where ΔT_0 is the delay induced by the LO filter, shown in figure 2.20. The fast oscillations in the measured interferograms can be removed by multiplying the heterodyne term with $e^{(\pm i\omega\Delta T_0)}$ term. With this procedure we are required to split the measured PE spectrum into two complex-conjugate interferograms:

$$\phi_S = \text{Im}\left\{\ln\left[\mathcal{A}\omega\right]\right\} = \phi_0 + \delta_\phi \qquad (2.63)$$

where $\phi_0 = \text{Im}\{\ln[PE(\omega)LO^*(\omega)]\}$, described as sum of phase spectra of the PE and LO field. Here it has been assumed that the ϕ_0 does not changes. The magnitude of δ_ϕ is characterized by standard deviation (STD) and given by:

$$\delta_\phi = std(\phi_s) \qquad (2.64)$$

Following which the PE spectrum can be obtained as:

$$S_{pe}(\omega) = \Delta S_+(\omega)\Delta S_-(\omega)/S_{LO}(\omega). \qquad (2.65)$$

After the oscillations are removed, we get:

$$\Delta S_{pe}(\omega) = \mathcal{A}(\omega)e^{i\omega\delta t} + \mathcal{A}^*(\omega)e^{-i\omega\delta t} + S_{pe}(\omega) \qquad (2.66)$$

Due to the invariance of the $P^{(3)}$ all terms at $T = 0$ in equation (2.61) and equation (2.66) becomes identical, as $PP(\omega) = PE(\omega)$. As a result both spectra can be given as:

$$\Delta S_{pp}(\omega) = \mathcal{A}(\omega)e^{i\omega\delta t} + \mathcal{A}^*(\omega)e^{-i\omega\delta t} + S_{pe}(\omega) \qquad (2.67)$$

Chapter 3

Coherent Charge Transfers in Photosystem II Reaction Centre

In all photosynthetic plants, the initial charge separation process occurs in reaction center (RC) making it the powerhouse of solar energy conversion. Photoinduced charge separation processes in photosystem II (PSII) RC involve different elementary steps, which are known to take place on ultrafast timescales with near unity efficiency of primary charge separation process. Due to this remarkable efficiency in one of the most essential process on earth, PSII RC serves as an archetype of charge-separation optimize by nature to study it from the fundamental as well as application perspective. In this chapter, 2DES spectroscopy is employed to the isolated PSII RC complex obtained from A. Thallia plant to investigate the photoinduced charge separation process at 20 K. Earlier studies have extracted the time constants associated with photoinduced energy transfer and charge separation processes by various ultrafast spectroscopic methods. Due to the complex network of the underlying processes, ambiguity still exists regarding assignments of spectral features and more recently, experimentally observed coherences in ultrafast measurements. In this study, I have

used ∼16 fs temporal resolution to probe the charge separation processes at low temperature (20 K). Using bandwidth narrowing at low temperature in conjunction with resolved pump wavelengths of 2DES measurements bolster the better assignments of the ultrafast processes in PSII RC. Additionally, I have analysed the impact of experimentally observed electronic and vibrational coherences on the ultrafast energy transfer and primary charge separation.

3.1   Introduction

Photosynthesis powers life on earth and has been an inspiration for human kind to employ sunlight energy as an alternative fuel source. Photosystem II (PSII) is the main component for oxygenic photosynthesis that uses light energy to split water and use the obtained reactive species to generate chemical products via series of chemical reactions. The quantum yield of primary charge separation process process in PSII is very high (~ 1), which makes it a unique and fascinating machinery. It includes a light-harvesting complex II (LHCII) that absorbs solar-light and funnels the exciton formed to the reaction center (RC). Here, the most crucial phenomena of charge separation happens, which is then used for water splitting process.

The RC core is considered as the least sophisticated but most efficient unit of oxygenic photosynthesis to do water oxidation.[84] The structure of RC has been resolved by X-ray crystallography with 1.9 Åresolution.[85] As shown in figure 3.1, RC unit consists of D1 and D2 branches which contains eight pigments: two primary chlorophyll (P_{D1}, P_{D2}), two accessory chlorophylls (Chl_{D1} and Chl_{D2}), two pheophytins ($Pheo_{D1}$ and $Pheo_{D2}$) and two peripheral chlorophylls ($Chlz_{D1}$ and $Chlz_{D2}$), and a cyt b559 (α- and β-subunits). Structurally, the bacterial RC (bRC) complex is quite similar in to the PSII RC.[86] However, unlike the bRC the absorption spectrum of D1/D2/cytb559 complexes containing the PSII RC shows almost no structure even
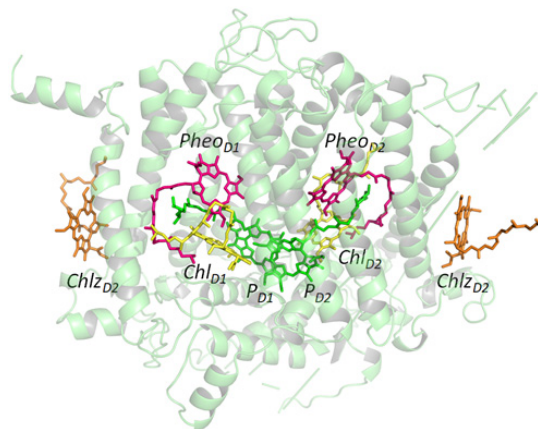
Figure 3.1: Molecular structure of isolated PSII Reaction center.

at low temperature (figure 3.2). This was contributed to the weak excitonic coupling between the special pairs (D1/D2) in PSII RC (140 - 180 cm^{-1}),which is comparable to that between the accessory chlorophyll.[87] In 1960, when Arnold and Clayton first showed the charge separation nature of the photochemical process in photosynthesis for purple bacteria.[88] Since then, researchers have been actively studying photosynthetic complexes to get hold on the mechanism of photoinduced energy and charge transfer process in bacterial and plants RCs.[89] The functional PSII RC could be isolated for the first time in 1987 by Satoh and his student Nanba.[90] This allowed for the first direct time resolved measurements performed by a three-way collaboration between Argonne National Laboratory (ANL), NREL and the University of Illinois with a 500 fs resolution transient absorption set-up at 277 K and 7 K.[91] This led to a series of experimental and theoretical studies to unravel the underlying mechanism of charge separation in PSII RC.[92–105]

With the course of time the laser development progressed and along with it de-

veloped new spectroscopic techniques with better temporal and spectral resolution to probe the photoinduced processes in biological system. It was the recent developments in two-dimensional electronic spectroscopy (2DES) which added a new dimension in understanding the energy transfer and charge transfer process in biological systems. 2DES studies provide a correlation between the excitation and the detection frequency which simplified the data obtained from complex biological systems and as a result many other biological systems including Fenna Mattew Oslon (FMO) were studied by 2D spectroscopy and exact timescale for energy transfer and charge generation processes were extracted from 2D spectra.[103,104] In 2007, first 2DES studies was performed on FMO and coherent oscillation were observed in the 2D spectrum. The observed oscillations in the 2D data was directly translated to the energy transfer processes to being coherent in nature and it gave rise to the idea of quantum biology.[106]This work triggered the study of revealing the role of quantum coherence in the process of energy transfers in light-harvesting complex[107] and marine algae.[108] The first 2D spectroscopic study of PSII reaction center has been performed by Myers et al. at 77 K.[109] They uncovered several relevant energy- and charge-transfer processes on the basis of fitting each individual trace in the 2D spectra along waiting time. More recently, the role of electronic and vibrational coherences were further examined by 2D electronic spectroscopy.[110,111] It have been suggested that the efficient charge transfer are strongly enhanced by the long-lived the vibronic coherence, especially when the frequency of these coherences resonant with the excitonic energy gap. However, a recent study has revisited coherent dynamics in energy transfer of FMO complex.[112] It shows the lifetime of electronic coherence is too short to play any functional role in the process of photosynthetic energy transfer. In summary, the functional role of electronic and/or vibronic coherences has been one important question in the charge separation chemistry in photosynthetic systems.

As discussed earlier, 2DES has been an excellent technique to study the comment

on the nature of coherence generated in the spectrum. In addition, 2D studies have been also found of profound importance to extract the kinetic information of photoinduced processes in the complex biological system.[105,111,113] Both at room temperature and 77 K, multiphasic kinetics has been proposed. Despite all the current understanding of the system there lies some unanswered question regarding the mechanism of the energy transfer and charge separation processes in PSII RC. Once deciphered these principles could be translated directly to the development of bioinspired solar energy conversion technologies. In this chapter, I have collected transient absorption and 2D spectra at 20 K and observed the change in kinetics of oxygenic PSII RC. At cryogenic temperatures, the molecules freeze and therefore, the local disturbances are reduced. In addition, various other intra- and intermolecular effects typically result into reduction of the half-bandwidth of the absorption bands along with the increase in the absorption strength.[114] These phenomena enhance the informational utility of the spectra as well as allow to discern the various spectral features in congested spectra obtained for charge generation process in PSII RC. Moreover, I have also captured the coherences and analysed their role in charge separation process.

3.2 Materials and Methods

3.2.1 Sample preparation

The thylakoid membranes were isolated from A. thaliana plants till the centrifugation step at 6000 g as described in.[115] Thylakoid membranes were solubilized with 0.6% dodecyl-D-maltoside (DDM) to attain 0.5mg/ml chlorophyll concentration. the sample was then ultracentrifuged to separate the PSII core particles as described in.[116] The sample was then purified to extract the PSII RC from the PSII core particles. For purification firslty, the PSII core particles were diluted in BTS200 buffer (20 mM Bis

Tris pH 6.5, 20 mM MgCl2, 5 mM CaCl2, 10 mM MgSO4, 0.03% DDM, 0.2M sucrose) to a chlorophyll concentration of 0.15mg/ml and solubilized with an equal volume of 10% Triton X-100 in BTS200 buffer for 20 min; then the material was loaded on a HiTrap Q Sepharose HP 1ml column (GE Healthcare) and washed with a BTS buffer until the eluate became colorless. Finally, the PSII RC particles were eluted from the column with 75 mM MgSO4 in a BTS200 buffer. The absorption spectrum of the obtained sample is shown in figure 3.2 together with the laser spectrum used in the experiment for excitation.

The solution of RC protein complex was mounted on a home-build sample cell and placed in the cryostat (Oxford Instrument). The 0.5 mm thick cell of 15 μL volume was filled in the dark and was slowly cooled to 4.2 K with liquid helium. Optical densities and pathlengths were chosen based on previous ultrafast studies performed by our group on RC complex.[117]

3.2.2   Experimental conditions

The details of experimental set-up used in this work has been described earlier in Chapter 2. Here I have briefly introduced the experimental conditions used in 2DES and TA measurements of PSII RC at 20 K. To capture the early time dynamics ultrashort pulses with ∼20 fs time-resolution have been used. The characterization of the pulses were done by FROG measurements. The bandwidth of the pulses is ∼100 nm (FWHM) centered at 700 nm. Bandwidth is selected as such it overlaps with the Q_y band of PSII RC. Three pulses are focused on the sample with the spot size of ∼100 μm and the photon echo signal is generated at the phase-matching direction. The 2D spectra for each waiting time T were collected by scanning the delay time $\tau = t_1 - t_2$ in the range of [-128 fs, 128 fs] with 1 fs delay step size. At each delay step, 130 spectra were averaged to enhance the signal to noise (S/N) ration. The
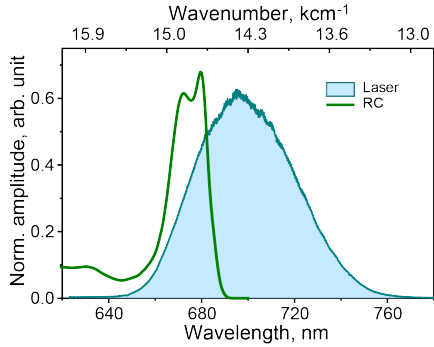
Figure 3.2: Figure shows the absorption spectrum of the isolated PSII RC molecule (green) at 20 K and the laser pulse spectrum (shaded blue) used to excited the temperature. The laser spectrum has been chosen as such to excites all the major pigments in the RC.

waiting time $T = t_3 - t_2$ was linearly scanned -200 to 2000 fs with 15 fs step size. To minimize the alteration in the sample quality all measurements were done with 8 nJ pulse energy and 1 kHz repetition rates. Phasing of obtained 2D spectra was performed using an "invariant theorem".[118]

For TA measurement same set-up was used but instead of four pulses only two pulses were employed for data collection. The projection slice theorem is used for 2D data processing and therefore all other experimental conditions for TA were kept similar as 2D measurements. First we collect the TA spectrum multiple times, for data consistency, and then multiple 2D scans were run on the same sample at different spots. With power dependence measurements we found that the spectral features scale linearly with the power of incident laser pulse, thereby, eliminating any potential artefact on the obtained spectrum due to non-linear excitation such as annihilation.
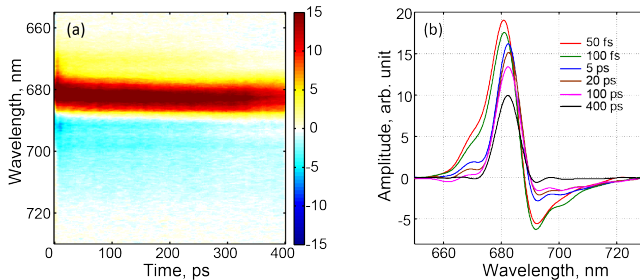
Figure 3.3: Figure showing: (q) 2-D differential absorption spectrum of isolated PS II RC, $\sim$ 20 fs pulses used for measurements with λ_{max} at 700 nm. In the spectrum there is a bleach signal centered around 680 nm and a weak excited state absorption signal around 685 nm. (b) Spectral slices plotted at selected time delays. There is an increase in he bleach signal $\sim$ 100 fs then the signal gradually decreases at later time points and lives upto 400 ps and beyond.

3.3   Results

Figure 3.1 presents the structural arrangement of pigments embedded in the protein matrix (data from 3ENI.pdb) and the measured absorption spectrum of RC complex at 20 K is shown in figure 3.2 (green line). The absorption spectrum PSII RC goes a tangible change at low temperature ($<$ 77 K) and structure appears in the spectrum around Q_y region manifesting the difference in the absorption of two peripheral chlorophyll ($\sim$ 670) nm and six central chromophores ($\sim$ 680) nm.[119] As we are interested in probing coherence dynamics and energy transfer among the excited states of different pigments in the RC complex the laser pulses used in the 2DES and TA measurements were tuned to overlaps with the Q_y transition, shown as blue shaded area in figure 3.2.

3.3.1 Transient absorption spectroscopy

In order to capture the energy transfer and charge separation dynamics in the isolated PSII RC complex, we have measured the differential transient absorption (TA) signal at 20 K. The details of the set-up is given in Materials and Methods section. In order to probe the energy transfer among the excited states of different chlorophyll molecules the laser pulses used in the measurements were tuned to overlap with the Qy transition. The differential absorption signal measured (figure 3.3(a)) primarily shows two prominent spectral features: a weak excited state absorption (ESA) feature and a strong ground state bleach (GSB) feature. The ESA signal is centered around ~ 685 nm and the GSB is centered at ~ 680 nm. Spectral traces plotted at different delay time (figure 3.3(b)) shows an initial increase in the positive peak within 100 fs. At later delay time the signal decays with multiple time constants. The TA spectrum is interpreted by global analysis which extracts the decay associated spectra. The details of global fitting approach is described in Appendix A. Since it is a well established that the PS II RC follows $RC^* \rightarrow$ Radical pair I $\rightarrow$ Radical pair II, we have used a sequential model in which one component decays into the next one and so on. After fitting global analysis was performed to retrieve decay associated spectra (DAS) with separate time components, which gave us five separate time components: < 20 fs, 240 fs, 3.8 ps, 31 ps and infinity, as shown in figure 3.5.

3.3.2 TA-Decay associated spectra

The global analysis of the transient data extracts five exponential decay time components ranging from ~ 50 fs to a non-decaying component for PSII reaction center. Below we discuss in details each DAS components shown in figure 3.5:
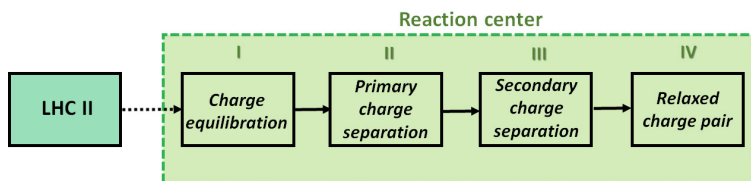
Figure 3.4: Diagramatic representation of sequential model used for extracting DAS spectra.
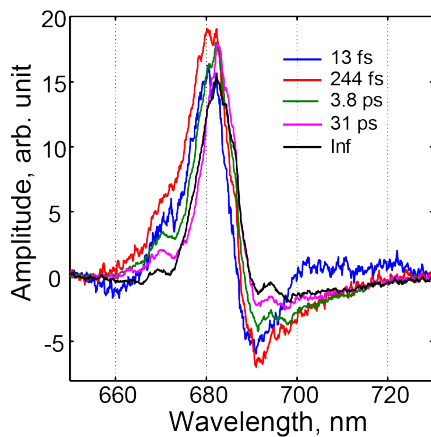
Figure 3.5: DAS spectra obtained after global analysis of TA spectrum with five exponential decay constants.

< 20 fs time component

The first DAS obtained evolves with a time constant of < 20 fs. The value of this time component is very similar to the fwhm of our instrument response, and therefore neither the lifetime nor amplitude can be extracted with precision.

240 fs time component:

In contrast to the bacterial RC, the pigments in PSII RC are in close proximity which leads to the dipole-dipole coupling between the pigments. As a consequence, the energetic modulates and delocalized exciton state are formed. This is referred as multimer model of PSII RC.[120] In this model all the central pigments in the RC are coupled and therefore the optical excitation is the energy equilibrates between excitonically excited states of RC pigments as proposed in work done by R. V. Grondelle (1994) and J. Durrant (1994). Therefore, it can be assigned to the energy equilibration among different pigments in the reaction center.[121]

3.8 ps time component

This component has been previously observed and assigned to decay of RC^*. These are considered as the primary electron donor in the PSII.

$$RC^* \rightarrow Chl_{D1}^+ Pheo_{D1}^-$$
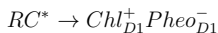
The quantum yield for this primary charge transfer (CT) is near unity.[122,123] Previous studies have suggested a strong coupling of CT state with exciton states facilitating the formation of radical pair[124,125] $(P_{D1}^+ Pheo_{D1}^-)$.

31 ps time component

This time component has been assigned to the energy transfer from peripheral chloro-phyll ($Chlz$), absorbing at 670 nm, to the reaction center core.[97] This component has been interpret as a slow energy transport process due to rather weak electronic couplings arising from the relatively large distance. These pigments are not a part of primary donor and trap the excitation energy at low temperatures slowing, which slows the rate of this charge transfer process. With single wavelength pump-probe measurements it has been shown in the literature the At high temperatures this pro-cess occurs within 16-21 ps time scale.

non-decaying time component

In our experimental set-up we could only collect data till 400 ps delay, but we observe a non-decaying signal in the transient data and therefore we have included a long non-decaying time component ($\sim$ 3 ns). This component has been assigned to the radical pair ($P_{D1}^+ Pheo_{D1}^-$) formation and is in consistent with the previously global done analysis studies.[126]

3.3.3   Two-dimensional electronic spectroscopy

The real part of 2D electronic spectra are shown in figure 3.6 with selected waiting times at 30, 90, 210, 510, 1005 and 1800 fs. In figure 3.6, the positive amplitude plotted as red peak in 2D spectra indicates ground-state-bleach (GSB) and/or stim-ulated emission (SE) and excited state absorption (ESA) is represented as blue peak and corresponds to negative amplitude. The first 2D electronic spectrum at T = 30 fs is shown representing all the optical transitions of PSII RC along the diagonal axis concentrated in the 14500 to 15000 cm^{-1} range. The nonstoichiometric presence of cofactors in the RC sample causes heterogeneity that leads to the broadening of the

linear absorption spectra and is manifested as elongation along the diagonal axis in the 2D spectrum. The broad bandwidth of the laser pulses employed in measurements enabled us to capture the cross-peaks instigating coupling between electronic states in the RC. At later waiting time points we do not observe any significant in the 2D spectrum, except the system becoming more homogeneous marked by the reduction in elongation of main peak along diagonal axis. In addition, the anti-diagonal bandwidth of main peak is continuously increases with the increasing waiting time (figure 3.6). Interestingly, we observe cross peaks located at $(\omega_\tau, \omega_t) = (15000, 14700)$ cm^{-1}, which manifests down-hill energy and charge transfers.

It has been demonstrated in the literature[112] that the lifetime of electronic dephasing can be directly extracted from the anti-diagonal bandwidth in 2D spectrum. Here, we retrieve the anti-diagonal slice of the main peak from rephasing part of 2D spectrum at $(\omega_\tau, \omega_t) = (14700, 14700)$ cm^{-1}, shown as red solid line in figure 3.8. The rephasing part of 2D electronic spectra at T = 30 fs are shown in figure 3.8(b) and (c). To retrieve the lifetime, the obtained profile was fitted with three Lorentzian lineshape functions, dotted blue line in figure 3.7. It gave the lifetime of electronic dephasing as 165 fs at 20 K.

3.3.4   2D-Decay associated spectra

To study the coherent dynamics in 2D spectra, firstly, a three-dimensional data is constructed by resorting time series of 2D electronic spectra with evolving waiting time (T). Subsequently, global fitting approach is performed to retrieve the decay-associated spectrum (DAS) with separated time components, which is given as $S(\omega_\tau, T, \omega_t) = \sum_I A_I(\omega_\tau, \omega_t)\exp(-T/\tau_i)$, where $A_I(\omega_\tau, \omega_t)$, is the DAS with the lifetime of i. We have parallel model to fit the initial 1000 fs data and obtained two species with 27 fs and 700 fs decay time constant. The 2D-DAS with 700 fs time
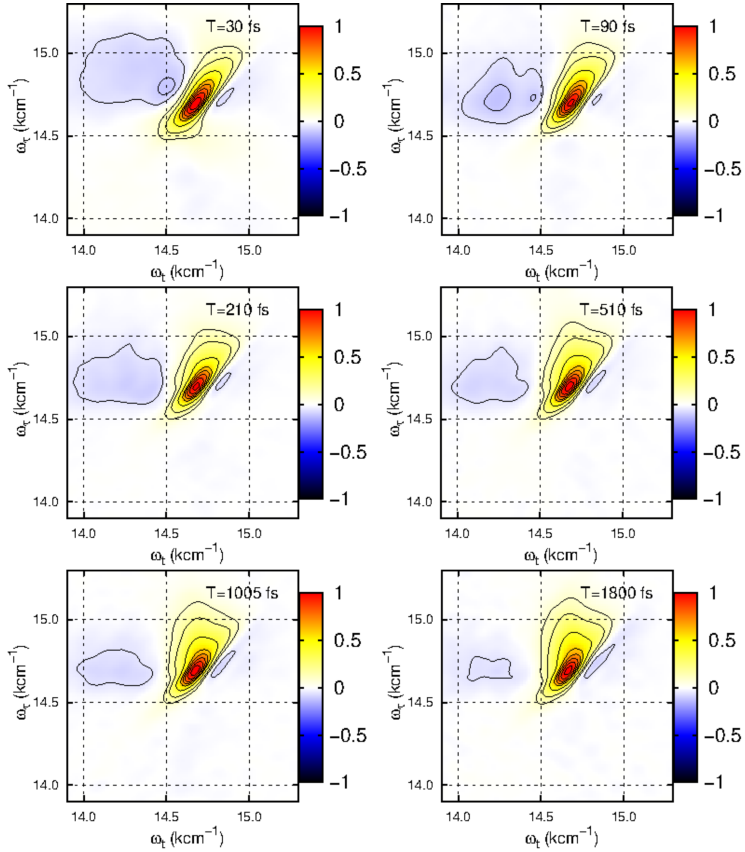
Figure 3.6: Real part of 2D electronic spectra of RC complex measured at 20 K with selected waiting times at 30 fs, 90 fs, 210 fs, 510 fs, 1005 fs and 1800 fs, respectively.
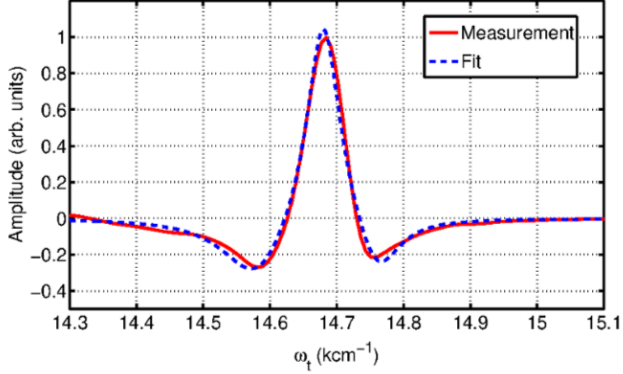
Figure 3.7: Anti-diagonal bandwidth of main peak obtained from rephasing part of 2D spectra at T = 30 fs, $(\omega_\tau, \omega_t) = (14700, 14700)$ cm^{-1}.

constant is shown in figure 3.8(a).

The fastest component with 27 fs time constant manifests the fast peak broadening and multiple pulse-overlap effect in 2D spectra at initial waiting time. The second component of 700 fs shows interesting diagonal and off-diagonal features in the spectrum (figure 3.8(a)). Diagonal peak with positive amplitude is observed from 14700 to 15000 cm^{-1} in DAS, which indicates the population decay of the area in 2D spectra. Additionally, a clear diagonal peak with negative amplitude centered at 14600 cm^{-1} is observed in DAS, which corresponds to the population increase in 2D electronic spectra with waiting time. The cross peak with negative amplitude at $(\omega_\tau, \omega_t) = (14800, 14600)$ cm^{-1}, corresponds to the down-hill population transfer from positive diagonal to negative diagonal peaks.[125,127] The DAS with 700 fs time constant is comparable to the coherent charge transfer timescale in PSII reaction center.

76
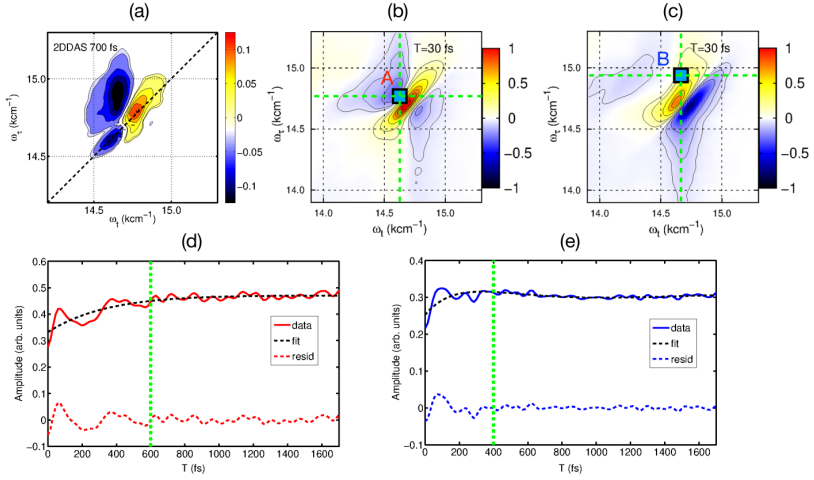
Figure 3.8: (a) 2DDAS with decay rate of 700 fs, this component reveals the ultrafast charge-transfer dynamics associated with electronic quantum coherence. (b) Real part of rephasing 2D electronic spectrum at T = 30 fs. (c) Imaginary part of rephasing 2D spectrum at T = 30 fs. (d) Trace (red solid line) extracted from $(\omega_\tau, \omega_t) = (14750, 14640)$ cm^{-1} (marked "A"). The global fitting approach is performed to removed the kinetic by dashed solid line and the residuals are shown as red dashed line. (e) Trace (blue solid line) retrieved from the imaginary part of rephasing 2D spectra at (ω_τ, ω_t) = (14970, 14690) cm^{-1} (marked "B"). The kinetics are removed by dashed black line and the residuals are shown as blue dashed line.

3.4 Electronic quantum coherence

In a previous work from our group signature of primary charge transfer has been demonstrated.[125] Two primary charge transfer pathways were obtained, given as:

$$(Chl_{D1}Pheo_{D1})^* \rightarrow Chl_{D1}^+ Pheo_{D1}^- \tag{3.1}$$

$$(P_{D1}P_{D2})^* \rightarrow P_{D2}^+ P_{D1}^- \tag{3.2}$$

To examine the first charge transfer process in the PSII reaction center, the kinetics of peak at $(\omega_\tau, \omega_t) = (14750, 14640)$ cm^{-1} is extracted, marked as A in figure 3.8(b). The excitonic states in this region are strongly related to pigments Chl_{D1} and $Pheo_{D1}$, involved in charge transfer. To have better signal to noise ratio, a square of 25 pixels (5×5) is averaged and plotted as red solid line in figure 3.8(d). To remove the high frequency noise from the kinetic data Turkey window Fourier Transform (Appendix B) is performed. Then exponential fitting is applied to he kinetic data, shown as the black dashed line in figure 3.8(d). Residual obtained after subtracting is shown as dashed red line in figure 3.8(d). To extract the coherent charge transfer between P_{D1} and P_{D2}, the kinetics of two excitonic states at $(\omega_\tau, \omega_t) = (14970, 14690)$ cm^{-1} are examined, marked as B in figure 3.8(c). The data is treated with same procedure (as peak "A") and the kinetics extracted is shown as blue solid line is figure 3.8(e). The exponential fit and residue is shown with black dashed line and blue dashed line, respectively.

To study the time evolution of the coherent dynamics wavelet analysis (Appendix C) is performed. The result obtained after analyzing both plots is plotted and shown in figure 3.10(a) and figure 3.10(b). In figure 3.10(a) a strong mode at 100 cm^{-1} is observed, which matches well with the energy gap between Chl_{D1} and $Pheo_{D1}$ excitonic states. This can be directly attributed to the electronic nature of the quantum coherence assisting the primary charge transfer from Chl_{D1} to $Pheo_{D1}$.
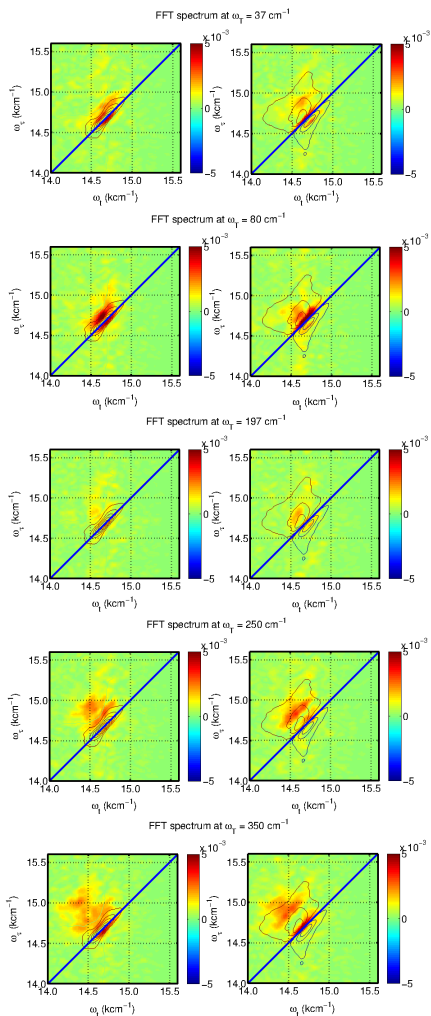
Figure 3.9: 2D power spectrum resolved by Fourier transform of 3D residuals. The identified modes excellently agree to the ground-state vibrations revealed in fluorescence line narrowing experiment.

Lifetime of the electronic coherence obtained from wavelet analysis is ~600 fs, which is strongly overlapped with the long-lived vibrational mode at 80 cm^{-1}. In addition a low frequency mode of 37 cm^{-1} is observed. These 80 and 37 cm^{-1} modes matches well with the results of fluorescence-line-narrowing measurements.[128] This is how the coherent dynamics of the selected peak "A" is studied in the 2D electronic spectrum.

To examine the coherent dynamics of other peaks global fitting approach (Appendix A) is employed. For this, time evolved 2D spectra is fitted globally and kinetics is removed from the data. Then Fourier transform is applied on the obtained 2D residual to generate 2D power spectrum. The 2D power spectrum of $\omega_T = 100$ cm^{-1} is plotted and shown in figure 3.10(c). A cross peak with strong amplitude at $(\omega_\tau, \omega_t) = (14750,14640)$ cm^{-1} is observed, which agrees well with theoretically predicted Chl_{D1} and $Pheo_{D1}$ excitonic states. To further confirm it, the diagonal lines are up shifted with 100 cm^{-1} gap. With the combination of theory and experiment, it has been demonstrated that the 2D power spectrum of 100 cm^{-1} is assisting the coherent dynamics of primary charge transfer pathway: $(Chl_{D1}Pheo_{D1})^* \rightarrow Chl_{D1}^+ Pheo_{D1}^-$. Based on the wavelet analysis in figure 3.10(a), the lifetime of coherence entangled in the process has been resolved as 600 fs at 20 K temperature.

Following same procedure, wavelet analysis was performed on peak B, shown in figure 3.10(b). In the figure, coherent dynamics at frequencies 250 and 280 cm^{-1} can be resolved. The 280 cm^{-1} mode matches with the energy gap of the cross peak $(\omega_\tau, \omega_t) = (14970,14690)$ cm^{-1}. Based on the calculations, this large energy gap corresponds to the strong electronic interaction between P_{D1} and P_{D2} radical pair. Hence, it can be said that the strong electronic coupling between the radical pair is resulting in relatively high frequency oscillations in figure 3.10(b). Furthermore, the lifetime of this mode is 400 fs. The other mode at 250 cm^{-1} matches well with Raman mode in electronic ground state.[128]
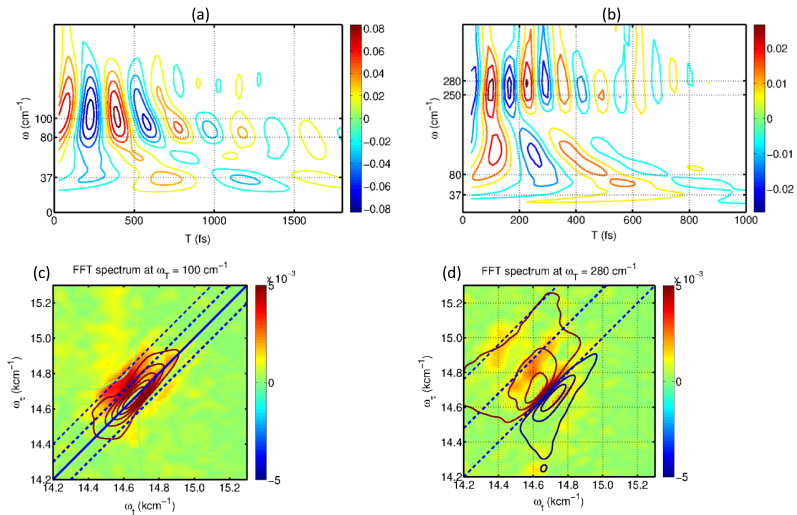
Figure 3.10: (a) Wavelet analysis of trace "A" at $(\omega_\tau, \omega_t) = (14750, 14640)$ cm^{-1}. It resolves the electronic coherence at 100 cm^{-1} and two vibrational frequencies at 37 and 80 cm^{-1}. (b) Wavelet analysis of trace "B" at $(\omega_\tau, \omega_t) = (14970, 14690)$ cm^{-1}. It uncovers the electronic quantum coherence at 280 cm^{-1}. (c) 2D power spectrum at $\omega_T = 100$ cm^{-1}. The diagonal dashed lines are shown with the gap of 100 cm^{-1}. (d) 2D power spectrum at $(\omega_T) = 280$ cm^{-1}. The blue dashed lines are shown as the gap of 280 cm^{-1}.

The power spectrum for this 280 cm^{-1} mode, global analysis is performed. The 2D power spectrum obtained is plotted and shown in figure 3.10(d). As expected, a strong cross peak is present at $(\omega_\tau, \omega_t) = (14970,14690)$ cm^{-1}. To resolve better the energy of cross peaks, the diagonal line is 280 cm^{-1} up shifted (figure 3.10(d)). Based on the theoretical and experimental studies, the coherent dynamics of 280 cm^{-1} mode has been assigned as the signature of electronic quantum coherence between P_{D1} and P_{D2}.

3.5   Conclusion

Due to the strong system-bath interaction in photosynthetic protein complexes, the lifetime of pure electronic quantum coherence is hard to be well-resolved. The congestion of spectrum makes it extremely hard to discern the quantum dynamics of every exciton even at cryogenic temperatures up to 77 K. However, in this chapter, the 2DES experimental measurements on PSII RC at 20 K, we can completely resolve the electronic coherences. The lifetime of electronic coherence of radial pair and the coherence between electron donor and acceptor at the initial step were found to be 600 and 400 fs, respectively. In addition, observed long-lived coherences of 37 and 80 cm-1 have been assigned to be vibrational in nature. Using global analysis on the experimental data, the time constants of elementary steps involved in PS II reaction center's charge generation process have also been extracted. This enabled us to map the process once all the pigments of RC core have been simultaneously excited by the pump pulse. At 20 K, the time constant for primary charge separation process was retrieved as 3.8 ps. The experimental findings reported in this chapter will be used in future as input to the theoretical calculations, which possibly can provide a precise model Hamiltonian to describe the quantum dynamics of PSII reaction center after photoexcitation.

Chapter 4

Photoinduced Vibrations Drive Ultrafast Structural Distortion in Lead Halide Perovskite

In this chapter, I have studied the dynamics of charge carriers in hybrid organic-inorganic perovskite materials by applying 2D electronic spectroscopy. The outstanding performance of perovskites in wide range of application including lasing and solar-energy conversion has attracted researchers to understand their photophysical behaviour. Especially, the long lifetimes of photogenerated charge carriers is one of the puzzles in perovskite photophysics. Earlier reports on this topic proposes the formation of large polaron, however, the understanding towards underlying structural

dynamics was missing. Here, I have focused on how the charge carriers responds to the external field when excited impulsively by laser pulse. With 2D experiments, I was able to capture the specific vibrational motions of organic cation, which induces interaction with inorganic lattice to cause charge-screening effect. The interplay of organic cation and inorganic lattice facilitates polaron formation in perovskites. The mechanistic details provided in this work may guide towards novel design principles for next generation hybrid-perovskite materials.

4.1   Introduction

Hybrid perovskites are described as organic-inorganic mixed halide systems with three principle components: an organic cation, an inorganic anion and halide group (MAX_3), shown in figure 4.1. Perovskites have fascinated researchers with properties such as superconductivity, ferroelectricity, piezoelectricity, ferromagnetism and antiferromagnetism. In 2009, perovskite was introduced as a photosensitizer for dye sensitized solar cells (Grätzel-type) with an PCE of only 3.8%. In a very short span of time metal halide perovskites (MHP) took over the photovoltaic field by storm with their record shattering performance (>20).[28, 129–131]

Recently, Hou et. al. were able to overcome the single junction Shockley-Queisser limit in photovoltaics by fabricating a tandem solar cell with solution processed perovskite on textured Silicon. These solar cells have 25.7% PCE with negligible losses after 400-hour thermal stability test at 85°C.[132] Explored not just in photovolatics, MHPs have been investigated by researchers of many other field and were found to perform well in light-emitting diodes (LEDs) and as lasing materials, etc.[26, 133–136]

Globally researchers are trying to apprehend the origin of the high performance in MHPs but is far from being understood. Ultraslow carrier cooling, nature of charge carriers, stability etc. are few interesting research questions to be addressed. Addi-

tionally, the role of the organic cation and structural morphology in perovskites are also important areas of research. Perovskites have shattered the conventional belief that high crystallinity is required for high solar-conversion, as these materials have shown high solar cell performance with structural disorderness (polycrystalline).[137] Scientist have been in constant pursuit to overcome the barrier related to stability and longevity in order to exploit these materials to their fullest potential.[138–146] Thorough understanding of the photophysical processes occuring in perovskite is required for large-scale commercial deployment.

One of the mysterious characteristic of perovskites is the origin of long charge carrier lifetimes despite having fairly decent carrier mobility,[147–149] 50-100 cm^{2}V^{-1}s^{-1}. The samples are prepared by solution processing methods, which should create midgap states. Mid-gap states are potential recombination centers and hence, should result into short lifetime for charge carriers. To address this perplexing behavior, Zhu and co-workers have studied the effect of different organic cations on the carrier lifetimes of $CH_3NH_3PbI_3$ using combination of time-resolved techniques: optical Kerr effect and photoluminescence spectroscopy. These studies have proposed the charge screening effect due to the re-oriental motion of the methyl cation.[150] Chen and co-workers did band-edge excitation in $HC(NH_2)_2PbI_3$ and $CH_3NH_3PbI_3$ and captured time-resolved photoluminesence as a function of temperature to propose a structural phase transition from lower entropy state to another phase with higher entropy via reorientation of organic cation.[151]

To capture the lattice displacement induced by photo-carrier generation in MHPs, state-of-the art techniques like impulsive vibrational spectroscopy[152] and electron diffraction[153] have also been employed. Although the information gathered from these studies were focused on evolution of inorganic lattice only. The observed low-frequency modes of the Pb-I bending and stretching vibrations reveal the key structural transformations in inorganic lattice after photoexcitation. In support of these

observations, resonant THz phonon excitation showed direct evidence of the mode-driving band gap in the MHPs. It demonstrates the correlation of the band gap and the Pb-I-Pb angle bending vibrations.[154–157] Raman and photoluminescence spectroscopy have also been used to investigate the structure-function relationships in MAPbI$_3$. The librational motion of the MA cation is found to be strongly coupled to the PbI$_6$ perovskite octahedra by a hydrogen.[157] Advanced theoretical calculations have uncovered that the polaron formation is induced by the structural disorder resulting mainly from thermal distortions of the inorganic sublattice. They reduce the overlap between the electron and hole wave functions and the probability of bimolecular recombination is then lowered by two orders of magnitude. Despite these numerous studies, no definite experimental report captures the dynamics of the organic cation during the formation of the large polaron. Such an analysis can reveal the possible functional role of the organic cation in perovskite photophysics.[158]

To resolve the structural dynamics during the polaron formation in CH$_3$NH$_3$PbI$_3$, I captured the coherent vibrational dynamics using ultrafast 2DES. 2DES helps in untangling the different spectral features and hence, excited state dynamics can be exclusively studied using non-overlapping features. This study uncovers the coherent generation of the vibrations specific to organic cations that evolve during the polaron formation.

4.2 Material and methods

4.2.1 Sample preparation

Sample, CH$_3$NH$_3$PbI$_3$ was provided to me as part of our collaboration (Dr. Pabitra Naik and Prof. Henry Snaith, Oxford university). The details of sample preparation is as follows:

Acetonitrile (ACN), gamma butyrolactone (GBL) Methyl ammonium solution, Chloroform and PbI_2 were procured from Sigma Aldrich and used as received. MAI was procured from Dyesol. Tetragonal single crystals of $CH_3NH_3PbI_3$ were prepared by a method described in[159] and were used as a precursor material. The precursor solution was prepared by dissolving single crystals of $CH_3NH_3PbI_3$ in an acetonitrile and methyl amine solution.[160] The final concentration of the solution is 0.5 M. The perovskite films were prepared by spincoating the precursor solution at 2000 r.p.m on quartz substrates for 45 second in a N_2 purged dry box. The UV-Vis spectrum of the thin film was taken on a Carry 300 UV-Vis spectrometer. The solution-processed $CH_3NH_3PbI_3$ is prepared and grown on a quartz substrate with 1 mm thickness. For the optical measurement, the sample film is mounted in the cryostat (Oxford Instrument) with vacuum condition to avoid the degradation by moisture. Figure 4.1(a) shows the molecular structure of tetragonal $CH_3NH_3PbI_3$ with the MA cation. In addition, the steady-state absorption spectrum of $CH_3NH_3PbI_3$ is shown in figure 4.1(b). The laser spectrum used in the present measurements is marked by the light-blue shaded area.

4.2.2 Experimental conditions

Our experimental apparatus for obtaining 2DES is described in detail in Chapter 2. Here, I have briefly explained the experimental conditions used for collecting the data. A broadband spectrum with a linewidth of 100 nm (FWHM) was centred at 13800 cm^{-1} such that an overlap with the near infrared region of the absorption spectrum of Perovskites is achieved(figure 4.1(b)). The excitation pulse was further compressed to the Fourier transform-limit with duration of 16 fs. The 2D spectra were collected at each fixed waiting time T by scanning the delay time $\tau = t_1 - t_2$ in the range from [-128 fs, 128 fs] with 1 fs delay time. At each delay point, 200 spectra were averaged

for high signal-noise ratio. The waiting time $T = t_3 - t_2$ was linearly scanned in the range of 0 - 2 ps with 10 fs step-size. The energy of the excitation pulse is limited to 5 nJ with 1 KHz repetition rates for room temperature measurements, ensuring the observed timescales are not affected by annihilation effects. Three pulses are focused on the sample with the spot size 100 μm and the photon echo signal generated in the phase-matching direction. Perovskite sample is sensitive to atmospheric moisture, therefore to avoid oxidation the sample was kept in the cryostat under vacuum condition (1.7×10^7 mPa) at room temperature. To verify the reproducibility of the results, measurements were performed at different spots on the same perovskite films. Observations were further verified on films prepared from three different batches as well. All measurements showed similar spectral features.

4.3 Results

4.3.1 Two-dimensional electronic photon-echo spectroscopy

To study the carrier dynamics after photoexcitation, the 2D electronic measurements of $CH_3NH_3PbI_3$ were performed at room temperature (296 K). All the measurements were performed in the vacuum cell to avoid sample degradation. The real part of the processed 2D spectra at selected waiting time (T) are shown here in figure 4.1(c) for 0, 50, 200, 320, 410 and 560 fs. At T = 0 fs, the intense bleach peak in the 2D spectrum shows elongation along the diagonal, which is indicative of strong inhomogeneous broadening. A strong absorption feature is also present and overlaps with the central diagonal peak. This overlap induces an apparent shift of the bleach peak to the upper left. At T = 50 fs, reduction in the inhomogeneous broadening can clearly be seen. The diagonal bleach peak also shows a reduced magnitude. The 2D spectrum for T = 200 fs shows further decay of the bleach feature although the
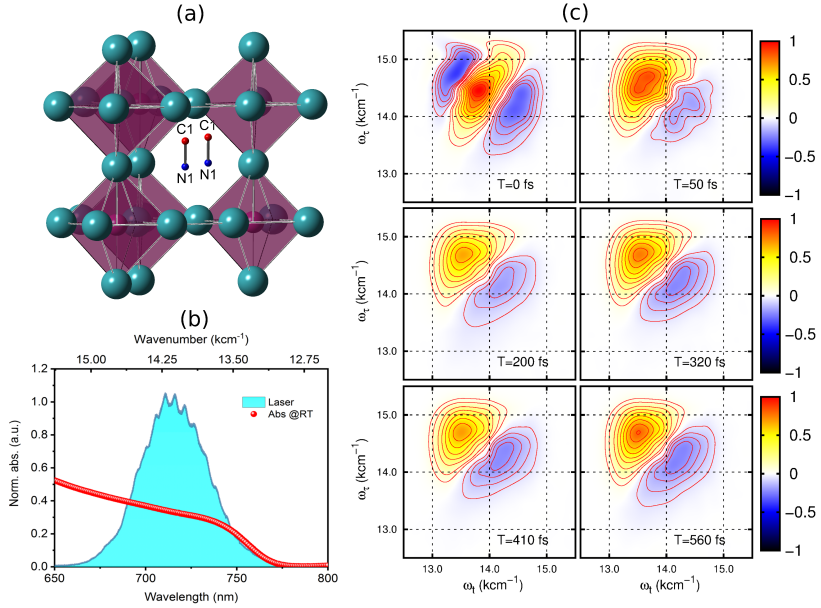
Figure 4.1: Ground state structure of tetragonal $CH_3NH_3PbI_3$. (b) Steady-state absorption spectrum (red circle) of perovskite at room temperature and laser spectrum (light blue area). (c) Time evolution of 2D electronic spectra (real part) at selected waiting times (T). The magnitude of the spectra decays with increasing waiting time. Interestingly, in 2D spectra, the amplitude can be seen oscillating from 200 fs to 560 fs can be clearly observed. Positive and negative amplitudes indicate the ground state bleach and excited state absorption, respectively.

changes in the inhomogeneous broadening are difficult to visualize. Earlier studies on $CH_3NH_3PbI_3$ have assigned the initial dynamics within 200 - 300 fs to carrier thermalization processes and lattice reorganization.[161,162] Thus, the observed changes within

time window should carry the information regarding these processes. In fact, after 200 fs, no significant changes in peak line shapes are present in 2D spectra. Evidently, the magnitude of the peaks in the 2D spectra is larger as we go from 320 fs to 200 fs and from 410 fs to 560 fs. This oscillating magnitude of the bleach features signifies the presence of underlying coherent vibrational dynamics.

4.3.2 Coherent vibrational dynamics

The observed oscillating magnitude in 2D are analyzed in the conventional way. The three-dimensional (3D) set of data consisting of 2D spectra with varying waiting time (T) is global fitted with multiple exponential functions. The global kinetics are then subtracted from the 3D data to obtain the residuals on the fit. The residuals so obtained are plotted along the excitation and detection axis. These residuals carry all the impulsively excited and generated oscillations after photoexcitation. To confirm the origin of these observed oscillations, a 2D correlation analysis is performed. In this analysis method, the oscillations of two correlated peaks are analyzed along the diagonal direction in the 2DES. It has been demonstrated that correlated oscillations originate from electronic coherences and anti-correlated oscillations from underlying vibrational coherences.[163,164] The 2D correlation map for the measured data is shown in figure 4.2(a). Two strong negative peaks along the diagonal are observed, which signifies anti-correlated oscillations at the presented coordinates in the 2DES. Therefore, the observed oscillations in the 2DES data has the vibrational origin.

4.3.3 Frequency analysis

To further analyze the oscillations for their characteristic frequencies, Fourier transformation (FT) is employed on the 2D residuals. The FT analysis presented the vibrational modes with the largest amplitudes, which are plotted here as distinct fre-
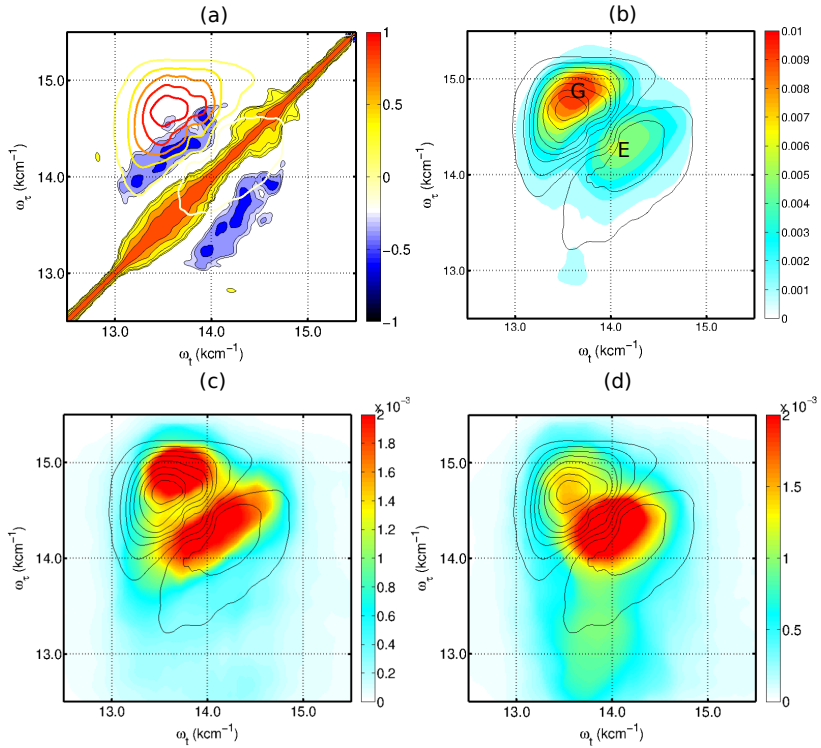
Figure 4.2: (a) 2D correlation spectrum after analyzing correlated cross peaks along diagonal. 2D electronic spectrum at T=200 fs is shown as contours for comparison. (b)-(d) 2D power spectra at frequencies of 157, 65 and 81 cm^{-1}, respectively. For comparison, 2D spectrum at T=200 fs is plotted as black contours. For data analysis, we extract the kinetics of selected peak at G and E in (b) to examine their coherent dynamics in GSB and ESA, respectively.

quencies along ω_τ and ω_t in the 2D power spectra. The 2D power spectra for the frequencies are presented here for selected major modes: 157, 65, 81 cm^{-1} in the panels (b) to (d) of figure 4.2. To comprehend the location of these frequencies easily, the black contours of the 2D spectrum at 200 fs are overlaid with the 2D power maps for all the modes. The vibrational mode of 157 cm^{-1} shows the strongest magnitude in the 2D power spectra. Evidently, the 2D power map at 157 cm^{-1} perfectly overlays with the excited-state absorption (ESA) and ground-state bleach (GSB). The time period of the 157 cm^{-1} mode is 208 fs. This timescale matches the amplitude fluctuation observed in figure 4.1(c). The strong amplitude in figure 4.2(b) is the evidence of strong vibronic coupling of this mode to the underlying electronic transitions. Additionally, two peaks (G and E) are also observed. These peaks are connected by a node, which implies the anti-correlated phase of the oscillations at these two peaks (which agrees with our observation in 2D correlation map). In figure 4.2(c)-(d), the magnitudes of vibrational modes: 65 and 81 cm^{-1} are mainly distributed in the GSB and ESA regions, which are separated by a node. Two retrieved 2D power spectra of the modes at 33 and 48 cm^{-1} are shown in the figure 4.3.

To verify the origin of observed coherences, the extracted kinetic traces at the maximal amplitude of the G and E peaks in figure 4.2(b) are plotted as red (G) and blue (E) lines in figure 4.4(a1). Global fitting method is used to fit the kinetics (fits are shown as black dashed lines figure 4.4(a1)). The residuals obtained after subtracting the fit from the raw data are shown as red and blue lines in figure 4.4(a1). For better visualization, the high-frequency noise was removed by tukey-window Fourier transform and presented as red and blue solid lines for the GSB and ESA in figure 4.4(a2), respectively. Phases of the observed oscillations shown by the red and blue lines are anti-correlated. This further confirms the validity of our earlier analysis presented in the 2D correlation spectrum in figure 4.2(a). The details of the tukey-window Fourier transform are described in the Appendix A.
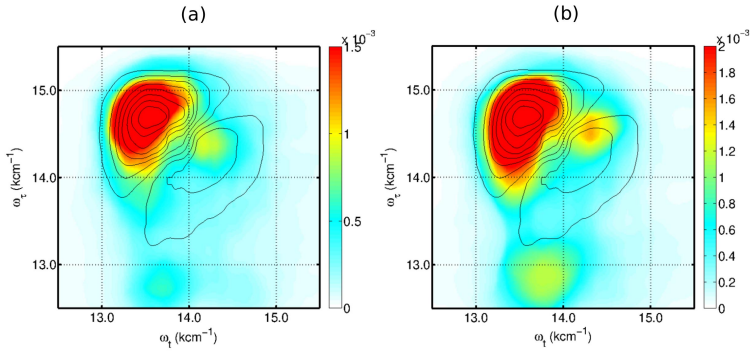
Figure 4.3: Measured 2D power spectra of vibrational modes at 33 (a) and 48 (b) cm^{-1}. They show a strong amplitude in the GSB and ESA regions which are connected by a node.

To further confirm the origin of the observed vibrational modes, Dr. H.-G. Duan in our group constructed a theoretical model with three electronic states. The optical signals of the GSB and ESA are identified for the optical transitions from ground to the first excited state and the transition from first to the second excited state, respectively. Based on his calculations, the anti-correlated oscillations from the GSB and ESA demonstrate the validity of our hypothesis. Hence, the kinetics of the ESA peak can be used to monitor the electronic and vibrational dynamics of the excited state.

After confirming the origin of the vibrations, Fourier transformation of the two residuals resulted into vibrational frequencies, which are plotted as power spectra in figure 4.4(b). The distinct key modes with frequencies of 65 (magenta), 81 (green) and 157 (black) cm^{-1} can be easily seen. Though the low-frequency modes at 33 and 48 cm^{-1} are not well resolved due to the lifetime broadening (in figure 4.4(b)). The

93
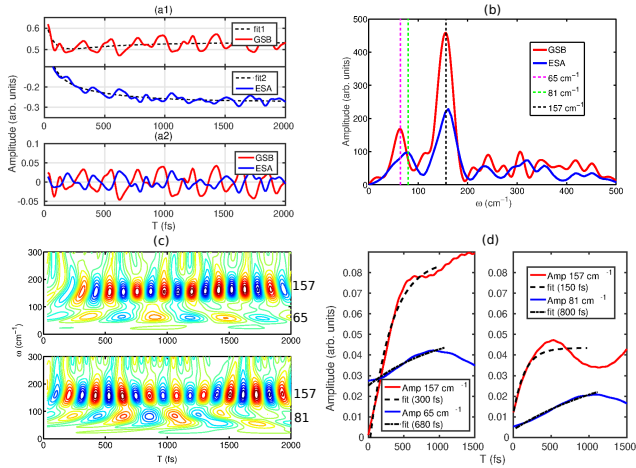
Figure 4.4: (a1) Traces at GSB (red solid line) and ESA (blue solid line). Their coordinates are marked as G and E separately in figure 4.2(b). These traces are fitted by global fitting approach in (a1) and the residuals are obtained after removing kinetics. In (a2), the polished residuals are shown as red (G) and blue (E) solid lines after removing the high-frequency noise. (b) The identified vibrational frequencies in power spectrum. The red (G) and blue (E) solid lines show the vibrational modes at 65, 81 and 157 cm^{-1}. (c) Wavelet analysis of residuals on GSB and ESA. The coherent dynamics of 65, 81 and 157 cm^{-1} modes from GSB (upper panel) and ESA (lower panel) are presented at the left and right part in (d). In GSB (left panel), coherent generation of 65 and 157 cm^{-1} shows an increase in amplitude on the timescale of 680 and 300 fs, respectively. The coherent dynamics of modes at 81 and 157 cm^{-1} show the amplitude increase on timescales of 800 and 150 fs in the ESA contribution (right panel), respectively.

94

vibrational frequency at 157 cm^{-1} shows a strong magnitude and is present in the GSB as well as ESA. The low frequency region (<100 cm^{-1}) shows different frequencies for the GSB and ESA spectra. To analyze these coherent vibrational frequencies in time, wavelet analysis is employed. The spectra obtained are shown in figure 4.4(c) (details of the analysis are described in the Appendix A). The time evolution of the amplitudes of the corresponding vibrational frequencies were analyzed by fitting the exponential decays of the oscillations at 65 and 157 cm^{-1} by sine functions. The time-evolved amplitudes are presented in the left portion of figure 4.4(d). This analysis reveals a coherent generation of 157 cm^{-1} vibrational frequency within 300 fs. For vibrational frequency at 65 cm^{-1}, increase in the amplitude of coherence was observed with a timescale of 680 fs. Similar analysis for frequencies at 81 and 157 cm^{-1} in the ESA part are presented in the right panel of figure 4.4(d). Coherent generation of vibrational frequencies at 81 and 157 cm^{-1} are observed within 800 and 150 fs, respectively. Experimental observations were further validated by computational analysis, performed by our collaborators Dr. Mohamed E. Madjet (Hamad Bin Khalifa University, Qatar) and colleagues. Theoretical calculations reveal that these two low-frequency modes are generated by the skeletal motion (I-Pb-I bending) of the sublattice in perovskite, which are presented in figure 4.5. The localization of the charge density, in turn, enhances the MA librational amplitude. With this redistributed charge, the skeletal motion of $CH_3NH_3PbI_3$ slightly changes its frequencies to reach the (metastable) local potential minimum of the stabilized polaron (details on the calculations are available in the reference[165]).

4.4   Discussion

Based on the discussed experimental and computational work described earlier in this chapter, it can be concluded that the photoexcitation in tetragonal $CH_3NH_3PbI_3$
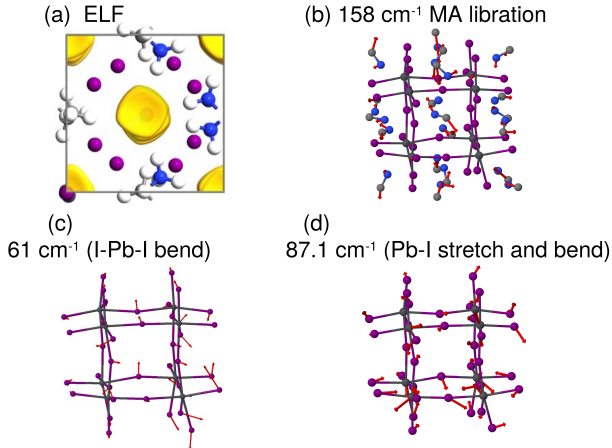
Figure 4.5: (a) Difference of electron localization functions with 1019 cm^{-1} excess electrons compared to its ground state. The magnitude of its isosurface is 0.03. (b) Molecular configuration of perovskite with the librational motions of the MA cation at 158 cm^{-1}. The vibrational coherence of the inorganic sublattice is present in the low-frequency region, 61 and 87 cm^{-1}, which are shown in (c) to (d), respectively.

leads to the formation of a large polaron, which involves the interplay of different vibrational frequencies corresponding to organic as well as inorganic sub-lattices motions. Specifically, the intense coherences of vibrational frequency corresponding to the methyl librational mode at 157 cm^{-1} (158 cm^{-1} from calculations) dominate the early dynamics of 200-300 fs. In order to get insight of the build-up of the librational amplitude of the MA cation, the temporal evolution of the difference of the electronic density between the excited and the ground states for the $CH_3NH_3PbI_3$ model system are analyzed. As shown in figure 4.6, the localization of the excess electron on the Pb atom line up the MA cation via rotation of its molecular axis. This should result into
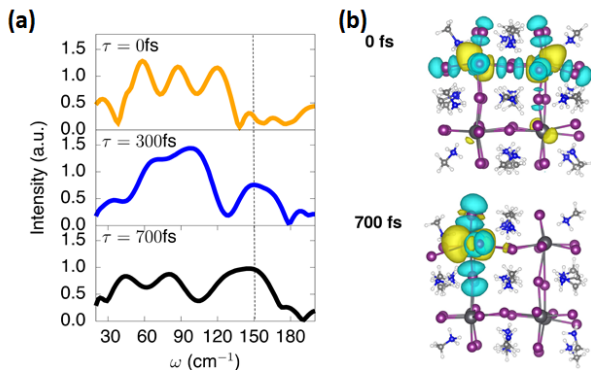
Figure 4.6: (a) Time evolution of the vibrational coherence after photoexcitation. The librational motion of the MA cation (158 cm^{-1}) is generated on a timescale of 300 fs. (b) Based on the ground-state equilibrium structure, the initial electron density is strongly delocalized after photoexcitation.

the generation of vibrational coherence of the MA cation on an ultrafast timescale of 300 fs. Due to the strong anharmonic interaction, vibrational coherence of the librational motion of the organic cation is gained from the sublattice motion of the I-Pb-I skeleton. Based on the simulations, the transfer of coherence is accomplished within 1 ps.

I would like to emphasize here that earlier reports on hybrid perovskites are focused on the role of skeletal modes of inorganic octahedra[152,166] (also reported in this chapter), meanwhile the vibrational modes corresponding to the organic cation has not received its due importance. Especially, the role in excited state dynamics in hybrid perovskites has never been explored before. Therefore, the studies presented in this chapter are the first report on the functional role of organic cation in polaron formation. Bonn and colleagues have performed IR pump and visible probe

experiments to show that the organic cations are electronically decoupled from the inorganic sublattice.[167] I would like to mention here that my work doesn't contradicts this observation. The coherences of organic cation vibrations gain amplitude with time via interaction with the inorganic lattice; it is this interaction which provides the necessary stabilization for the polaronic state. As discussed earlier, the formation of the polaron results into long-lived charges, hence the organic cation performs the electrostatic screening for protection of the charge carriers. This phenomenon is unique to the strong ionic character of MHPs, which greatly distinguishes this class of material from other semiconductors.

4.5   Conclusion

This chapter presents the coherent dynamics of tetragonal $CH_3NH_3PbI_3$ after resonant photoexcitation at room temperature. Employing the high sensitivity of heterodyne-detected 2D electronic spectroscopy, coherent vibrational frequencies were captured. The 2D correlation analysis revealed the origin of the vibrational coherences observed in 2DES measurements. The dominating frequencies are: 65, 81 and 157 cm^{-1}. The strong magnitude of the observed oscillations manifest significant vibronic coupling of these key modes to the corresponding electronic transitions (i.e. ground state bleach and excited state absorption transitions). Based on the wavelet analysis, the key vibrational mode of methyl ammonium cation, 157 cm^{-1} is gradually generated on a timescale of 300 fs. Additionally, the amplitude of the skeletal phonon modes at 65 and 81 cm^{-1} are also enhanced during the process of the coherent generation of the 157 cm^{-1} mode. A structure-based approach developed by theoretical calculations allows us to show the evidence of anharmonic interaction between the MA cation and the inorganic sub-lattice. This interaction further induces a coherent transfer of excitation from the MA cation to the skeletal motion of PbI_3^{-}. Thus, this chapter

summarizes a new comprehensive understanding towards coherent dynamics leading to polaron formation in $CH_3NH_3PbI_3$. Based on the fundamental insight gained in this work, one may anticipate rational design principles for the development of next generation materials.[168]

Chapter 5

Unraveling electronic interactions in molecular-doped polymer

Spin casting of molecular doped polymer solution mixtures is one of the commonly used methods to obtain conductive organic semiconductor films. In spin-casted films, electronic interaction among the dopant and polymer is one of the crucial factors that dictate the doping efficiency. To achieve active control over the doping via spin casting, it is imperative to structurally track the evolution of the dopant:polymer interactions during the film casting process. In this chapter, I have described the use excited state lifetimes of dopant anions to probe the differential electronic interaction in pre-formed ion-pairs of prototypical F_4TCNQ doped P3HT polymer system using ultrafast two-dimensional (2D) electronic spectroscopy. Off-diagonal peaks in 2D spectra clearly establishes the excitonic coupling between P3HT$^+$ and F_4TCNQ^- ions in solution. The observed excitonic coupling is a direct manifestation of Coulombic interaction amongst the ion-pair. The excited state lifetime of F_4TCNQ^- ions in ion-pair shows bi-exponential decay: 30 fs and 200 fs, which implies the presence of heterogeneous population with differential interaction strengths. To examine the nature

of these differential interactions in solution mixture, molecular dynamics simulations on fully solvated model is employed with the generalized Amber force field (performed by Dr. Xin Li). The retrieved three dominant interaction modes of F_4TCNQ anions with P3HT are: side-chain, π-stack and slipped stack. The magnitude of electronic interactions among these modes are directly reflected in excitonic coupling strengths amongst experimentally probed electronic states of ion-pair, which in turn vary the excited state lifetime of the dopant anions in different interaction geometries. To quantify these interactions, we complement our studies with electronic structure calculations on three different interaction geometries, which reveal the excitonic coupling strengths of: $\sim$75 cm^{-1} for side-chain, $\sim$150 cm^{-1} for π-π-stack, and $\sim$69 cm^{-1} for slipped stack. These different interaction modes govern the salient geometries of seed structures in precursor solution mixtures that may dictate the eventual structures in spin-casted films. To gain insight of the evolved dopant-polymer interactions in films, I extended my studies to doped-polymer films as well. The comparison between dopant-polymer interactions obtained using different processing conditions have also been discussed. The important novel insights gained from the study presented in this chapter will guide new strategies to control and ultimately tune the Coulomb interactions in precursor solutions for obtaining higher effective doping levels in spin casted films.

5.1 Introduction

Organic semiconductors are becoming increasingly popular due to the ease of solution processability to obtain devices. To compete with the existing inorganic semiconductors, there are constant research efforts going on towards improvement of the conductivities in organic conjugated polymeric systems using extrinsic methods.[14] Doping of conjugated polymers with tailored small molecular dopants, called as molecular dop-

ing, is one of the widely used extrinsic methods to increase the conductivities.[15, 169–171] Molecular doping results into oxidation (p-type doping) or reduction (n-type doping) of the host polymer systems via charge transfer process. The extent of charge transfer along with the strength of interaction between resultant charges are keys to the success of efficient doping process. Thus, a detailed understanding of evolution of electronic interactions during the doping process is paramount.

In p-type doping, the molecular dopant is chosen such that it's lowest unoccupied molecular orbital (LUMO) is lower in energy than the highest occupied molecular orbital (HOMO) of the conjugated polymer (although there are few exceptions to this rule.[14] The molecular dopant 2,3,5,6-tetrafluoro-7,7,8,8-tetracyanoquinodimethane (F$_4$TCNQ) with LUMO at $\sim$ 5.24 eV is popularly used as p-type dopant for prototypical polymeric semiconductor system poly(3-hexylthiophene) (P3HT) with HOMO at $\sim$ 5 eV.[172] The molecular structures of the mentioned molecular systems has been shown in figure 5.1(a). The P3HT/F$_4$TCNQ system does integer charge transfer to form an ion-pair (IP) of dopant anion and polymer cation i.e. polaron. But, the poor doping efficiency in this system implies that the charges created via doping are not free. Even at high dopant loading conditions of 20 % maximum conductivity achieved is $\sim$ 10 S cm^{-1}.[173,174] Neher group has employed quantitative analysis of the specific near-infrared absorption bands of (F$_4$TCNQ) anion to reveal that nearly every (F$_4$TCNQ) dopant undergoes integer charge transfer with (P3HT) matrix. However, only about 5 % fraction of charges dissociate to actually contribute a free hole for electrical conduction, while the remaining 95 % fraction remains strongly bounded.[175] Thus, the in-depth understanding of physical factors that control the nature and strength of interactions amongst charges during ion-pair formation should pave the way towards efficient doping mechanisms.

There are numerous research works that have contributed towards our current understanding of F$_4$TCNQ doped P3HT system prepared using different methods.[170,171,175–177]

In solution co-processing method, F_4TCNQ is mixed with P3HT in low-dielectric solvent like chorobenzene, which is spin-casted over the desired substrate to form oriented doped films. To obtain the structural insight of the spin-casted polymer films, various experimental tools have been used e.g. atomic force microscopy (AFM),[178] grazing incidence wide-angle X-ray scattering (GIWAXS),[179] electron paramagnetic resonance spectroscopy,[180] infrared spectroscopy,[181,182] Raman spectroscopy,[183] electron diffraction[184] etc. General consensus is that the F_4TCNQ anion stacks between the ordered polymer chains via π-π interactions. However, DFT simulations propose strong orbital coupling between polymer and dopant, which should favour charge transfer complex (CTC) formation instead of the experimentally observed IP formation. Recent observations suggest that molecular doping in this system might be more complex. Jacobs et al. reported a P3HT/F_4TCNQ crystalline polymorph, which gives rise to CTC formation, but interestingly can be converted back to the standard IP polymorph by solvent exposure.[185] This result apart from highlighting the role of crystal structure, also shows the importance of solvent in attaining the IP polymorph with higher electrical conductivity. In fact, Müller et al. have shown how interactions in solvent might predefine doping efficiency of F_4TCNQ doped P3HT films.[186] Thus, it becomes eminent to study the electronic interactions in precursor solution mixtures, which might seed the polymer-dopant interactions in spin-casted films.

To study the electronic interactions in precursor solution mixture of P3HT/F_4TCNQ, here I have used two-dimensional electronic spectroscopy (2DES) measurements along with the molecular dynamics (MD) simulations of solution mixture. The 2DES measurements capture the electronic interactions amongst the ion-pair in chlorobenzene via off-diagonal coupling between polymer cation and F_4TCNQ anion electronic transitions. We used excited state dynamics of F_4TCNQ anion to postulate the presence of differential electronic interaction between ion-pairs in solution, which is further

supported by our MD simulations. The analysis of the MD trajectories provide possible interaction modes operational in precursor solution mixtures. To generalize these observation on other polymeric systems, a similar study is also performed on PBTTT $-$ F$_4$TCNQ precursor solution mixtures. The effect of side chains and different polymer processing conditions have also been discussed in details.

5.2 Materials and Methods

5.2.1 Sample preparation

All chemicals, P3HT (M_w=50,000-100,000), F$_4$TCNQ and chlorobenzene, were purchased from Sigma Aldrich and used without further purification. The sample for steady state absorption in visible and IR as well as 2DES measurements was prepared by the method reported in the literature, with slight changes.[187] 1 mg ml^{-1} orange- red coloured solution of F$_4$TCNQ was prepared in chlorobenzene. The solution was heated upto 130 °C for 30 mins and then kept at 110 °C. The fluorescent-orange coloured solution of P3HT was prepared by adding 10 mg of P3HT in 1 ml of chlorobenzene. This solution was also heated to 130 °C for 30 mins and then was kept at 110 °C. On mixing of both the solutions at 110 °C, the colour of the solution changed to wine-red, indicating the formation of ion-pairs in chlorobenzene. This was further confirmed by the absorption measurements as shown in figure 5.1(b).

For side-chain dependence measurements P3DT (M_w=$\sim$27000) and P3BT (M_w=54,000) were also purchased from Sigma Aldrich. PBTTT polymer (M_w=40,000-80,000) was purchased from Luminescence technology corp. Solution samples were prepared with procedure mentioned for P3HT samples.

5.2.2 Experimental conditions for 2D Electronic measurement

Detailed experimental set-up for 2D electronic measurements has been described previously by our group.[188] Briefly, 16 fs compressed pulses are generated from a home-built non-linear optical parametric amplifier (NOPA), using a combination of a prism-pair and deformable mirror (OKO Technologies). A commercial femtosecond PHAROS laser, by light conversion, is used to pump the NOPA. An all-reflective 2D spectrometer based on a diffractive optic (Holoeye) with a phase stability of lamda/160 has been used for the measurements.[189] Frequency-resolved optical grating (FROG) measurements were used to characterize the temporal resolution of the compressed beam, commercial program FROG3 was used to analyse the FROG traces. The 2D set-up also includes a Sciencetech spectrometer model 9055 which is coupled to CCD linear array camera (Entwicklungsburo Stresing). The linewidth of the broad spectrum so obtained was $\sim$100 nm (FWHM), centered at 13000 cm^{-1}. The bandwidth of laser pulse has been adjusted as such it covered, both, the polaron peak, P2 of P3HT and the second vibronic feature of F_4TCNQ anion. The photon-echo signal is generated by obtaining a phase-matching in the boxcar geometry. The 2D spectra for different population time, $T = t_3 - t_2$ were acquired by scanning the delay time $\tau = t_1 - t_2$ in the range of [-128 fs, 128 fs] with a step size of 1 fs. At each delay step time τ, 150 spectra were averaged to reduce the noise ratio. The waiting time $T = t_3 - t_2$ was linearly scanned till 1 ps with steps of 10 fs. The energy of the excitation pulse is tuned to 18 nJ with the spot size of $\sim$80 μm on the sample and 1 kHz repetition rate. To minimize light scattering, the precursor solution sample was filtered using a 0.2 μm filter and then sealed in a 1 mm quartz cell (Starna). To avoid any sample degradation during the measurements, the sealed quartz cell in the 2D setup was placed on a precise 2D translator and moved at a speed of $\sim$20 cm s^{-1} in both directions. 2D spectra have been retrieved from the measured photon-echo

(PE) signals using the "invariant theorem".[118] The details of the data analysis has been described in the previous reports from our group.[112]

5.2.3 Theoretical calculations

The MD trajectory file contains 20 molecules, the first 10 being P3HT cations and the other 10 F_4TCNQ anions. The simulation has been performed in a cubic box of 10 $times$ 10 $times$ 10 nm^3 containing chlorobenzene as solvent. There were 5103 chlorobenzene molecules contained in the simulation box. The initial condition is set up to NPT, T = 298 K and P = 1 atm. The MD trajectory is analysed to obtained 1000 configurations in 100 ns. For each time point in MD trajectory, we find the closest two F_4TCNQ molecules for every P3HT (from distance between centers of molecules) and generate 10 separated geometries. We use the minimal distance (between non-H atoms) between P3HT and F_4TCNQ since their center of mass distance would not necessarily be small even they form π-π stack. For the 10 $\times$ Nt (^{4}) geometries so obtained, we perform Kabsch transformation and carry out PCA analysis to see whether they can group into different configurations, e.g. side-chain packing/π-π-stacking. We employed k-Means classification to obtain three different three different groups.

5.3 Results

The precursor solution mixture of P3HT $-$ F_4TCNQ in chlorobenzene has been prepared by following the known protocol,[187] which is also briefly described in the materials and methods section. The solution mixture so obtained has 10 wt % of dopant to polymer ratio corresponding to $\sim$5 P3HT repeat units per F_4TCNQ. The interaction of polymer:dopant pairs might have more than one possible mode, which also should
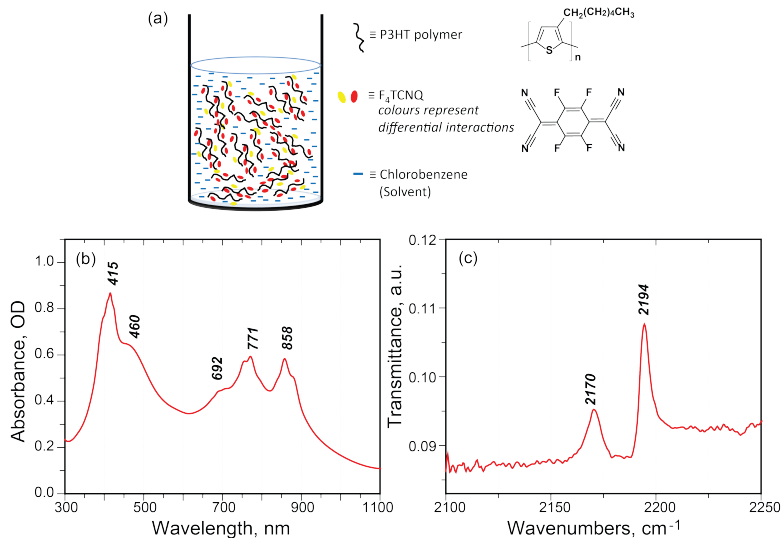
Figure 5.1: P3HT−F$_4$TCNQ: p-doped polymer system. (a) cartoon representation of precursor solution mixture in chlorobenzene showing possible differential interaction between P3HT and F$_4$TCNQ ions (red and yellow colors signify differently interacting dopant with polymer chains). Chemical structures of the polymer P3HT and molecular dopant, F$_4$TCNQ are shown. (b) absorption spectrum of the prescursor solution mixture at room temperature, showing characteristic vibronic features corresponding to F$_4$TCNQ anion. (c) IR spectrum of the system in solution depicting the signature of F$_4$TCNQ anion only (absence of any spectral features corresponding to neutral species can be noted).

correspond to different possible interaction strengths. This scenario has been depicted in figure 5.1(a). Optical spectroscopy has been used widely to characterize the nature of species in the solution mixture of P3HT/F$_4$TCNQ. As mentioned earlier,

107

P3HT $-$ F$_4$TCNQ forms an ion-pair, which can also be seen to exist even in the precursor solution. The absorption spectrum of the solution mixture has been shown in figure 5.1(b). The characteristic absorption band with pronounced vibronic features at 692, 771 and 858 nm corresponds to $D_0 \rightarrow D_1$ transition of F$_4$TCNQ anion.[170] The absorption feature at 415 nm corresponds to $D_0 \rightarrow D_2$ transition of F$_4$TCNQ anion. The absorption features of neutral F$_4$TCNQ is completely quenched on formation of ion-pair, which suggests that most of the added F$_4$TCNQ exist in the form of anions in solution. The absorption spectrum of P3HT polymer cation is rendered invisible due to strong over-lapping F$_4$TCNQ anion signals. The absorption feature at 460 nm corresponds to $\pi - \pi^*$ transition in polymer backbone. To further characterize the nature and interaction mode of F$_4$TCNQ in precursor solution mixture, infrared (IR) absorption spectrum is measured, which is shown in figure 5.1(c). The C≡N stretching frequency region in the IR spectrum shows C≡N symmetric stretch vibrations corresponding to F$_4$TCNQ anion only, which has been marked at 2194 (b$_{1u}$ mode) and 2169 (b$_{2u}$ mode with contribution from b$_{3g}$ mode) cm^{-1}.[186] The C≡N stretching frequencies of neutral F$_4$TCNQ (2227 and 2214 cm^{-1}) do not exist in the solution mixture spectrum, which further validates our hypothesis that all the added F$_4$TCNQ are interacting with the polymer backbone to form ion-pairs in solution. In addition, the 2194 (b$_{1u}$ mode) cm^{-1} mode has also been shown to be the marker of onefold ionization signifying that one principal mode of interaction possibly dominates in the solution mixture. But, interestingly, a very small shoulder at 2202 cm^{-1} can also been seen, which reflects a small population corresponding to partial charge transfer complex.[185] Thus, optical absorption measurements in visible and IR establishes that the precursor solution mixture of P3HT/F$_4$TCNQ in chlorobenzene contains F$_4$TCNQ predominantly in the form of anions. The optical transitions of F$_4$TCNQ anion carry the information of the interacting surrounding, which is in this case are polymer and solvent molecules. Thus, the excited state dynamics of F$_4$TCNQ anion can reveal the

information regarding the electronic interaction strength between the ion-pair and its heterogeneity.
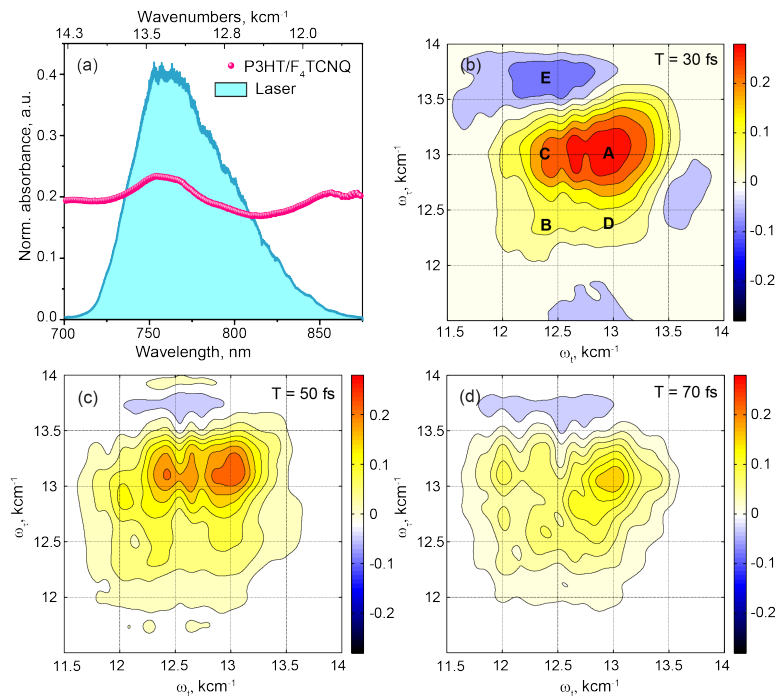
Figure 5.2: Two-dimensional electronic spectroscopy (2DES): (a) Laser spectrum used in the 2DES experiment. Bandwidth is selected as such it covers the polaronic band of polymer and the F_4TCNQ anion band. (b), (c), (d) experimental 2D electronic spectra at different initial waiting points. Red peaks represents the ground state bleach and the blue peaks represents the excited state absorption.

5.3.1 Two-dimensional electronic spectroscopy (2DES) measurements

2DES is an extremely useful nonlinear optical spectroscopic method to study electronic interactions and their dynamics.[77,78,190] Unlike conventional 1D spectroscopic study, 2DES provides a correlation between the excitation wavelength (ω_τ) and the probe wavelength (ω_t). This in turn provides information regarding the electronic couplings present between the different electronic states in the system. Our earlier work on $PBTTT - F_4TCNQ$ has shown the potential of 2DES to study the electronic interactions in molecular doped polymer systems.[191] To capture correlation among the different excitonic states in $P3HT/F_4TCNQ$, we recorded 2D electronic photon-echo spectra at room temperature, for various waiting time. We excited the system with 16 fs laser pulse, centered at 13400 cm^{-1} (760 nm). Laser profile has been such chosen that it covers both, the polaronic band of polymer and the F_4TCNQ anionic band. Measured 2D spectra (real part) at selected waiting times is shown in fig. 2. The diagonal peaks in the spectrum correspond to the electronic states excited by the laser and the off-diagonal peaks represent the coupling between different electronic states. Diagonal peak, A at $\omega_t = 13000$ cm^{-1} represents a strong ground state bleach feature corresponding to transition in the higher electronic state of F_4TCNQ anion ($D_0 \rightarrow D_1$ transition). Another ground state bleach feature, B at $\omega_t = 12380$ cm^{-1} is signature of P3HT polaron (P2 band). In addition, The off-diagonal peaks C and D at ($\omega_t = 12400$, $\omega_\tau = 13000$) and ($\omega_t = 13250$, $\omega_\tau = 12250$) cm^{-1} manifests the presence of coupling in the excitonically coupled electronic states (peaks A and B) of the $P3HT^+F_4TCNQ^-$ ion-pair in chlorobenzene. The excited state absorption feature shown in blue at ($\omega_t = 12500$, $\omega_\tau = 13750$) cm^{-1} possibly represents the $D_1 \rightarrow D_n$ transition. The magnitudes of ground state bleach and excited state absorption features show a dramatic decrease in the later time points, as shown in figure 5.2(c) and

(d) corresponding to 2D spectra at 50 and 70 fs, respectively. Thus, 2DES measurements captures the electronic interactions among the ion-pair in solution mixture and shows the existence of fast excited state decay dynamics of ions.

The electronic interaction among the ion-pair can strongly modulate excited state decay dynamics of the individual ions. Figure 5.3(a) represents the diagonal cut of the 2D spectrum at T = 30 fs. The two features at $\omega_t = 13000$ cm^{-1} and $\omega_t = 12380$ cm^{-1} corresponds to F$_4$TCNQ anion and P2 band of the polymer, respectively. F$_4$TCNQ anion has been shown to have decay time constant of 200 fs via conical intersection in gas phase.[192] Here, in precursor solution mixture, F$_4$TCNQ anion shows a bi-exponential decay with time constants: ∼30 fs and ∼200 fs (figure 5.3(b)). This signifies that possible existence of heterogeneous interactions in solution. F$_4$TCNQ anion population that decays via ∼30 fs time constant represents a strong perturbation via electronic interaction with the polymer backbone, which constitutes the major population (70%). A minor population (30%) decays via ∼200 fs time constant (similar to gas phase decay constant) highlighting that this population does not get perturbed by the strength of the interaction with the polymer backbone (or possibly reflects the poor interaction strength among the ion-pair). In order to discern the cause of these differential decay time-constants for F$_4$TCNQ anions, it is essential to apprehend the plausible interaction modes of the ion-pairs in chlorobenzene.

5.3.2   Molecular Dynamics (MD) Simulations

(*MD Simulations were performed by Dr. Xin Li. I have analysed the trajectories.*)

In order to gain insight into the nature and strength of interaction modes of the ion-pairs in solution, MD simulations using the generalized Amber force field (GAFF)[193] were performed. The MD trajectories contain 10 P3HT cations and 10 F$_4$TCNQ anions, with propagation time of 100 ns. Each P3HT polymer contains 7
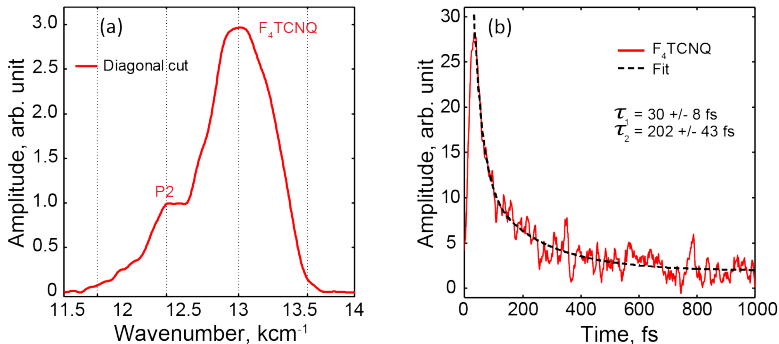
Figure 5.3: (a) Cut along the diagonal axis in 2D spectrum at 30 fs waiting time. The two bands corresponds to F_4TCNQ anion and P3HT cation at 13000 cm^{-1} and 12390 cm^{-1}, respectively. (b) Red curves shows the ultrafast decay dynamics of the F_4TCNQ anion. The kinetic has been fitted bi-exponentially.

monomer thiophenes units alongwith the hexyl side chains. For each time snapshot, we pick the P3HT cations and locate the closest two F_4TCNQ anions for every P3HT cation, using their center of mass distance of the non-hydrogen atoms. To classify the P3HT $-$ F_4TCNQ configurations, we perform the Kabsch transformation to all the P3HT/F_4TCNQ complexes, and project the geometries on the first two major axis from principal component analysis (PCA). In figure 5.4, the projected configurations are classified into three groups: Group 1 (purple), Group 2 (cyan) and Group 3 (yellow) with equivalent populations (i.e. $\frac{1}{3}$ of the total configurations in each group). To visualize the interaction modes in these groups, we take the representative geometry of each group: C1, C2 and C3 (shown in figure 5.4b, c and d). The C1 configuration shows that F_4TCNQ anion is in close proximity to the hexyl side-chain of the polymer. This mode of dopant interaction with the side-chains of polymers has been postulated for molecular doped polymer films by various studies. Configuration C2 depicts the

112

well known π-π-stack configuration of dopant F_4TCNQ anion with thiophene unit of the polymer. In configuration C3, the F_4TCNQ anions are slipped stacked to interact with two thiophene units in the polymer chain. Thus, our MD simulations reveal three major dopant-polymer interaction modes: side-chain, π-π-stack and slipped stack. These different interactions modes must result into differential excitonic couplings between electronic levels of dopant and polymer ion-pairs. The Coulombic excitonic couplings between various ion-pairs are calculated using transition partial charges. The computational details can be found in the reference.[180] The excitonic coupling values obtained are: 75 cm^{-1} for side-chain, 150 cm^{-1} for π-π-stack, and 69 cm^{-1} for slipped stack (it is important to note that these values for excitonic coupling in different interaction modes belongs to representative configurations only. These values remain very similar from one configuration to another within the same interaction mode). Interestingly, slipped stack configuration manifests weak excitonic coupling. Quinoidal ring of F_4TCNQ anions in C3 configuration is placed in between the two thiophene rings resulting into poor electronic overlap of dopant with either of the rings in P3HT.

5.4 PBTTT $-$ F_4TCNQ: second model system

To generalize my observations to other polymer systems, PBTTT $-$ F_4TCNQ system is selected. Recent reports on F_4TCNQ doped PBTTT polymer films have revealed encouraging values of electrical conductivity.[187,194] The molecular structures of polymer PBTTT is shown in figure 5.5. Polymer PBTTT consists of a thieno [3,2-b] thiophene (TT) core having two fused thiophene rings with 6π-electrons in each monomeric unit. The solution mixture of dopant and polymer is prepared using the same protocol as for P3HT system. The measured absorption spectrum showed the characteristic features of F_4TCNQ anion, confirming the formation of ion-pair.
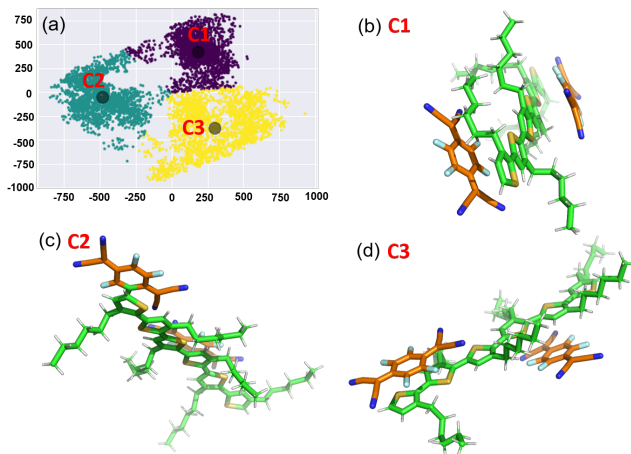
Figure 5.4: Projection of P3HTT − F$_4$TCNQ configurations onto the first two major principal axis. The projected configurations are classified into three groups by the k-means method. The representative configurations of the three groups, the geometries are taken to be the center of the projected points. Configuration 1 can be identified as the side-chain packed geometry, and configurations 2, 3 to be the *pi*-stacking geometry.

Thus, PBTTT − F$_4$TCNQ system serve as the second model system to confirm the observation of electronic coupled polymer-dopant population in the solution mixture.

5.5   2DES Measurements on PBTTT − F$_4$TCNQ solution mixture

Two-dimensional electronic measurements on PBTTT − F$_4$TCNQ is performed using similar experimental conditions as that for P3HT − F$_4$TCNQ system. Measured 2D
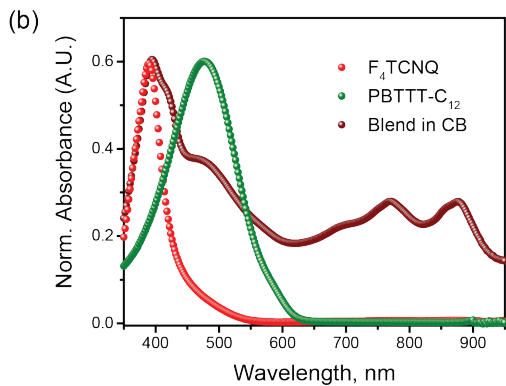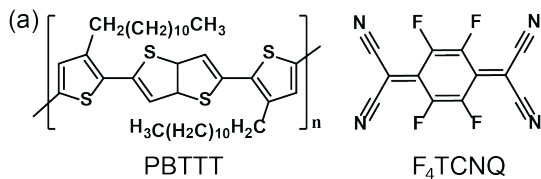
Figure 5.5: PBTTT−F$_4$TCNQ: another model system to study ion-pair in precursor solutions of p-doped organic semiconductors. (a) Chemical structures of the PBTTT (C_{12}-alkyl side chain) polymer and the dopant, F$_4$TCNQ. (c) Absorption spectra of F$_4$TCNQ (in red), PBTTT polymer (in green) and blend mixture of polymer-dopant in chlorobenzene (in brown). The characteristic features for the F$_4$TCNQ anion ($D_0 \to D_1$ transition) confirms the formation of ion-pair in the solution.

spectra (real part) for selected waiting times: 50 fs, 60 fs and 100 fs are shown in figure 5.6. Interestingly, the observed 2D spectra for different waiting times show various diagonal and off-diagonal features, which are marked as A, B, C and D in figure 5.6(a).
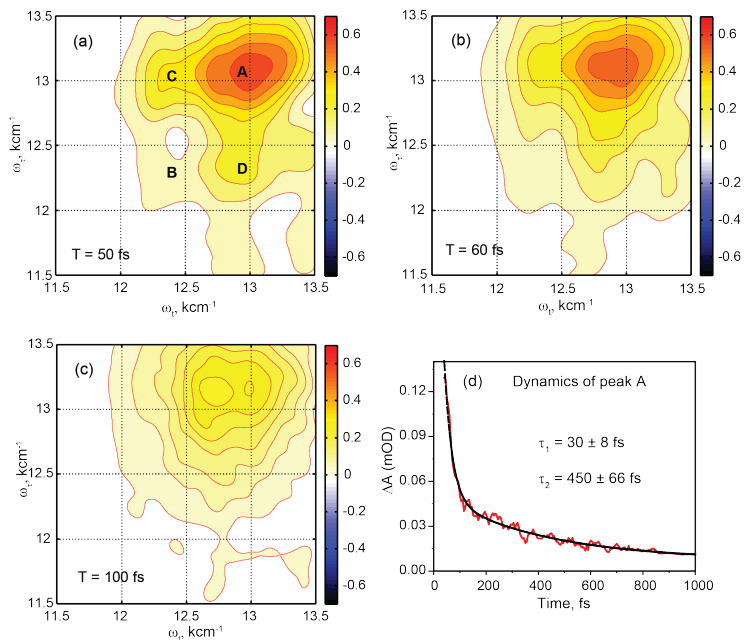
Figure 5.6: Two-dimensional electronic spectra (real part) of the PBTTT − F$_4$TCNQ in chlorobenzene at the selected evolution times: 50 fs (a); 60 fs (b); and 100 fs (c). Red peaks represent the photo-induced increase of the transmission due to the ground-state bleach. Diagonal peaks A and B refers to the bleach signatures corresponding to transitions from F$_4$TCNQ anion and polymer polaron, respectively. The off-diagonal peaks C and D establish the presence of excitonically coupled electronic states of the PBTTT − F$_4$TCNQ. (d) Decay dynamics of F$_4$TCNQ anion's bleach feature at A. The kinetic traces has been fitted to a bi-exponential function shown as black traces.

The off-diagonal peaks C and D establish the existence of evident excitonic cou-pling between the transitions corresponding to A and B corresponding to F_4TCNQ anion and polymer polaron, respectively. The presence of these off-diagonal fea-tures confirms the electronic interaction between the F_4TCNQ anion and the PBTTT cation in precursor solution mixture. The other set of off-diagonal features at lower energies manifest vibronic coupling between the F_4TCNQ anion's transitions. Based on the simulations, we successfully retrieve a strong electronic coupling of 250 cm^{-1} amongst the ions of the ion-pair.[191] Kinetic analysis of the peak A corresponding to F_4TCNQ anion shows bi-exponential decay of 30 fs and 450 fs. Thus, similar to P3HT$-F_4TCNQ$ system, PBTTT$-F_4TCNQ$ also shows heterogeneously interacting population of polymer and dopant.

5.6   Comparison of P3HT vs PBTTT

The presence of three different interaction modes in precursor solutions of P3HT$-$F_4TCNQ$ signifies the heterogeneous nature of these interactions. The π-stack in-teraction mode is the strongest in nature. Although, in comparison to PBTTT, the excitonic coupling strengths for π-stack configuration is weaker in P3HT (250 cm^{-1} for PBTTT as compared to 150 cm^{-1} for P3HT). This can easily be perceived con-sidering PBTTT contains fused thiophene rings as molecular units with rich electron density as compared to single thiophene ring as π-cloud in P3HT. Thus, π-stack inter-action mode should be less detrimental in terms of effective doping in films for P3HT in comparison to PBTTT. Due to the smaller interactions energies in slipped stack and side-chain modes, there should be continuous exchange of population amongst them. These weaker interaction modes (especially side-chain) have been known to exist in doped polymer films as well. It will also be worth to explore how the popula-tions amongst these differential interaction modes can be controlled using systematic

variation in polymers (like side-chain) and film processing conditions.

5.6.1 Systematic evaluation of side-chain length dependence

Alkyl-side chains are means to make the polymers heavy as well as provide solubility. Recently, the polymer side-chain engineering has been used as one of the important ways to align the polymers macrostructures in films.[195] In molecular doped-polymers, the polymer side-chains has also been conjectured to play an important role.[196] In this section, I have described ultrafast transient absorption studies on F_4TCNQ doped thiophene based polymer with systematic variation in the side chain lengths: butyl (P3BT), hexyl (P3HT) and dodecyl (P3DT). The absorption spectra of doped polymers in chlorobenzene are shown in figure 5.7.

All the three polymers show clear signatures of F_4TCNQ anion in the range of 700 to 900 nm. The differences in the intensities corresponding to the vibronic features can also be easily visualized. These differences in intensity as well as peak position can possibly be due to the alteration in static disorders in polymers with different side-chains. The presence of F_4TCNQ anion features establish the formation of ion-pairs in all the three polymer systems.

To explore the dopant-polymer interactions, I have performed transient absorption measurements on the precursor solution mixtures of the three polymer systems. The transient spectra are collected for wavelength window of 700 -850 nm, which perfectly coincides with the desired F_4TCNQ anion features. To perform the transient measurements in linear regime, the pump energy is tuned to 12 nJ. The transient absorption spectra are plotted and shown in figure 5.8 (a), (c) and (e) for P3BT, P3HT and P3DT, respectively. The bleach features (in red) corresponds to the F_4TCNQ anion. In P3BT, a broad excited state absorption band (in blue) at ∼800 nm is also observed. In P3HT and P3DT, the absorption feature is masked by the broad bleach
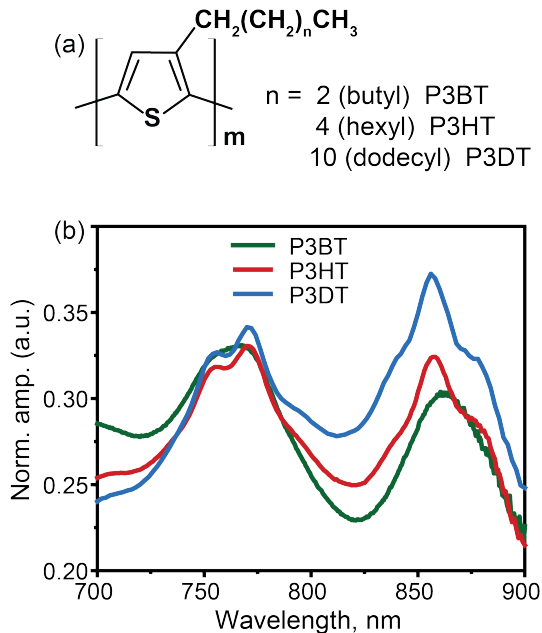
Figure 5.7: Systematic variation in polymer side-chain lengths. (a) Chemical structures of the polymers with different side-chains: butyl (P3BT), hexyl (P3HT) and dodecyl (P3DT). (c) Absorption spectra of F_4TCNQ doped P3BT (green), P3HT (red) and P3DT (blue) in chlorobenzene. The characteristic features for the F_4TCNQ anion ($D_0 \to D_1$ transition) in all the three polymeric systems confirm the formation of ion-pair in the solution.

feature of F_4TCNQ anion.

To further analyze the transient data, kinetic trances at 760 nm are plotted here in figure 5.8 as (b), (d) and (f) for P3BT, P3HT and P3DT, respectively. All the kinetic traces are fitted with bi-exponential function. Interestingly, the major decay
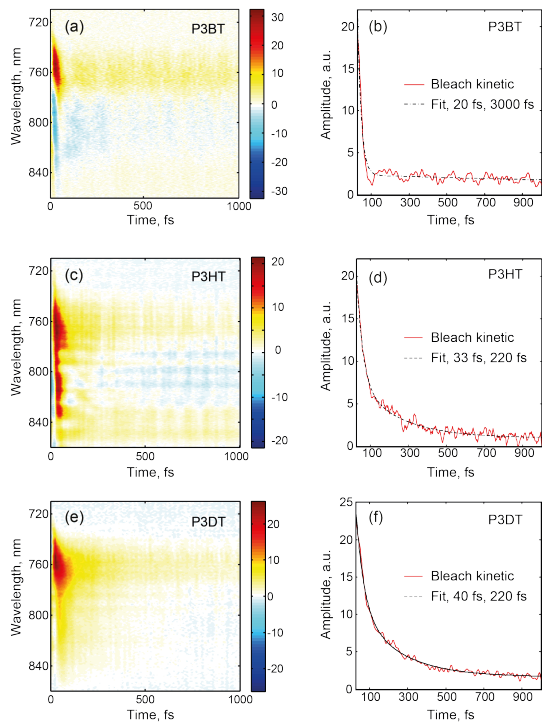
Figure 5.8: Transient absorption measurements on thiophene-based polymers with varying side-chain lengths: (a) P3BT, (c) P3HT and (e) P3DT. Red peaks represent the photo-induced increase of the transmission due to the ground-state bleach and blue peaks corresponds to excited state absorption. The characteristic bleach features for the F_4TCNQ anion at 760 nm can be observed in all the three systems. The decay dynamics of bleach features at 760 nm are plotted for all the polymer systems as (b), (d) and (f). The kinetic traces have been fitted, which are shown as black traces.

component vary systematically with variation in side-chain: 20 fs (P3BT), 33 fs (P3HT) and 40 fs (P3DT). The ultrafast component has been assigned earlier in this chapter as dopant-polymer polymer population interacting with π-π interaction mode. Thus, one can systematically tune the interaction strengths by changing the side-chain lengths. Additionally, P3BT data shows $\sim$85% of the population interacts via π-π interaction mode. This can be easily perceived considering short alkyl chain length in P3BT will have smaller population of dopants interacting with polymer side-chains. In summary for this section, the polymer-side chains are actively participating in the molecular doping process. By systematic variation of the side-chain lengths, we can tune the strength of the polymer-dopant interaction as well as vary the population distribution amongst differently interacting populations.

5.7   Extended structures in solution

Recent studies propose side-chain interaction mode to be major population in some of molecular doped polymer films.[171] Interestingly, our MD trajectory captures transient extended π-stack structures (see figure 5.9).

The extended π-stacked polymer-dopant structures with long-range interactions are known to exist in polymer films. The presence of these structures in solution further bolster our hypothesis on the seeding effect. In the next section, I will focus on how does polymer-dopant interactions evolved to differently processed films.

5.7.1   PBTTT $-$ F$_4$TCNQ films: different preparation methods

To achieve molecular doped polymeric semiconductor films, currently, three principle methods are in use: (1) solution processing (dopant and polymer are mixed in common solvent and then is co-deposited by spin-casting over the substrate); (2) solution
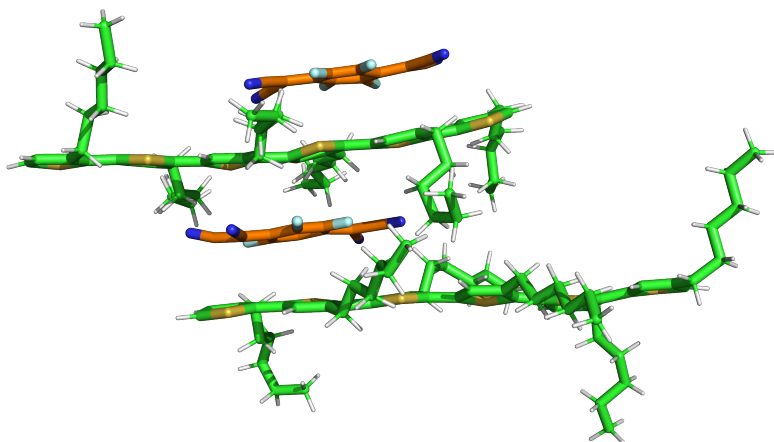
Figure 5.9: Transiently observed extended π-stacked P3HT and F_4TCNQ structures captured in molecular dynamics simulations. These structures mimic the proposed π-stacked frameworks in solution-processed films, and hence possibly act as kinetically trapped seed-structures present in the precursor solution mixtures

sequential processing (molecular dopant is dissolved in a solved and then spin-casted on a substrate which is pre-deposited with polymer film); and, (3) solid-state diffusion (molecular dopant is sublimed on top of a substrate which is pre-deposited with polymer film by spin coating). Importantly, the encounter of polymer and dopant happens at different stages in the three methods. Thus, formation of ion-pair formation is also observed at different phases. In the solution processing method, as discussed earlier in this chapter, polymer-dopant interaction happens in the precursor solution mixture resulting into ion-pair formation. In other two methods, dopant interaction with polymer happens in pre-ordered polymer lamellar microstructures. Therefore, it might be possible that the encounter of polymer and dopant in different

phases results into differential nature and strength of interactions. In fact, recent studies on F_4TCNQ doped PBTTT have shown extremely different electrical conductivity values from this pair: 2 Scm^{-1} (by solution processing)[187] and 248 Scm^{-1} (by solid-state diffusion).[194] It must be noted that in the solution processing method, the intercalated dopant between the π-stacks of the polymer is known to introduce some disorder in the π-stacking, and this might be one of the important reasons behind the observed difference in the conductivity values. Although, the difference in the polymer dopant interactions that also contributes towards the macroscopic parameter of conductivity, is not known.

To understand the nature and strength of interactions in differently processed films, I have studied F_4TCNQ doped PBTTT films prepared using solution-mixed and sequentially processed films. The samples were prepared by Dr. Ian Jacobs (University of Cambridge) as part of the collaboration. The absorption spectrum of polymer films are shown in figure 5.10.

For both the films, absorption spectra show distinct vibronic features (878 and 769 nm) corresponding to F_4TCNQ anions. These features confirm the presence of ion-pair in processed films. Interestingly, the polymer $\pi \rightarrow \pi^*$ transition band is red shifted in sequentially processed film to 577 nm as compared to 526 nm for films prepared by solution-mixing. This apparent red shift does not reflect the bandgap changes. It is rather due to the intensity enhancement in vibronic feature at 577 nm in sequentially processed films. It is well known that this feature gains in the intensity in films due to ordered polymer packing. Therefore, it can be concluded that sequentially processed films have highly ordered lamellar microstructures. The absorption feature at 415 nm corresponds to the $D_0 \rightarrow D_2$ transition of F_4TCNQ anions. Another noticeable observation is that the relative intensities of F_4TCNQ anions vs polymer $\pi \rightarrow \pi^*$ transition bands is lesser in sequentially processed films compared to the solution mixed films. This can easily be understood considering that
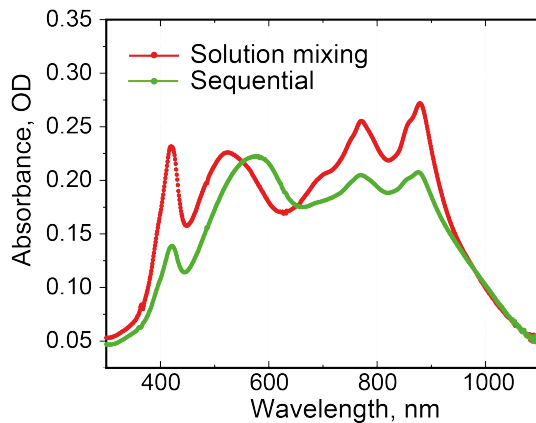
Figure 5.10: Absorption spectra of F_4TCNQ doped PBTTT films prepared using solution mixing (in red) and sequentially processed (in green) method. The characteristic features for the F_4TCNQ anion confirms the presence of ion-pair in both the differently processed films.

the two methods introduce the dopants in different ways, which results in different extent of ion-pair formation. In solution-mixing, dopant-polymer are homogeneously mixed in solution mixture resulting in higher percentage of ion-pair formation as compared to the sequentially processed films. Thus, absorption measurements confirm the formation of ion-pairs in films, and reflects the higher ordered polymer packing with reduced dopant concentration in sequentially processed films compared to solution-mixed films.

5.7.2 2DES measurements on $\mathrm{PBTTT-F_4TCNQ}$ films

To study the polymer-dopant interactions in different phases, I have used 2DES to probe $\mathrm{F_4TCNQ}$ doped PBTTT films prepared using two different methods: solution processing and solution-sequential processing. For all the measurements, the doped-polymer film samples are mounted in the cryostat with vacuum conditions to avoid any degradation. The pump energy has been tuned to 10 nJ with beam focal size of 100 μm at the sample position. The representative measured 2D spectra for two differently processed films are presented here in figure 5.11.

The 2D spectra of solution-mixed processed film for T = 30 fs in figure 5.11 (a) shows a clear intense bleach peak marked as A, (ω_τ, ω_t) = (13000, 13000) cm^{-1} corresponding to $D_0 \rightarrow D_1$ transition of $\mathrm{F_4TCNQ}$ anion. In addition, a less intense feature at low energy is marked as B, (ω_τ, ω_t) = (12500, 12500) cm^{-1}. As discussed earlier in this chapter, this feature corresponds to the polymer polaron transition. The off diagonal features C (13000, 12500) cm^{-1} and D (12500, 13000) cm^{-1} confirms the excitionic coupling between the two observed transitions. In 2D spectrum at T = 50 fs, a sharp decrease in intensity for peak A can be easily be seen. The decrease in bleach intensity uncovers the excited state absorption at (ω_τ, ω_t) = (13600, 13000) cm^{-1}. Similarly, in 2D data for sequentially doped films shown in figure 5.11 (b), diagonal bleach peaks corresponding to $\mathrm{F_4TCNQ}$ anion and polymer polaron are observed as A' and B'. The off diagonal coupling peaks are marked as C' and D'. Surprisingly, D' off diagonal peak is more intense in the sequentially processed samples in contrast to solution-mixed film where peak C is more intense. To understand this observation, further input from theoretical modelling is needed. Additionally, for T = 50 fs in sequentially mixed film, 2D data does not show appreciable decay of intensity corresponding to A' peak. To get more insight to this observation, decay dynamics of A and A' peaks for respective samples are extracted and plotted in figure 5.12.
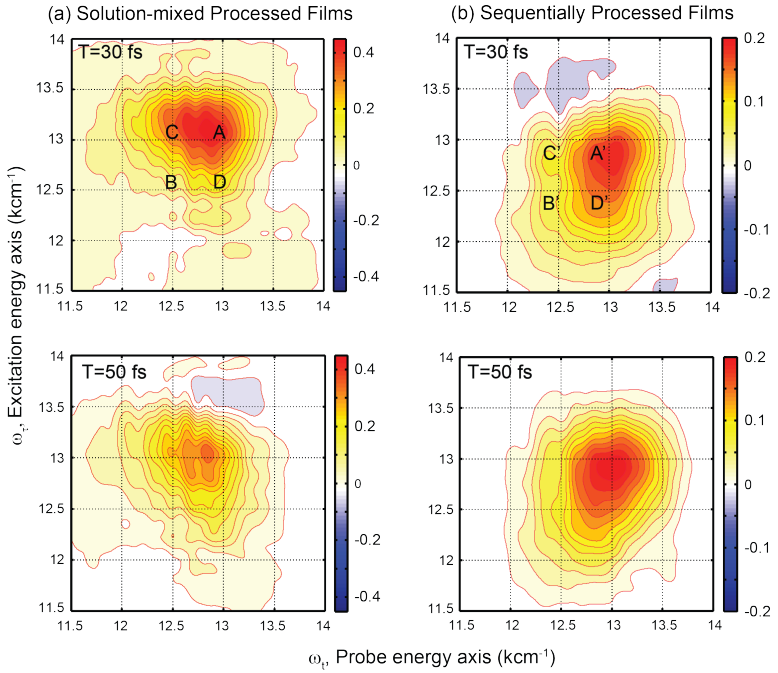
Figure 5.11: Two-dimensional electronic spectra (real part) of the PBTTT−F$_4$TCNQ films at the selected evolution times of 30 fs and 50 fs, obtained for two differently processed films: (a) solution-mixed processed films; and (b) sequentially processed films. Red peaks represent the photo-induced increase of the transmission due to the ground-state bleach and blue peaks corresponds to excited state absorption. Diagonal peaks A and B (A′ and B′ for sequentially processed film data) refers to the bleach signatures corresponding to transitions from F$_4$TCNQ anion and polymer polaron, respectively. The off-diagonal peaks C and D (C′ and D′ for sequentially processed film data) establish the presence of excitonically coupled electronic states of the PBTTT− F$_4$TCNQ.
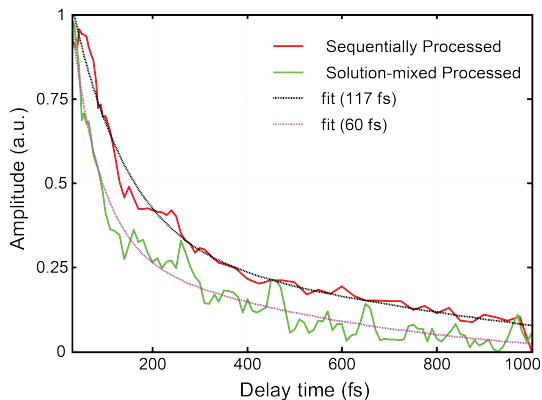
Figure 5.12: Comparison of decay dynamics of F_4TCNQ anion's bleach feature at A and A′ in figure 5.11. The kinetic traces have been fitted to a bi-exponential function shown as black traces. Sequentially processed film distinctly show the longer lifetime in comparison to solution-processed films.

The difference in the decays can easily be visualized. The decay dynamics of F_4TCNQ anion diagonal features are fitted with bi-exponential function. Sequentially processed film clearly shows slower dynamics with major component of ∼117 fs, whereas solution-processed film has ∼60 fs as major component. It must be noted here that the fast component in decay dynamics of D_1 state has been interpreted as π-stacked dopant-polymer population in precursor solution mixtures. In solution, the time component was found to be ∼30 fs. Considering that the strongly modulated lifetime of D_1 state is due to the π-stack interaction between dopant and polymer, the changes in lifetimes from solution to film directly signifies the differential interaction strengths amongst ion-pair. Even for two differently processed films, these interaction strengths vary a lot. It is a very interesting observation, which needs further input

from theoretical modelling to extract the nature and strength of interaction strengths.

5.8   Conclusions

Despite of various experimental study to obtain structural insight of spin-casted molecular doped organic semiconductors, our understanding towards evolution of polymer-dopant interactions during the spin-casting process is limited. In this chapter, I employed two-dimensional electronic spectroscopy to reveal heterogeneous ion-pair interactions in precursor solution mixture of prototypical $P3HT - F_4TCNQ$ system in chlorobenzene. The two-dimensional electronic photon echo spectroscopic measurements captured the electronic interactions amongst the ion-pair via unique signatures off diagonal coupling peaks. In addition, the dynamics of the D_1 state of F_4TCNQ anion showed bi-exponential decay with time constants: 30 and 200 fs (instead of expected mono-exponential decay) signifying presence of heterogeneously interacting ion-pairs. The 2DES data on $PBTTT - F_4TCNQ$ also showed electronically coupled dopant population with bi-exponential decay of the D_1 state of F_4TCNQ anion. With the help of MD simulations (performed by our collaborators) on 1:1 solution mixture of $P3HT - F_4TCNQ$ in chlorobenzene and quantum chemistry calculations, we have obtained three dominant interaction modes with different vibronic coupling strengths: 75 cm^{-1} for side-chain, 150 cm^{-1} for π-stack, and 69 cm^{-1} for slipped stack. The time-resolved measurements on systematically modified side-chain length in polymers revealed preferential selection of population with π-stack mode of interaction in shorter alkyl side-chain lengths. Systematic variation of excitonic coupling strength in π-stack interaction with alkyl chain length was also observed. Additionally, I probed these interactions in differently processed films. The D_1 state of F_4TCNQ anion showed slower decay dynamics in sequentially processed films as compared to solution-mixed films. Thus, this study provides a detailed analysis of the

possible nature and strengths of electronic interactions amongst ion-pair in precursor solutions and films of molecular doped polymers. It will be interesting to explore how these seed-interactions evolve during the spin-casting process, and what physical parameters dictate the retention of one interaction mode over other in films. We envision that capitalizing on this quantitative structural understanding of the seed-interactions in precursor solutions, one may think of possible ways to achieve desirable interactions in the spin-casted films, and hence improve the doping efficiency.

Chapter 6

Photocatalysis: role of entasis in prototypical Cu(I) phenanathroline complex

Driving efficient photo-redox chemical transformations is the key for the development of new cost-effective as well as environmentally benign synthetic methods. Copper(I) based photocatalysts with low toxicity and highly negative oxidation potentials have shown great promise to be efficient photocatalysts. In this chapter, I have studied the effect of entasis (with strained geometry) in excited state dynamics of prototypical copper(I) based photocatalyst in single crystals. Using femtosecond broadband transient absorption spectroscopy, I observe that the triplet generation from entactic state is faster in crystals ($\sim$5 ps) unlike solution, where the intersystem crossing is slower ($\sim$10 ps) leading to loss of excited state population via competing internal conversion process. The effect of entasis on vibrationally coherent photoinduced Jahn-Teller distortion timescale has been discussed as well. The results presented in this chapter may inspire synthesis of novel Cu(I) complexes with intelligent ligand design and/or

encapsulation of the complexes in porous supramolecular hosts. This will the pave the way towards minimizing the undesired structural distortions in excited state leading to efficient generation of catalytic triplet state.

6.1 Introduction

The concept of entasis has long been applied to explain the efficient catalysis or electron transfer in the metal active sites of metalloproteins.[197–199] It signifies a structural pre-distortion in a transition metal complex, which energizes the reactive state of the system.[200, 201] This conceptualization has attracted numerous scientific communities, especially bioinorganic chemists. Inspired by the success of this conceptual framework, Galperin and Koonin have proposed its far-reaching impacts on evolution, stating the emergence of each separate entactic state as a key evolutionary incident.[202] Each such event might have allowed catalysis of a new class of efficient reactions. Now a days, the idea of entactic state is even extended to enzymes without metals to envision the role of strain in enzymes for efficient enzymatic catalysis.[203]

The higher reactivity of the entatic geometry is due to the elevated energy levels of the reactive as well as the product states with respect to the transition state.[200] This conceptual framework has been depicted in figure 6.1. The elevation in the energy level can be caused by various forms of stresses (solvation or crystal lattice effects) or strains (ligand backbones). The use of these different factors in energizing the reactive state has been an active area of research.

In transition metal complexes, copper-based systems are most intensively studied group to understand the role of entactic state. Most of the synthetic 'entactic state' complexes of copper emulate blue copper proteins, which display fast electron transfer believably due to the entasis.[204, 205] Employing the strain with novel ligand designs, the Cu(II/I) model complexes have been synthesized and studied extensively.[206–209]
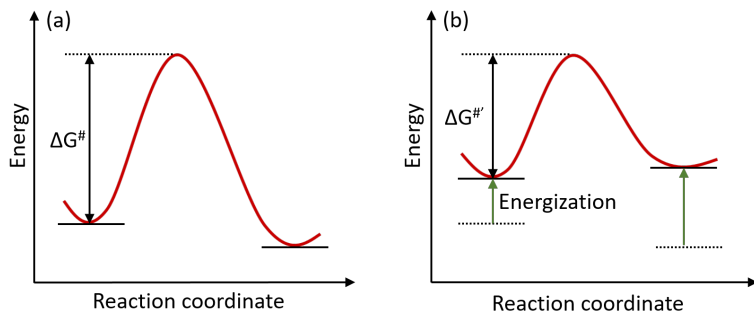
Figure 6.1: Conceptual illustration of entasis induced energization of the reactant state. (a) normal reaction, (b) reaction where reactant is energized to decrease the activation energy.

Recently, Dahl and Szymczak synthesized a nearly square-planar Cu(I) complex.[210] Policar and colleagues have designed sugar-based ligands to achieve pre-organization for Cu(II), but with Cu(I) oxidation state.[211] Herres-Pawlis and colleagues have also reported series of bis(chelate) Cu(I) and Cu(II) guanidine-quinoline complex cations with entatic geometry.[206] They have also studied the effect of ligand induced strained entactic state in excited state structural evolution.[212] Most studies reported in the literature focus mainly on the strained induced entactic state. The effect of stresses induced by crystal lattice in photoinduced Jahn-Teller distortion dynamics in Cu(I)-based complexes has not been explored yet.

Here, I have presented the excited state dynamics of bis(diimine)copper(I) complex (shown in figure 6.3(a)) in single crystals. In crystalline state, this complex shows pre-twisted configuration towards Cu(II) geometry. Therefore, it makes this molecule a model 'entatic state' system to understand the effect of lattice induced stress in structural relaxation. Using femtosecond transient absorption measurements,

I captured the faster structural dynamics of this complex in crystals as compared to solution. Additionally, the affected evolution of triplet state in crystals has also been discussed.

6.2 Material and methods

6.2.1 Sample preparation

$[Cu(dmphen)_2]PF_6$ was prepared by the method reported in the literature.[213] All the materials were used as received from Sigma Aldrich. Purification of the sample was checked by absorption and NMR. Dichloromethane (Sigma) and Methanol (Sigma) solvents were used for static and transient measurements. The absorbance of the sample for used for optical measurements was set to be 1 OD. The stability of the sample checked by comparing static absorption before and after the measurement. Fresh sample was prepared for every measurement.

The $[Cu(dmp)_2]^+$ crystals for the optical experiments were grown in-house and sliced to sections thinner of 400 nm. The crystal obtained from synthesis were recrystallized in dichloromethane (DCM). The new crystals obtained were better in size for transient studies. In order to cut the crystals of desired thickness, a conventional crystal thinning technique was used, called ultramicrotomy.[214] The ultramicrotome equipment in our lab is shown in figure 6.2. The thin microtomed sections were mounted on quartz substrate for measurements. The stability of the crystals was checked by recording absorption before and after measurements.

6.2.2 Experimental conditions

All measurements done in this chapter were performed on the transient absorption set-up described in Chapter-2. The pump-pulse used excites $S_1 \leftarrow S_0$ transition, which
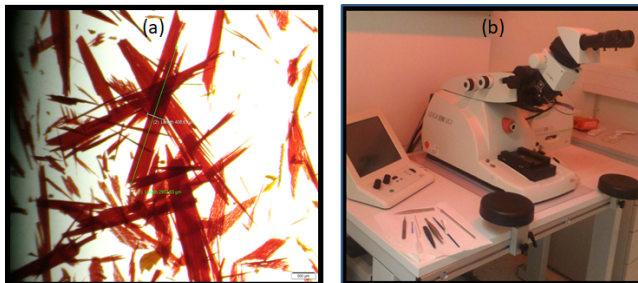
Figure 6.2: Picture of $[Cu(dmp)_2]^+$ crystal (a) and ultramicrotome in Miller's lab (b). It can be use to cut crystals down to 50 nm thickness.

corresponds to the MLCT (metal-to-ligand charge transfer) band. Time-resolved absorption spectra were measured with $\sim$200-fs time resolution. The solution measurement was done in 1 mm quartz cuvette. In order to avoid damage and keep sample fresh during the measurement the cuvette was mounted on a motorized shaker. To have good S/N ratio data 600-800 spectra was averaged for each time delay. The energy of the pump power was attenuated to avoid nonlinear artefacts. To have data consistency experiments were repeated multiple times on different samples. All measurements were performed at room temperature.

6.3   Results

The synthesized $[Cu(dmp)_2]^+$ was dissolved in methanol and the solution was measured for its absorption spectrum. Figure 6.3(b) shows the absorption spectrum of the complex (red trace) in the visible region. It displays two absorption bands around $\sim$454 nm and a broad shoulder on the red edge at $\sim$550 nm. In literature, both the absorption bands are assigned to MLCT transitions.[215,216] The weak MLCT transi-

134
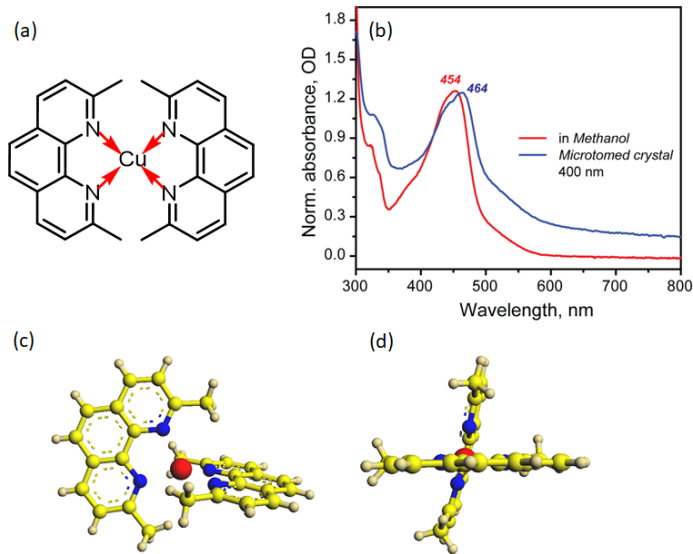
Figure 6.3: $[\text{Cu(dmp)}_2]^+$: Bis(2,9-dimethyl-1,10-phenanthroline)copper(I). (a) Molecular structure, (b) absorption spectra of the copper complex dissolved in methanol (red) and 400 nm thin microtomed crystal (blue). The intense absorption spectral feature shifts from 454 nm in solution to 464 nm in crystal ($S_2 \leftarrow S_0$ transition). Weak lower energy absorption band at $\sim$550 nm corresponds to $S_1 \leftarrow S_0$ transition. Both these transition have MLCT character in visible part of the spectrum . The crystal structure of the molecule is shown with top view (c) and side view (d).

tion at $\sim$550 nm (A_2 state) is assigned to $S_1 \leftarrow S_0$, which essentially is an optically forbidden transition. The observed transition intensity in this feature is due to the effect of nuclear displacement in S_1 state. The intense higher energy absorption band at $\sim$454 nm (B_2 state) is due to the optically allowed $S_2 \leftarrow S_0$ transition. These assignments have also been supported by recent TDDFT calculations.[217,218] In crys-

talline state, $[\mathrm{Cu(dmp)_2}]^+$ exists in pre-twisted configuration, as shown in figure 6.3(c) and (d). Now because, the dihedral angle is close to 80° (79.4°) and not 90° as imposed in D_{2d}, the symmetry lowers to D_2 geometry resulting into relaxation in the selection rule.[219,220] In fact, it is well known that the distorted structure in copper complexes show more intense $S_1 \leftarrow S_0$ transition.[217] To observe this effect in $[\mathrm{Cu(dmp)_2}]^+$ crystals, the absorption spectrum of the ~400 nm thin microtomed slices of the crystal is presented in figure 6.3(b) as blue line. As expected, the $S_1 \leftarrow S_0$ transition shows intensity that is more prominent in crystals as compared to solution. In addition, this feature seems broader in crystals, but the scattering background makes it difficult to convince myself. The intense $S_2 \leftarrow S_0$ transition is apparently red-shifted to 464 nm in crystals. This might be due to the differential Franck-Condon overlap caused by the distortion in the ground state geometry.

6.3.1   Transient absorption measurement

Various research groups have studied the ultrafast dynamics of Cu(I)-based complexes of this complexes in solution using various spectroscopic tools.[221−226] In a pioneering work by Tahara and co-workers, they used femtosecond transient absorption spectroscopy to unravel the dynamics of the $[\mathrm{Cu(dmp)}]_2$ complex (same system that has been discussed in this chapter) after exciting MLCT state (S_1) at 550 nm.[224] They have observed two distinct processes: structural change, D_{2d} (perpendicular) $\rightarrow D_2$ (flattened) and subsequent intersystem crossing, $S_1 \leftarrow T_1$. These two processes have been shown to have well-separated timescales: ~0.8 ps and ~10 ps for structural change and intersystem crossing respectively. Here I have presented the femtosecond transient absorption measurements on the same complex after subjecting the system with photoexcitation at 515 nm in solution as well as in crystals.

Figure 6.4(a) represents transient absorption spectra of $[\mathrm{Cu(dmp)_2}]^+$ in solution
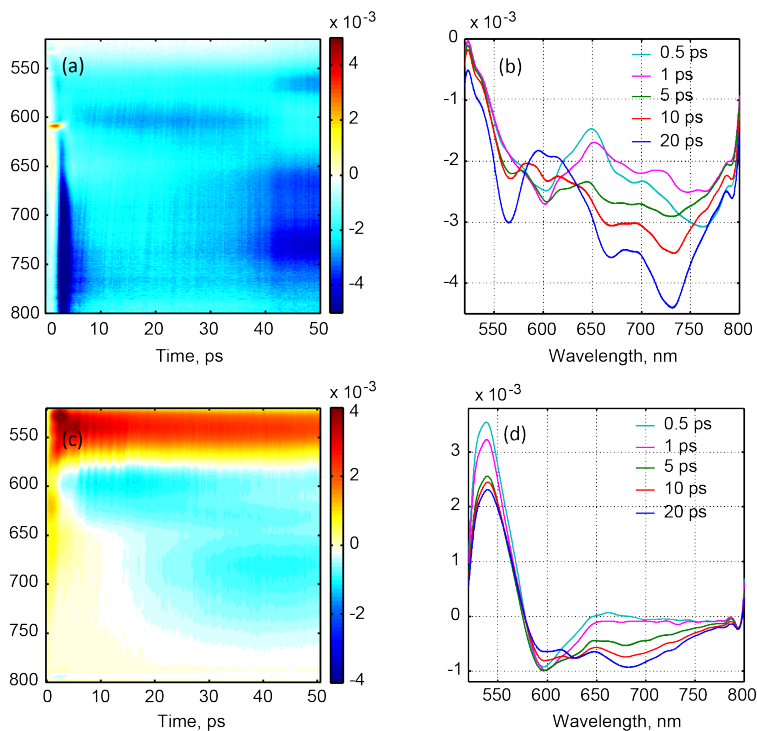
Figure 6.4: Transient absorption spectrum of $[Cu(dmp)_2]^+$ in solution (a) and in 400 nm thin crystal (c). Spectral evolution at selected time delays have also been plotted for solution (b) and crystal (d).

after excitation at 515 nm. The spectral traces for selected time points have also been plotted in figure 6.4(b). Largely, all the spectral features observed here have been identified by earlier reports on this complex. Excited state absorption (ESA) band at 600 nm is assigned to absorption from S_1 to higher energy levels. ESA

features at ∼725 nm, ∼660 nm and ∼565 nm are T_1 absorption bands to T_2, T_3 and T_4 respectively. The global fitting of the data reveals ∼610 fs lifetime of the perpendicular S_1 state, which is in contrast to ∼920 fs observed by Tahara and co-workers.[224] Similarly, the lifetime of the flattened S_1 state has been extracted here as ∼8.9 ps, which is slightly shorter than the lifetime of 9.8 ps report by Tahara and co-workers.[224] This inconsistency can be explained based on the difference in initial photoexcitation energies. In the experiment present in this chapter, excitation at 515 nm provides the vibrational excess energy in the S_1 state generated, which may cause the observed change in the time constants.

The transient absorption spectrum of ∼400 nm thin $[\text{Cu(dmp)}_2]^+$ crystals has been presented in figure 6.4(c). The spectral evolution at different time points are also plotted as figure 6.4(d). One distinctly observed feature is the ground state bleach at ∼540 nm. The observation of the feature clearly suggests that the $S_1 \leftarrow S_0$ transition band in $[\text{Cu(dmp)}_2]^+$ crystals are more intense as compared to the solution due to the pre-twisting in the crystals. Similar to solution studies, a excited state absorption feature at ∼595 nm can be seen to be generated just after photoexcitation. Hence, this band can be assigned to absorption from S_1 to higher energy levels. As this ESA feature at ∼595 nm decays, the rise of two ESA features at 625 and 685 nm are seen to rise subsequently. A less prominent feature at 730 nm can also be seen. These ESA features should correspond to triplet state, T_1 absorption. To assign these features convincingly to specific transition needs further support from electronic structure calculations. The global fit of the data reveals ∼350 fs lifetime of the perpendicular S_1 state and ∼6 ps lifetime of the flattened S_1 state. The cause and implications of these observed lifetimes have been described later in the discussion section.

6.3.2   Coherent nuclear dynamics

In figure 6.5(a), the TA spectrum with positive (ground state bleach feature centered at 535 nm) and negative bands (excited state absorption centered at 595 nm) is presented. The time step used for the measurements in this window is 5 fs. As described earlier, the ESA feature centered at 595 nm corresponds to the absorption from S_1 to higher energy levels. The oscillations over the dynamics of transient features are clearly visible in both the regions of the spectrum. As a representative trace, the kinetics of the GSB is shown as red line in figure 6.5(b). A strong oscillation overriding the kinetic decay captures the underlying vibrational frequency. The associated exponential fitting for the kinetic decay is presented as black dashed line. To retrieve the observed dominant coherent vibrational mode, Fourier transform analysis of the residual (blue trace in figure 6.5(b)) after removing the decay components is performed. The power spectrum so obtained is plotted here in figure 6.5(c). A frequency of $\sim$101 cm^{-1} is observed with high amplitude. Another dominant frequency is $\sim$10 cm^{-1}. To retrieve the vibrational frequencies from the different regions of the TA spectrum, the TA data is globally fit. The residuals obtained after subtracting the kinetic fits are further analyzed using Fourier transformation over the entire spectrum. The retrieved 2D vibrational frequency map consisting of the GSB and the ESA regions are shown in figure 6.5(d). The identified low-frequency modes are: 13 and 101 cm^{-1}. The observed mode at 101 cm^{-1} has been assigned in the literature to the 'breathing' mode of the complex, which involves symmetric stretching of the Cu-N bond.

To retrieve the evolution of the ground and excited state frequencies in time, I have analyzed the data from the GSB and ESA regions using the wavelet analysis. The spectra obtained for the GSB and ESA regions are shown in figure 6.6 (a) and (b), respectively. Both the spectra show strong magnitude oscillations around 100 cm^{-1}.
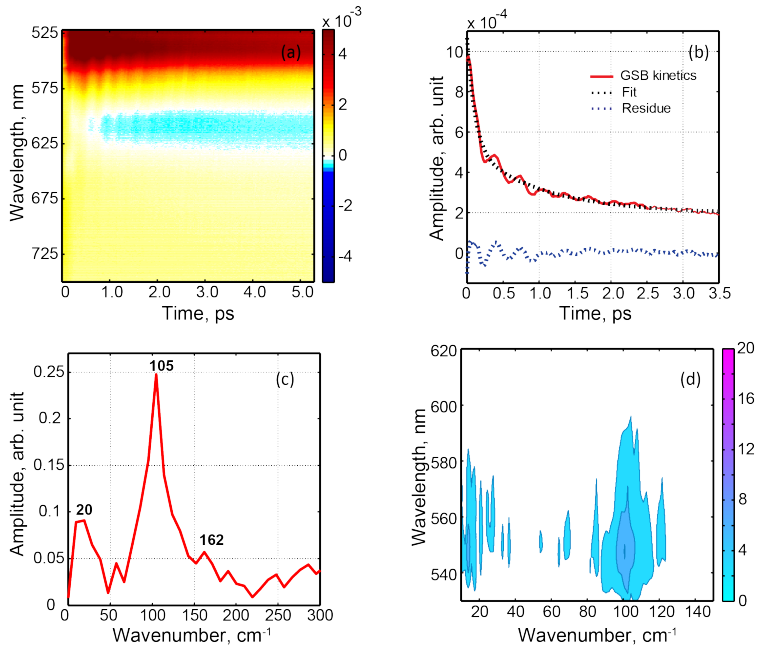
Figure 6.5: Frequency analysis: (a) measured transient absorption spectrum of $[Cu(dmp)_2]^+$ crystals with a time step of 5 fs. The GSB (red) and ESA (blue) regions clearly show the oscillations. (b) The kinetics of the GSB is shown as red line. The associated exponential fitting curve is presented as black dashed line. The obtained residual is shown as blue solid line at the bottom. (c) Fourier transfer has been performed to examine the vibrations. The obtained power spectrum is presented here. (d) 2D frequency map obtained after performing the Fourier transformation on the residuals of the globally fitted data.

Interestingly, the anti-correlated oscillations from the GSB and ESA demonstrate the separation of vibrations from the electronic ground and excited states. Tahara and co-workers also argued for a well-defined vibrational structure for the perpendicular S_1 state in their studies on solution. Hence, coherence in the ESA region corresponds to the perpendicular S_1 state vibrational frequencies.
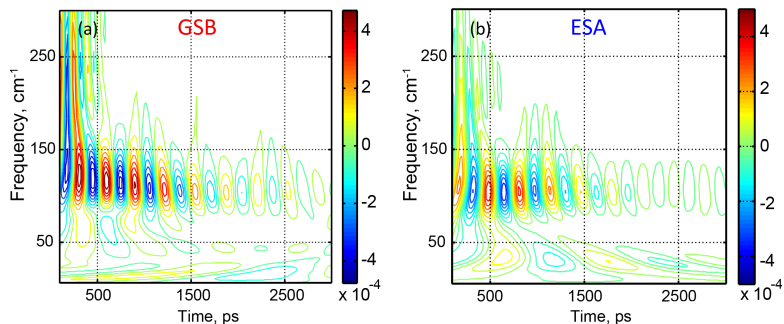
Figure 6.6: Wavelet analysis of residuals from (a) ground state bleach, GSB and (b) excited state absorption, ESA.

6.4   Discussion

The observed short lifetimes of perpendicular S_1 state ($\sim$350 fs) and flattened S_1 state ($\sim$6 ps) in $[\mathrm{Cu(dmp)_2}]^+$ crystals clearly demonstrates the huge implications of the lattice stress induced entasis on excited state population dynamics. The faster Jahn-Teller structural distortion timescales can easily be understood considering that copper complex in crystalline state exists in a pre-organized geometry for Cu(II) to be formed after excitation at MLCT band. Thus, the system needs lesser reorganization after photo-induced charge transfer event. On the other hand, the observed shorter

lifetime of the flattened S_1 state is possibly due to a cumulative effect of faster internal conversion to ground state and faster triplet formation. The later process can happen if the so-called flattened S_1 state have distortion from square planar geometry. This will result into different spin-orbit coupling (SOC) between relaxed S_1 to T_1 states in crystals and solution. Earlier report work on $[Cu(dmp)_2]^+$ have revealed that the Franck-Condon geometry has SOC of ~300 cm^{-1} between S_1 and T_1.[217] For the geometry after structural distortion, SOC value is only ~30 cm^{-1}. Thus, faster triplet formation must be caused by the hindered planarization of the ligand in crystal lattice, which results into relaxed S_1 state in crystals with higher SOC value. In that case, relaxed S_1 state in crystals (with partially flattened geometry) would also be higher in energy as compared to the relaxed S_1 state in solution. The proposed mechanism described here needs to be tested using other experimental and theoretical tools.

6.5   Conclusion

In this chapter, I have presented a detailed time-resolved studies on $[Cu(dmp)_2]^+$ crystals using femtosecond transient absorption measurements. In crystals, $[Cu(dmp)_2]^+$ exists in entactic state, which exists due to the presence of lattice induced stresses. The effect of entactic state is extremely noticeable in the observed dynamics in the excited state. The photoinduced Jahn-Teller distortion timescale decreases in crystals, which curtail the timescale of FC perpendicular S_1 state to ~350 fs as compared to ~800 fs in solution. The underlying coherent vibrational dynamics during structural distortions have also been presented. In addition, the observed shorter lifetime of the flattened S_1 state (~6 ps) hints towards the possible existence of distorted square planar geometry as the minima of the S_1 state. This cause faster generation of triplet state in crystals. Hence, the study presented in this chapter reveal how the lattice induced entasis effect the excited state dynamics of Cu(I)-based complexes. The lattice

stress induced fast triplet generation presented in this work can be used as a guiding principle to design the Cu(I)-based metal-organic frameworks to performed triplet-state based photocatalysis. Lattice stresses can be engineered in these frameworks to obtain higher yields of triplet states, which is the primary photocatalytic state used in Cu(I)-based catalysis.

Chapter 7

Conclusion and outlook

The need for efficient materials for solar light harvesting has motivated the research towards novel material design. However, this pursuit of the ideal material has mostly been intended using combinatorial approach, which is guided by the macroscopic parameters like device efficiency or turnover frequency of catalytic reaction. These macroscopic parameters hide the specific details towards the reasons for the success or failure of the material system. Gathering the precise understanding towards underlying electronic and structural transitions would guide us towards rational design principles for next generation of materials. Within this thesis, I have studied the photoinduced processes underlying charge generation in natural and celebrated artificial materials.

To gather understanding from natural systems, I have probed the isolated photosystem II reaction center (PSII RC) and observed the charge separation dynamics at cryogenic temperature of 20 K. The work described in chapter 3 unravel the complex multiphasic charge separation phenomena in RC complex. The time-constant of primary charge separation was retrieved to be $\sim$3.8 ps. Additionally, I have assessed the role of electronic and vibrational coherences during the energy transfer step. In liter-

ature, controversy exists regarding the assignments of electronic coherence in natural photosynthetic complexes. The work presented in the chapter 3 using 2DES clearly resolve the electronic coherences ($\sim$600 fs for radical pair and $\sim$400 fs for the electron donor and acceptor at initial time) in PSII RC at biologically non-relevant low temperature of 20 K. The observed long-lived oscillations at 37 and 80 cm^{-1} correspond to the vibrational coherences.

In chapter 4, I have probed the functional role of the vibrational coherences in hybrid perovskite photophysics. Hybrid organic-inorganic perovskites are the most celebrated amongst contemporary materials for photovoltaics. The photoinduced charges in perovskite ($CH_3NH_3PbI_3$) have ultrafast dephasing time constants suggesting strong interaction to the phonon modes. This leads to polaron formation in organic-inorganic perovskites, though the exact mechanism of this process was not completely known. Particularly, the role of organic part in perovskite photphysics was never unraveled. The study presented in this chapter uncover the interplay of libration mode of methyl cation with phonon modes corresponding to inorganic octahedra that reorganize the perovskite lattice to localize charges leading to polaron formation. This study signifies the role of methyl cation as more than a filler and vibrational insight gained can be useful in designing the modern perovskite based solar cells.

Once charges are generated, they need to be transported to their respective electrodes in photovoltaics or photocatalytic cells. The efficient charge transport needs favorable coupling of molecular system with the electrode surface. In chapter 5, I have studied the one of the prototypical material systems that are actively used as electron transport layers in photovoltaics: molecular doped conjugated polymers. Poor doping efficiency in these class of materials limit the electron conductivity. With the work present in this chapter, I have gathered quantitative understanding of ion-pair interactions in molecular-doped polymers. The nature and strength of these ion-pair interac-

tions holds the key towards efficient conductivities. Combination of two-dimensional spectroscopy and broadband transient absorption spectroscopies measurements on prototypical F_4TCNQ doped P3HT/PBTTT polymers unraveled the possibility of retained memory for ion-pairs from solution to processed films. Excited state lifetime of the F_4TCNQ anions uncovers the existence of heterogeneous interactions in solution. To explore the dopant-side chain interactions, I have described the systematic study where the polymer-dopant solution mixtures are probed with varying polymer side chain lengths. This study highlights that long side chains prevents the excitonic coupling among the polymer and dopants electronic states. Finally, this chapter provides the insight to the differential conductivities observed for same polymer-dopant system prepared using different processing methods.

Moving on from photovoltaics to photocatalysis, I have studied the photoinduced Jahn-Teller distortion in prototypical $[Cu(dmp)_2]^+$ system in microtomed single crystals in chapter 6. This chapter unravels the role of lattice strain induced entasis in copper(I) photophysics. The TA measurements on the crystals reveal modulated structural relaxation dynamics of $\sim$350 fs as compared to $\sim$800 fs in solution. In addition, the intersystem crossing is faster in crystals with entactic geometry than in solution. I also captured the vibrational coherences that possibly drives the phtoinduced Jahn-Teller distortion in the system. Hence, the work presented in chapter details the lattice induced entasis effect on the excited state dynamics of $[Cu(dmp)_2]^+$.

Outlook

In this thesis, I have emphasized on the fundamental understanding of charge generation and transport processes in molecular materials, in order to enable surpass their existing performance in electronic devices. Charge generation followed by charge transfer process imposes structural changes in the materials. These changes include

electronic as well as nuclear displacement (length of displacement is system dependent). As described in this thesis, I was able to capture the electronic changes using state-of-the art techniques like 2-D electronic and transient experiments. Despite the astonishing success of these methods to capture electronic and/or vibrational coherences, the precise understanding of the accompanying structural changes during the charge generation processes remain elusive. I envision that the theoretical modelling of these ultrafast dynamical processes by novel methods may pave the way towards their detail understanding. However, at the same time, the advanced experimental techniques should also drive our understanding at atomistic level, beyond the conventional validation of the underlying kinetics. Since structural information can be directly translated to the rational designing of molecular materials, mapping nuclear motions by diffraction-based methods will help us to gain the necessary details of the processes. This can be achieved by employing synchronized femtosecond optical excitation laser pulses with a femtosecond pulsed x-ray or electron sources. The optical pulse triggers the structural change while the x-ray or electron source observes the atomic motions involved on the relevant time scales. These experiments will provide unprecedented understanding towards the processes. In addition, I would like to emphasize that the results of this thesis are major breakthroughs in the material systems studied. The understanding gained from this thesis can be directly be used to design novel molecular materials from labs to industry, but still many promises lies ahead in this crusade. In case of doped-polymers systems, I propose to use excited state lifetime of F_4TCNQ anion as a tool to probe the interaction in dopant-polymer. Rather than using the macroscopic parameter like conductivity, lifetime imaging experiments can be used as routine to test quality of the processed films. The structural handle (using NMR or diffraction-based techniques) on the polymer-dopant interaction will further help the chemists to come with rational strategies.

147

Appendix A

2D Spectrum analysis

A.1 Global fitting approach

Multidimensional global fits of both experimental arrays of 2D spectra were performed in accordance with the available algorithm developed in our group.[125] A detailed description of the technique can be found in the work reported earlier.[227] In this method, a sequence of 2D spectra taken at different waiting times T are collected to form a three-dimensional array $S(\omega_\tau, \omega_t, T)$. This 3D array is then decomposed into a sum of two-dimensional decay-associated spectra $A_i(\omega_\tau, \omega_t)$ with individual exponential decays of correspondingly associated life times τ_i according to

$$S(\omega_\tau, \omega_t, T) = \sum_i A_i(\omega_\tau, \omega_t) \exp(-T/\tau_i). \tag{A.1}$$

We apply the global fitting to the 2D electronic spectra of perovskite.

A.2 Correlation analysis in 2D electronic spectra

To verify the origin of the oscillations observed in the 2D spectra, we have performed a cross-correlation analysis of the residuals across diagonal $\omega_\tau = \omega_t$. To quantify the

correlation, we have calculated the correlation coefficients C between the residuals R for each pair of conjugated spectral positions in the delay time window up to 2 ps. The delay time steps were equally distributed with dt = 15 fs and the correlation coefficients are given by

$$C(\omega_t, \omega_\tau) = corr(R(\omega_t, \omega_\tau, T), R(\omega_\tau, \omega_t, T)), \qquad (A.2)$$

where corr evaluates the correlation with respect to T. This yields a 2D correlation spectrum.

Appendix B

Fourier Transformation

B.1 Tukey-window Fourier transform

Here, we provide the details related to the Fourier transform using Tukey window. To isolate the high-frequency jitters, Fourier filtering in the frequency domain is employed. By this, we isolate each of these regions of interest with a Tukey window, which has the form

$$\omega(n) = \begin{cases} 1, & 0 \leq |n| \leq \alpha \frac{N}{2}\,, \\ \frac{1}{2}\left(1 + \cos\left[\frac{\pi(n-\alpha\frac{N}{2})}{(1-\alpha)\frac{N}{2}}\right]\right), & \alpha \frac{N}{2} \leq |n| \leq \frac{N}{2}\,. \end{cases} \tag{B.1}$$

Due to the flat top, it conserves the amplitudes of the Fourier components of interest over a larger frequency range than a cosine or a Gaussian window, while it still limits the artifacts arising from a pure bandpass filter. In this work, we use the Tukey window with $\alpha = 1/5$ and a Fourier bandpass filter with ≤ 700 cm^{-1}.

Appendix C

Frequency analysis

C.1 Wavelet analysis

In this section, we summarize the technical principles of the wavelet transform. The details have been reported before.[228, 229] It starts from the definition of a zero mean and a short-time oscillating function ψ, called a "mother" wavelet, which is used to decompose a one- or multi-dimensional real-valued signal into different frequency bands. This mother wavelet function is translated in time by t and stretched by the scale of ω^{-1}, giving the wavelet "atom" function

$$\psi_{t,\omega}(t') = \sqrt{\omega}\psi([t' - t]\omega).$$ (C.1)

It provides the effective basis for the transformation. The two most common transforms are the discrete wavelet transform and the continuous wavelet transform.[230] The discrete one decomposes the signal into several frequency bands and is frequently used for data and image compression. The continuous one, which is used in this paper, is based on an expansion of a temporal signal $f(t)$ via the inner product of the function

with a wavelet atom and reads

$$CWT_f(t, \omega) = \int_{-\infty}^{+\infty} dt' f(t') \sqrt{\omega} \psi^*([t' - t]\omega) \,. \qquad \text{(C.2)}$$

The parameter t indicates where the wavelet atom is centered, while the scale parameter ω^{-1} controls the relative width of the wavelet atom compared to the mother wavelet function. This nonlinear integral transform provides a high *time* resolution of high-frequency components, while for the slowly varying components of the signal, the *frequency* resolution is high. It projects the signal onto basis functions with a varying "center" frequency and a varying range fixed by the scaling factor.

Appendix D

List of hazardous substances

List of the hazardous substances used in the work. They are marked as p (precaution-ary) and (hazardous) as per Global Harmonised System (GHS) with in the European Union (EU):

GHS07 Harmful   GHS08 Health hazard   GHS02 Flammable

GHS04 Compressed gas   GHS01 Explosive   GHS06 Toxic

GHS05 Corrosive   GHS03 Oxidising   GHS09 Environmental hazard

Substance	H-statement(s)	P-statement(s)	GHS Labelling
Copper (II) sulphate	302, 315, 319, 410	280, 373, 301+312 302+352 305+351+338	
Chlorobenzene	226, 315, 332, 411	210, 273, 302+352 304+340+312	
Dichloromethane	315, 319, 336, 351	201,302,352 305+350+338	
PBTTT-C12	Non-hazardous	Non-hazardous	-
Poly(3-hexyl-thiophene-2,5-diyl)	261	261, 305+351+338	
Poly(3-butyl thiophene-2,5-diyl)	Non-hazardous	Non-hazardous	-
Poly(3-dodecyl thiophene-2,5-diyl)	Non-hazardous	Non-hazardous	-
2,3,5,6-Tetrafluoro-7,7,8,8- tetracyano-quinodimethane	301+311+331	301+310+330 302+352+312 304+340+311	
Methanol	225, 301+311+331	210, 233, 280 301+310 303+361+353 304+340+311	
Lithium acetate hydrate	319	280-305+351+338	
2,9-Dimethyl-1,10-phenanthroline	Non-hazardous	Non-hazardous	-
Sodium hexa-fluorophosphate	302+312+332, 314	280, 305+351+338 310	
L-Ascorbic acid	Non-hazardous	Non-hazardous	-

154

Bibliography

[1] B. J. Kim, S. Lee, and H. S. Jung, "Recent progressive efforts in perovskite solar cells toward commercialization," *Journal of Materials Chemistry A*, vol. 6, pp. 12215–12236, jul 2018.

[2] N. Nelson and A. Ben-Shem, "The complex architecture of oxygenic photosynthesis," *Nature Reviews Molecular Cell Biology*, vol. 5, pp. 971–982, 2004.

[3] W. Junge, "Oxygenic photosynthesis: History, status and perspective," *Quarterly Reviews of Biophysics*, vol. 52, pp. 1–17, 2019.

[4] D. Gust and T. A. Moore, "Mimicking photosynthesis," *Science*, vol. 244, pp. 35–41, 1989.

[5] A. I. Hochbaum and P. Yang, "Semiconductor nanowires for energy conversion," *Chemical Reviews*, vol. 110, pp. 527–546, 2010.

[6] D. Gust, T. A. Moore, and A. L. Moore, "Realizing artificial photosynthesis," *Faraday Discussions*, vol. 155, pp. 9–26, 2012.

[7] Y. Wang, H. Suzuki, J. Xie, O. Tomita, D. J. Martin, M. Higashi, D. Kong, R. Abe, and J. Tang, "Mimicking Natural Photosynthesis: Solar to Renewable H2 Fuel Synthesis by Z-Scheme Water Splitting Systems," *Chemical Reviews*, vol. 118, pp. 5201–5241, 2018.

[8] D. K. Dogutan and D. G. Nocera, "Artificial Photosynthesis at Efficiencies Greatly Exceeding That of Natural Photosynthesis," *Accounts of Chemical Research*, vol. 52, p. 3143â3148, 2019.

[9] C. S. Ponseca, P. Chábera, J. Uhlig, P. Persson, and V. Sundström, "Ultrafast Electron Dynamics in Solar Energy Conversion," *Chemical Reviews*, vol. 117, pp. 10940–11024, 2017.

[10] S. Hammes-Schiffer and A. A. Stuchebrukhov, "Theory of coupled electron and proton transfer reactions," *Chemical Reviews*, vol. 110, pp. 6939–6960, dec 2010.

[11] E. F. Aziz, A. Vollmer, S. Eisebitt, W. Eberhardt, P. Pingel, D. Neher, and N. Koch, "Localized charge transfer in a molecularly doped conducting polymer," *Advanced Materials*, vol. 19, pp. 3257–3260, 2007.

[12] Alan J. Heeger, "Semiconducting and Metallic Polymers: The Fourth Generation of Polymeric Materials (Nobel Lecture)," *Angewandte Chemie - International Editionte Chemie International edition*, vol. 40, pp. 2591–2611, 2001.

[13] T. W. Kelley, P. F. Baude, C. Gerlach, D. E. Ender, D. Muyres, M. A. Haase, D. E. Vogel, and S. D. Theiss, "Recent progress in organic electronics: Materials, devices, and processes," *Chemistry of Materials*, vol. 16, pp. 4413–4422, 2004.

[14] K. Walzer, B. Männig, M. Pfeiffer, and K. Leo, "Highly efficient organic devices based on electrically doped transport layers," *Chemical Reviews*, vol. 107, pp. 1233–1271, 2007.

[15] B. Lüssem, M. Riede, and K. Leo, "Doping of organic semiconductors," *Physica Status Solidi (A) Applications and Materials Science*, vol. 210, pp. 9–43, 2013.

[16] A. K. Bakhshi, "Electrically conducting polymers: from fundamental to applied research," *Bulletin of Materials Science*, vol. 18, pp. 469–495, 1995.

[17] T. J. Skotheim, *Handbook of Conducting Polymers (Third edition)*. 1997.

[18] N. Basescu, Z. X. Liu, D. Moses, A. J. Heeger, H. Naarmann, and N. Theophilou, "High electrical conductivity in doped polyacetylene," *Nature*, vol. 327, pp. 403–405, 1987.

[19] A. J. Heeger, S. Kivelson, J. R. Schrieffer, and W. P. Su, "Solitons in conducting polymers," *Reviews of Modern Physics*, vol. 60, pp. 781–850, jul 1988.

[20] C. K. Chiang, C. R. Fincher, Y. W. Park, A. J. Heeger, H. Shirakawa, E. J. Louis, S. C. Gau, and A. G. MacDiarmid, "Electrical conductivity in doped polyacetylene," *Physical Review Letters*, vol. 39, pp. 1098–1101, 1977.

[21] J.-L. Bredas, J. E. Norton, J. Cornil, and V. Coropceanu, "Molecular understanding of organic solar cells: the challenges," *Accounts of chemical research*, vol. 42, pp. 1691–1699, 2009.

[22] L. Zhu, E. G. Kim, Y. Yi, and J. L. Brédas, "Charge transfer in molecular complexes with 2,3,5,6-tetrafluoro-7,7,8,8- tetracyanoquinodimethane (F4-TCNQ): A density functional theory study," *Chemistry of Materials*, vol. 23, pp. 5149–5159, 2011.

[23] B. Dereka, M. Koch, and E. Vauthey, "Looking at Photoinduced Charge Transfer Processes in the IR: Answers to Several Long-Standing Questions," *Accounts of Chemical Research*, vol. 50, pp. 426–434, 2017.

[24] M. M. Lee, J. Teuscher, T. Miyasaka, T. N. Murakami, and H. J. Snaith, "Efficient Hybrid Solar Cells Based on Meso-Superstructured Organometal Halide Perovskites," *Science*, vol. 338, pp. 643–647, 2010.

[25] J. H. Im, C. R. Lee, J. W. Lee, S. W. Park, and N. G. Park, "6.5% efficient perovskite quantum-dot-sensitized solar cell," *Nanoscale*, vol. 3, pp. 4088–4093, 2011.

[26] H. S. Kim, C. R. Lee, J. H. Im, K. B. Lee, T. Moehl, A. Marchioro, S. J. Moon, R. Humphry-Baker, J. H. Yum, J. E. Moser, M. Grätzel, and N. G. Park, "Lead iodide perovskite sensitized all-solid-state submicron thin film mesoscopic solar cell with efficiency exceeding 9%," *Scientific Reports*, vol. 2, pp. 1–7, 2012.

[27] J. H. Noh, S. H. Im, J. H. Heo, T. N. Mandal, and S. I. Seok, "Chemical management for colorful, efficient, and stable inorganic-organic hybrid nanostructured solar cells," *Nano Letters*, vol. 13, pp. 1764–1769, 2013.

[28] P. K. Nayak, S. Mahesh, H. J. Snaith, and D. Cahen, "Photovoltaic solar cell technologies: analysing the state of the art," *Nature Reviews Materials*, vol. 4, pp. 269–285, 2019.

[29] K. Galkowski, A. Mitioglu, A. Miyata, P. Plochocka, O. Portugall, G. E. Eperon, J. T. W. Wang, T. Stergiopoulos, S. D. Stranks, H. J. Snaith, and R. J. Nicholas, "Determination of the exciton binding energy and effective masses for methylammonium and formamidinium lead tri-halide perovskite semiconductors," *Energy and Environmental Science*, vol. 9, pp. 962–970, 2016.

[30] A. Kojima, K. Teshima, Y. Shirai, and T. Miyasaka, "Organometal halide perovskites as visible-light sensitizers for photovoltaic cells," *Journal of the American Chemical Society*, vol. 131, pp. 6050–6051, 2009.

[31] J. J. Choi and S. J. Billinge, "Perovskites at the nanoscale: From fundamentals to applications," *Nanoscale*, vol. 8, pp. 6206–6208, 2016.

[32] J. Huang, Y. Yuan, Y. Shao, and Y. Yan, "Understanding the physical properties of hybrid perovskites for photovoltaic applications," *Nature Reviews Materials*, vol. 2, pp. 1–19, 2017.

[33] Y. Shao, Y. Yuan, and J. Huang, "Correlation of energy disorder and open-circuit voltage in hybrid perovskite solar cells," *Nature Energy*, vol. 1, pp. 1–6, jan 2016.

[34] C. Eames, J. M. Frost, P. R. Barnes, B. C. O'Regan, A. Walsh, and M. S. Islam, "Ionic transport in hybrid lead iodide perovskite solar cells," *Nature Communications*, vol. 6, pp. 1–8, 2015.

[35] I. Deretzis, E. Smecca, G. Mannino, A. La Magna, T. Miyasaka, and A. Alberti, "Stability and Degradation in Hybrid Perovskites: Is the Glass Half-Empty or Half-Full?," *Journal of Physical Chemistry Letters*, vol. 9, pp. 3000–3007, 2018.

[36] P. Lotfabadi, "Analyzing passive solar strategies in the case of high-rise building," *Renewable and Sustainable Energy Reviews*, vol. 52, pp. 1340–1353, 2015.

[37] D. Ravelli, D. Dondi, M. Fagnoni, and A. Albini, "Photocatalysis. A multifaceted concept for green chemistry," *Chemical Society Reviews*, vol. 38, pp. 1999–2011, 2009.

[38] P. J. Boddy, "Oxygen Evolution on Semiconducting TiO2," *Journal of The Electrochemical Society*, vol. 115, p. 199, 1968.

[39] A. Fujishima and K. Honda, "Electrochemical photolysis of water at a semiconductor electrode," *Nature*, vol. 238, pp. 37–38, 1972.

[40] K. J. Young, L. A. Martini, R. L. Milot, R. C. Snoeberger, V. S. Batista, C. A. Schmuttenmaer, R. H. Crabtree, and G. W. Brudvig, "Light-driven water

oxidation for solar fuels," *Coordination Chemistry Reviews*, vol. 256, pp. 2503–2520, 2012.

[41] O. S. Wenger, "Is Iron the New Ruthenium?," *Chemistry - A European Journal*, vol. 25, pp. 6043–6052, 2019.

[42] P. Chábera, Y. Liu, O. Prakash, E. Thyrhaug, A. E. Nahhas, A. Honarfar, S. Essén, L. A. Fredin, T. C. Harlang, K. S. Kjær, K. Handrup, F. Ericson, H. Tatsuno, K. Morgan, J. Schnadt, L. Häggström, T. Ericsson, A. Sobkowiak, S. Lidin, P. Huang, S. Styring, J. Uhlig, J. Bendix, R. Lomoth, V. Sundström, P. Persson, and K. Wärnmark, "A low-spin Fe(III) complex with 100-ps ligand-to-metal charge transfer photoluminescence," *Nature*, vol. 543, pp. 695–699, 2017.

[43] A. Britz, W. Gawelda, T. A. Assefa, L. L. Jamula, J. T. Yarranton, A. Galler, D. Khakhulin, M. Diez, M. Harder, G. Doumy, A. M. March, É. Bajnóczi, Z. Németh, M. Pápai, E. Rozsályi, D. Sárosiné Szemes, H. Cho, S. Mukherjee, C. Liu, T. K. Kim, R. W. Schoenlein, S. H. Southworth, L. Young, E. Jakubikova, N. Huse, G. Vankó, C. Bressler, and J. K. McCusker, "Using Ultrafast X-ray Spectroscopy to Address Questions in Ligand-Field Theory: The Excited State Spin and Structure of [Fe(dcpp)2]2+," *Inorganic Chemistry*, vol. 58, pp. 9341–9350, 2019.

[44] A. Schinabeck, M. J. Leitl, and H. Yersin, "Dinuclear Cu(I) Complex with Combined Bright TADF and Phosphorescence. Zero-Field Splitting and Spin-Lattice Relaxation Effects of the Triplet State," *Journal of Physical Chemistry Letters*, vol. 9, pp. 2848–2856, 2018.

[45] M. Maiuri, M. Garavelli, and G. Cerullo, "Ultrafast Spectroscopy: State of the Art and Open Challenges," *Journal of the American Chemical Society*, vol. 142, pp. 3–15, 2020.

[46] B. J. Siwick, J. R. Dwyer, R. E. Jordan, and R. J. Miller, "An Atomic-Level View of Melting Using Femtosecond Electron Diffraction," *Science*, vol. 302, pp. 1382–1385, 2003.

[47] A. R. Attar, A. Bhattacherjee, C. D. Pemmaraju, K. Schnorr, K. D. Closser, D. Prendergast, and S. R. Leone, "Femtosecond x-ray spectroscopy of an electrocyclic ring-opening reaction," *Science*, vol. 356, pp. 54–59, 2017.

[48] R. J. Dwayne Miller, "Mapping atomic motions with ultrabright electrons: The chemists' gedanken experiment enters the lab frame," *Annual Review of Physical Chemistry*, vol. 65, pp. 583–604, 2014.

[49] T. Ishikawa, S. A. Hayes, S. Keskin, G. Corthey, M. Hada, K. Pichugin, A. Marx, J. Hirscht, K. Shionuma, K. Onda, Y. Okimoto, S.-y. Koshihara, T. Yamamoto, H. Cui, M. Nomura, Y. Oshima, M. Abdel-Jawad, R. Kato, and R. J. D. Miller, "Direct observation of collective modes coupled to molecular orbital-driven charge transfer," *Science*, vol. 350, pp. 1501–1506, 2015.

[50] Y. Tian, A. Merdasa, M. Peter, M. Abdellah, K. Zheng, C. S. Ponseca, T. Pullerits, A. Yartsev, V. Sundström, and I. G. Scheblykin, "Giant photoluminescence blinking of perovskite nanocrystals reveals single-trap control of luminescence," *Nano Letters*, vol. 15, pp. 1603–1608, 2015.

[51] Y. Tian, A. Merdasa, E. Unger, M. Abdellah, K. Zheng, S. Mckibbin, A. Mikkelsen, T. Pullerits, A. Yartsev, V. Sundström, and I. G. Scheblykin, "Enhanced Organo-Metal Halide Perovskite Photoluminescence from Nanosized

Defect-Free Crystallites and Emitting Sites," *Journal of Physical Chemistry Letters*, vol. 6, pp. 4171–4177, 2015.

[52] A. Merdasa, M. Bag, Y. Tian, E. Källman, A. Dobrovolsky, and I. G. Scheblykin, "Super-resolution luminescence microspectroscopy reveals the mechanism of photoinduced degradation in CH3NH3PbI3 perovskite nanocrystals," *Journal of Physical Chemistry C*, vol. 120, pp. 10711–10719, 2016.

[53] H. Yuan, E. Debroye, G. Caliandro, K. P. Janssen, J. Van Loon, C. E. Kirschhock, J. A. Martens, J. Hofkens, and M. B. Roeffaers, "Photoluminescence Blinking of Single-Crystal Methylammonium Lead Iodide Perovskite Nanorods Induced by Surface Traps," *ACS Omega*, vol. 1, pp. 148–159, 2016.

[54] M. Cho, "Two-Dimensional Optical Spectroscopy,"

[55] A. Tokmakoff, "NONLINEAR SPECTROSCOPY: Introduction," *http://home.uchicago.edu/˜tokmakoff/NLS/Notes/11.1.-4._Nonlinear_Spectroscopy_4-09.pdf*, pp. 1–43, 2009.

[56] A. H. Zewail, "Femtochemistry: Atomic-scale dynamics of the chemical bond," *Journal of Physical Chemistry A*, vol. 104, pp. 5660–5694, 2000.

[57] A. Rosspeintner, B. Lang, and E. Vauthey, "Ultrafast photochemistry in liquids," *Annual Review of Physical Chemistry*, vol. 64, pp. 247–271, 2013.

[58] P. J. Walla, "Ultrafast- and Nonlinear Spectroscopy," *Modern Biophysical Chemistry*, pp. 257–284, jun 2014.

[59] K. Kreher, "Ultrafast Spectroscopy of Semiconductors and Semiconductor Nanostructures," *Zeitschrift für Physikalische Chemie*, vol. 202, pp. 300–300, 1997.

[60] Y. Tanimura and S. Mukamel, "Two-dimensional femtosecond vibrational spectroscopy of liquids," *The Journal of Chemical Physics*, vol. 99, pp. 9496–9511, 1993.

[61] K. Park and M. Cho, "Time- and frequency-resolved coherent two-dimensional IR spectroscopy: Its complementary relationship with the coherent two-dimensional Raman scattering spectroscopy," *Journal of Chemical Physics*, vol. 109, pp. 10559–10569, 1998.

[62] S. H. Lin, A. A. Villaeys, and Y. Fujimura, *Advances in multi-photon processes and spectroscopy*, vol. 23 of *Advances in Multi-Photon Processes and Spectroscopy*. WORLD SCIENTIFIC, 2016.

[63] S. Mukamel, "Multidimensional femtosecond correlation spectroscopies of electronic and vibrational excitations," *Annual Review of Physical Chemistry*, vol. 51, pp. 691–729, 2000.

[64] R. W. Boyd, *Non-linear optics*. 2007.

[65] E. Vauthey, "Introduction to nonlinear optical spectroscopic techniques for investigating ultrafast processes," *Univ. of Geneva*, pp. 1–40, 2006.

[66] R. A. Baumgartner And, "Optical I Parametric Amplification," tech. rep., OPA1979, 1979.

[67] S. Mukamel, *Principles of non linear optical spectroscopy*. 1995.

[68] P. Hamm, "Principles of Nonlinear Optical Spectroscopy : A Practical Approach or : Mukamel for Dummies," 2005.

[69] A. Nitzan, *Chemical Dynamics in Condensed Phases*. 2006.

[70] A. J. Nathan and A. Scobell, *Quantun Chemistry*, vol. 91. 2012.

[71] P. Atkins and R. Friedman, "Molecular Quantum Mechanics Fourth Edition," *Oxford University Press New York*, p. 588, 2005.

[72] S. E. Braslavsky, "Glossary of terms used in photochemistry 3rd edition: (IU-PAC Recommendations 2006)," *Pure and Applied Chemistry*, vol. 79, pp. 293–465, 2007.

[73] M. Kasha, "Characteization of electronic transitions in complex molecules," *Discuss. Faraday Soc.*, vol. 9, pp. 14–19, 1950.

[74] R. Berera, R. van Grondelle, and J. T. Kennis, "Ultrafast transient absorption spectroscopy: Principles and application to photosynthetic systems," 2009.

[75] C. Ruckebusch, M. Sliwa, P. Pernot, A. de Juan, and R. Tauler, "Comprehensive data analysis of femtosecond transient absorption spectra: A review," *Journal of Photochemistry and Photobiology C: Photochemistry Reviews*, vol. 13, pp. 1–27, 2012.

[76] T. Brixner, T. Mancal, I. V. Stiopkin, and G. R. Fleming, "Phase-stabilized two-dimensional electronic spectroscopy," *Journal of Chemical Physics*, vol. 121, pp. 4221–4236, 2004.

[77] D. M. Jonas, "Two -Dimensional Femtosecond Spectroscopy," *Annual Review of Physical Chemistry*, vol. 54, pp. 425–463, 2003.

[78] V. I. Prokhorenko, A. Halpin, and R. D. Miller, "Coherently-controlled two-dimensional photon echo electronic spectroscopy," *Optics Express*, vol. 17, p. 9764, 2009.

[79] R. L. Fork, C. H. Brito Cruz, P. C. Becker, and C. V. Shank, "Compression of optical pulses to six femtoseconds by using cubic phase compensation," *Optics Letters*, vol. 12, p. 483, 1987.

[80] E. Miesak and R. Negres, "Alignment Procedure for a Dual Grating Pulse Compressor," *Applied Optics*, vol. 37, p. 8146, 1998.

[81] E. H. G. Backus, S. Garrett-Roe, and P. Hamm, "Phasing problem of heterodyne-detected two-dimensional infrared spectroscopy," *Optics Letters*, vol. 33, p. 2665, 2008.

[82] A. D. Bristow, D. Karaiskaj, X. Dai, and S. T. Cundiff, "All-optical retrieval of the global phase for two-dimensional Fourier-transform spectroscopy," *Optics Express*, vol. 16, p. 18017, 2008.

[83] S. M. Faeder and D. M. Jonas, "Two-dimensional electronic correlation and relaxation spectra: Theory and model calculations," *Journal of Physical Chemistry A*, vol. 103, pp. 10489–10505, 1999.

[84] D. J. Vinyard, G. M. Ananyev, and G. Charles Dismukes, "Photosystem II: The reaction center of oxygenic photosynthesis," *Annual Review of Biochemistry*, vol. 82, pp. 577–606, 2013.

[85] Y. Umena, K. Kawakami, J. R. Shen, and N. Kamiya, "Crystal structure of oxygen-evolving photosystem II at a resolution of 1.9Å," *Nature*, vol. 473, pp. 55–60, 2011.

[86] J. Deisenhofer, O. Epp, K. Miki, R. Huber, and H. Michel, "Structure of the protein subunits in the photosynthetic reaction centre of Rhodopseudomonas viridis at 3 resolution," *Nature*, vol. 318, pp. 618–624, 1985.

[87] V. I. Prokhorenko and A. R. Holzwarth, "Primary processes and structure of the photosystem II reaction center: A photon echo study," *Journal of Physical Chemistry B*, vol. 104, pp. 11563–11578, 2000.

[88] W. Arnold and R. K. Clayton, "The first step in photosynthesis: evidence for its electronic nature," *Proceedings of the National Academy of Sciences*, vol. 46, pp. 769–776, 1960.

[89] S. R. Greenfield and M. R. Wasielewski, "Excitation energy transfer and charge separation in the isolated Photosystem II reaction center," *Photosynthesis Research*, vol. 48, pp. 83–97, 1996.

[90] O. Nanba and K. Satoh, "Isolation of a photosystem II reaction center consisting of D-1 and D-2 polypeptides and cytochrome b-559," *Proceedings of the National Academy of Sciences*, vol. 84, pp. 109–112, 1987.

[91] M. Seibert and M. R. Wasielewski, "The isolated Photosystem II reaction center: First attempts to directly measure the kinetics of primary charge separation," *Photosynthesis Research*, vol. 76, pp. 263–268, 2003.

[92] M. R. Wasielewski, D. G. Johnson, Govindjee, C. Preston, and M. Seibert, "Determination of the primary charge separation rate in Photosystem II reaction centers at 15 K," *Photosynthesis Research*, vol. 22, no. 1, pp. 89–99, 1989.

[93] R. Jankowiak, D. Tang, G. J. Small, and M. Seibert, "Transient and persistent hole burning of the reaction center of photosystem II," *Journal of Physical Chemistry*, vol. 93, pp. 1649–1654, 1989.

[94] T. A. Roelofs, M. Gilbert, V. A. Shuvalov, and A. R. Holzwarth, "Picosecond fluorescence kinetics of the D1-D2-cyt-b-559 photosystem II reaction cen-

ter complex. Energy transfer and primary charge separation processes," *BBA - Bioenergetics*, vol. 1060, pp. 237–244, 1991.

[95] D. Tang, R. Jankowiak, M. Seibert, and G. J. Small, "Effects of detergent on the excited state structure and relaxation dynamics of the photosystem II reaction center: A high resolution hole burning study," *Photosynthesis Research*, vol. 27, pp. 19–29, 1991.

[96] A. R. Holzwarth, M. G. Müller, G. Gatzen, M. Hucke, and K. Griebenow, "Ultrafast spectroscopy of the primary electron and energy transfer processes in the reaction center of photosystem II," *Journal of Luminescence*, vol. 60-61, pp. 497–502, 1994.

[97] M. G. Müller, M. Hucke, M. Reus, and A. R. Holzwarth, "primary processes and structure of the photosystem ii reaction center. 4. low-intensity femtosecond transient absorption spectra of Dl-D2-cyt-b559 reaction centers," *Journal of Physical Chemistry*, vol. 100, no. 22, pp. 9527–9536, 1996.

[98] S. A. Merry, S. Kumazaki, Y. Tachibana, D. M. Joseph, G. Porter, K. Yoshihara, J. Barber, J. R. Durrant, and D. R. Klug, "Sub-picosecond equilibration of excitation energy in isolated photosystem II reaction centers revisited: Time-dependent anisotropy," *Journal of Physical Chemistry*, vol. 100, pp. 10469–10478, 1996.

[99] S. R. Greenfield, M. Seibert, Govindjee, and M. R. Wasielewski, "Direct measurement of the effective rate constant for primary charge separation in isolated photosystem II reaction centers," *Journal of Physical Chemistry B*, vol. 101, pp. 2251–2255, 1997.

[100] J. A. Leegwater, J. R. Durrant, and D. R. Klug, "Exciton equilibration induced by phonons: Theory and application to PS II reaction centers," *Journal of Physical Chemistry B*, vol. 101, pp. 7205–7210, 1997.

[101] M. L. Groot, J. P. Dekker, R. Van Grondelle, F. T. Den Hartog, and S. Völker, "Energy transfer and trapping in isolated photosystem II reaction centers of green plants at low temperature. A study by spectral hole burning," *Journal of Physical Chemistry*, vol. 100, pp. 11488–11495, 1996.

[102] S. R. Greenfield, M. Seibert, and M. R. Wasielewski, "Time-Resolved Absorption Changes of the Pheophytin Qx Band in Isolated Photosystem II Reaction Centers at 7 K: Energy Transfer and Charge Separation," *Journal of Physical Chemistry B*, vol. 103, pp. 8364–8374, 1999.

[103] R. J. Sension, B. Donovan, L. A. Walker, and C. F. Yocum, "Primary charge separation in photosystem II," *Springer Series in Chemical Physics*, vol. 62, pp. 340–341, 1996.

[104] L. M. Yoder, A. G. Cole, and R. J. Sension, "Structure and function in the isolated reaction center complex of Photosystem II: Energy and charge transfer dynamics and mechanism," 2002.

[105] A. Gelzinis, L. Valkunas, F. D. Fuller, J. P. Ogilvie, S. Mukamel, and D. Abramavicius, "Tight-binding model of the photosystem II reaction center: Application to two-dimensional electronic spectroscopy," *New Journal of Physics*, vol. 15, pp. 1–26, 2013.

[106] G. S. Engel, T. R. Calhoun, E. L. Read, T. K. Ahn, T. Mančal, Y. C. Cheng, R. E. Blankenship, and G. R. Fleming, "Evidence for wavelike energy trans-

fer through quantum coherence in photosynthetic systems," *Nature*, vol. 446, pp. 782–786, 2007.

[107] G. S. Schlau-Cohen, A. Ishizaki, T. R. Calhoun, N. S. Ginsberg, M. Ballottari, R. Bassi, and G. R. Fleming, "Elucidation of the timescales and origins of quantum electronic coherence in LHCII," *Nature Chemistry*, vol. 4, pp. 389–395, 2012.

[108] E. Collini, C. Y. Wong, K. E. Wilk, P. M. Curmi, P. Brumer, and G. D. Scholes, "Coherently wired light-harvesting in photosynthetic marine algae at ambient temperature," *Nature*, vol. 463, pp. 644–647, 2010.

[109] J. A. Myers, K. L. Lewis, F. D. Fuller, P. F. Tekavec, C. F. Yocum, and J. P. Ogilvie, "Two-dimensional electronic spectroscopy of the D1-D2-cyt b559 photosystem II reaction center complex," *Journal of Physical Chemistry Letters*, vol. 1, pp. 2774–2780, 2010.

[110] E. Romero, R. Augulis, V. I. Novoderezhkin, M. Ferretti, J. Thieme, D. Zigmantas, and R. Van Grondelle, "Quantum coherence in photosynthesis for efficient solar-energy conversion," *Nature Physics*, vol. 10, pp. 676–682, 2014.

[111] F. D. Fuller, J. Pan, A. Gelzinis, V. Butkus, S. S. Senlik, D. E. Wilcox, C. F. Yocum, L. Valkunas, D. Abramavicius, and J. P. Ogilvie, "Vibronic coherence in oxygenic photosynthesis," *Nature Chemistry*, vol. 6, pp. 706–711, 2014.

[112] H. G. Duan, V. I. Prokhorenko, R. J. Cogdell, K. Ashraf, A. L. Stevens, M. Thorwart, and R. J. Miller, "Nature does not rely on long-lived electronic quantum coherence for photosynthetic energy transfer," *Proceedings of the National Academy of Sciences of the United States of America*, vol. 114, pp. 8493–8498, 2017.

169

[113] J. A. Myers, K. L. Lewis, P. F. Tekavec, and J. P. Ogilvie, "Two-color two-dimensional Fourier transform electronic spectroscopy with a pulse-shaper," *Optics Express*, vol. 16, p. 17420, 2008.

[114] F. L. Hoch, "Low-tempersture absorption spectroscopy (Cryoabsorption Spectroscopy)," *J. Chem. Educ.*, vol. 32, pp. 469–472, 1955.

[115] S. Caffarri, R. KouÅil, S. Kereïche, E. J. Boekema, and R. Croce, "Functional architecture of higher plant photosystem II supercomplexes," *EMBO Journal*, vol. 28, pp. 3052–3063, 2009.

[116] S. Caffarri, R. Croce, L. Cattivelli, and R. Bassi, "A look within LHCII: Differential analysis of the Lhcb1-3 complexes building the major trimeric antenna complex of higher-plant photosynthesis," *Biochemistry*, vol. 43, pp. 9467–9476, 2004.

[117] H. G. Duan, V. I. Prokhorenko, E. Wientjes, R. Croce, M. Thorwart, and R. J. Miller, "Primary Charge separation in the Photosystem II reaction center revealed by a global analysis of the two-dimensional electronic spectra," *Scientific Reports*, vol. 7, pp. 1–9, 2017.

[118] J. D. Hybl, A. A. Ferro, and D. M. Jonas, "Two-dimensional Fourier transform electronic spectroscopy," *Journal of Chemical Physics*, vol. 115, pp. 6606–6622, 2001.

[119] M. Germano, C. C. Gradinaru, A. Y. Shkuropatov, I. H. Van Stokkum, V. A. Shuvalov, J. P. Dekker, R. Van Grondelle, and H. J. Van Gorkom, "Energy and Electron Transfer in Photosystem II Reaction Centers with Modified Pheophytin Composition," *Biophysical Journal*, vol. 86, pp. 1664–1672, 2004.

[120] J. R. Durrant, D. R. Klug, S. L. Kwa, R. Van Grondelle, G. Porter, and J. P. Dekker, "A multimer model for P680, the primary electron donor of photosystem II," *Proceedings of the National Academy of Sciences of the United States of America*, vol. 92, pp. 4798–4802, 1995.

[121] M. L. Groot, F. Van Mourik, C. Eijckelhoff, I. H. Van Stokkum, J. P. Dekker, and R. Van Grondelle, "Charge separation in the reaction center of photosystem II studied as a function of temperature," *Proceedings of the National Academy of Sciences of the United States of America*, vol. 94, pp. 4389–4394, 1997.

[122] J. R. Durrant, G. Hastings, Q. Hong, J. Barber, G. Porter, and D. R. Klug, "Determination of P680 singlet state lifetimes in photosystem two reaction centres," *Chemical Physics Letters*, vol. 188, pp. 54–60, 1992.

[123] J. A. Myers, K. L. Lewis, F. D. Fuller, P. F. Tekavec, C. F. Yocum, and J. P. Ogilvie, "Two-dimensional electronic spectroscopy of the D1-D2-cyt b559 photosystem II reaction center complex," *Journal of Physical Chemistry Letters*, vol. 1, pp. 2774–2780, 2010.

[124] E. Romero, I. H. Van Stokkum, V. I. Novoderezhkin, J. P. Dekker, and R. Van Grondelle, "Two different charge separation pathways in photosystem II," *Biochemistry*, vol. 49, pp. 4300–4307, 2010.

[125] H. G. Duan, V. I. Prokhorenko, E. Wientjes, R. Croce, M. Thorwart, and R. J. Miller, "Primary Charge separation in the Photosystem II reaction center revealed by a global analysis of the two-dimensional electronic spectra," *Scientific Reports*, vol. 7, pp. 1–9, 2017.

[126] H. M. Visser, M. L. Groot, F. Van Mourik, I. H. Van Stokkum, J. P. Dekker, and R. Van Grondelle, "Subpicosecond transient absorption difference spectroscopy

on the reaction center of photosystem II: Radical pair formation at 77 K," *Journal of Physical Chemistry*, vol. 99, no. 41, pp. 15304–15309, 1995.

[127] H. G. Duan, A. L. Stevens, P. Nalbach, M. Thorwart, V. I. Prokhorenko, and R. J. Miller, "Two-Dimensional Electronic Spectroscopy of Light-Harvesting Complex II at Ambient Temperature: A Joint Experimental and Theoretical Study," *Journal of Physical Chemistry B*, vol. 119, pp. 12017–12027, 2015.

[128] E. J. Peterman, H. Van Amerongen, R. Van Grondelle, and J. P. Dekker, "The nature of the excited state of the reaction center of photosystem II of green plants: A high-resolution fluorescence spectroscopy study," *Proceedings of the National Academy of Sciences of the United States of America*, vol. 95, pp. 6128–6133, 1998.

[129] W. S. Yang, J. H. Noh, N. J. Jeon, Y. C. Kim, S. Ryu, J. Seo, and S. I. Seok, "High-Performance Photovoltaic Perovskite Layers Fabricated through Intramolecular Exchange," *Science*, vol. 348, pp. 1234–1237, 2015.

[130] J. M. Ball, M. M. Lee, A. Hey, and H. J. Snaith, "Low-temperature processed meso-superstructured to thin-film perovskite solar cells," *Energy and Environmental Science*, vol. 6, pp. 1739–1743, 2013.

[131] N. J. Jeon, J. H. Noh, W. S. Yang, Y. C. Kim, S. Ryu, J. Seo, and S. I. Seok, "Compositional engineering of perovskite materials for high-performance solar cells," *Nature*, vol. 517, pp. 476–480, 2015.

[132] Y. Hou, E. Aydin, M. De Bastiani, C. Xiao, F. H. Isikgor, D. J. Xue, B. Chen, H. Chen, B. Bahrami, A. H. Chowdhury, A. Johnston, S. W. Baek, Z. Huang, M. Wei, Y. Dong, J. Troughton, R. Jalmood, A. J. Mirabelli, T. G. Allen, E. Van Kerschaver, M. I. Saidaminov, D. Baran, Q. Qiao, K. Zhu, S. De Wolf, and

E. H. Sargent, "Efficient tandem solar cells with solution-processed perovskite on textured crystalline silicon," *Science*, vol. 367, pp. 1135–1140, 2020.

[133] H. Zhu, Y. Fu, F. Meng, X. Wu, Z. Gong, Q. Ding, M. V. Gustafsson, M. T. Trinh, S. Jin, and X. Y. Zhu, "Lead halide perovskite nanowire lasers with low lasing thresholds and high quality factors," *Nature Materials*, vol. 14, pp. 636–642, 2015.

[134] Z. K. Tan, R. S. Moghaddam, M. L. Lai, P. Docampo, R. Higler, F. Deschler, M. Price, A. Sadhanala, L. M. Pazos, D. Credgington, F. Hanusch, T. Bein, H. J. Snaith, and R. H. Friend, "Bright light-emitting diodes based on organometal halide perovskite," *Nature Nanotechnology*, vol. 9, pp. 687–692, 2014.

[135] Q. Lin, A. Armin, P. L. Burn, and P. Meredith, "Filterless narrowband visible photodetectors," *Nature Photonics*, vol. 9, pp. 687–694, 2015.

[136] L. Etgar, P. Gao, Z. Xue, Q. Peng, A. K. Chandiran, B. Liu, M. K. Nazeeruddin, and M. Grätzel, "Mesoscopic CH 3NH 3PbI 3/TiO 2 heterojunction solar cells," *Journal of the American Chemical Society*, vol. 134, pp. 17396–17399, 2012.

[137] D. W. DeQuilettes, S. M. Vorpahl, S. D. Stranks, H. Nagaoka, G. E. Eperon, M. E. Ziffer, H. J. Snaith, and D. S. Ginger, "Impact of microstructure on local carrier lifetime in perovskite solar cells," *Science*, vol. 348, pp. 683–686, 2015.

[138] L. M. Herz, "How Lattice Dynamics Moderate the Electronic Properties of Metal-Halide Perovskites," *Journal of Physical Chemistry Letters*, vol. 9, pp. 6853–6863, 2018.

[139] M. Saba, F. Quochi, A. Mura, and G. Bongiovanni, "Excited State Properties of Hybrid Perovskites," *Accounts of Chemical Research*, vol. 49, pp. 166–173, 2016.

[140] K. Miyata, T. L. Atallah, and X. Y. Zhu, "Lead halide perovskites: Crystal-liquid duality, phonon glass electron crystals, and large polaron formation," 2017.

[141] K. Miyata, D. Meggiolaro, M. Tuan Trinh, P. P. Joshi, E. Mosconi, S. C. Jones, F. De Angelis, and X. Y. Zhu, "Large polarons in lead halide perovskites," *Science Advances*, vol. 3, pp. 1–9, 2017.

[142] A. Jha, H. G. Duan, V. Tiwari, P. K. Nayak, H. J. Snaith, M. Thorwart, and R. J. Dwayne Miller, "Direct Observation of Ultrafast Exciton Dissociation in Lead Iodide Perovskite by 2D Electronic Spectroscopy," *ACS Photonics*, vol. 5, pp. 852–860, 2018.

[143] S. A. Bretschneider, I. Ivanov, H. I. Wang, K. Miyata, X. Zhu, and M. Bonn, "Quantifying Polaron Formation and Charge Carrier Cooling in Lead-Iodide Perovskites," *Advanced Materials*, vol. 30, p. 1707312, 2018.

[144] B. J. Bohn, T. Simon, M. Gramlich, A. F. Richter, L. Polavarapu, A. S. Urban, and J. Feldmann, "Dephasing and Quantum Beating of Excitons in Methylam-monium Lead Iodide Perovskite Nanoplatelets," *ACS Photonics*, vol. 5, pp. 648–654, 2018.

[145] T. Ghosh, S. Aharon, L. Etgar, and S. Ruhman, "Free Carrier Emergence and Onset of Electron-Phonon Coupling in Methylammonium Lead Halide Per-ovskite Films," *Journal of the American Chemical Society*, vol. 139, pp. 18262–18270, 2017.

[146] J. Nishida, J. P. Breen, K. P. Lindquist, D. Umeyama, H. I. Karunadasa, and M. D. Fayer, "Dynamically Disordered Lattice in a Layered Pb-I-SCN Per-

ovskite Thin Film Probed by Two-Dimensional Infrared Spectroscopy," *Journal of the American Chemical Society*, vol. 140, pp. 9882–9890, 2018.

[147] M. J. P. Alcocer, T. Leijtens, L. M. Herz, A. Petrozza, and H. J. Snaith, "Electron-Hole Diffusion Lengths Exceeding Trihalide Perovskite Absorber," *Science*, vol. 342, pp. 341–344, 2013.

[148] H. Oga, A. Saeki, Y. Ogomi, S. Hayase, and S. Seki, "Improved understanding of the electronic and energetic landscapes of perovskite solar cells: High local charge carrier mobility, reduced recombination, and extremely shallow traps," *Journal of the American Chemical Society*, vol. 136, pp. 13818–13825, 2014.

[149] C. Wehrenfennig, M. Liu, H. J. Snaith, M. B. Johnston, and L. M. Herz, "Charge-carrier dynamics in vapour-deposited films of the organolead halide perovskite CH3NH3PbI3-xClx," *Energy and Environmental Science*, vol. 7, pp. 2269–2275, 2014.

[150] H. Zhu, K. Miyata, Y. Fu, J. Wang, P. P. Joshi, D. Niesner, K. W. Williams, S. Jin, and X. Y. Zhu, "Screening in crystalline liquids protects energetic carriers in hybrid perovskites," *Science*, vol. 353, pp. 1409–1413, 2016.

[151] T. Chen, W. L. Chen, B. J. Foley, J. Lee, J. P. Ruff, J. Y. Ko, C. M. Brown, L. W. Harriger, D. Zhang, C. Park, M. Yoon, Y. M. Chang, J. J. Choi, and S. H. Lee, "Origin of long lifetime of band-edge charge carriers in organicâinorganic lead iodide perovskites," *Proceedings of the National Academy of Sciences of the United States of America*, vol. 114, pp. 7519–7524, 2017.

[152] G. Batignani, G. Fumero, A. R. Srimath Kandada, G. Cerullo, M. Gandini, C. Ferrante, A. Petrozza, and T. Scopigno, "Probing femtosecond lattice dis-

placement upon photo-carrier generation in lead halide perovskite," *Nature Communications*, vol. 9, pp. 1–5, 2018.

[153] X. Wu, L. Z. Tan, X. Shen, T. Hu, K. Miyata, M. Tuan Trinh, R. Li, R. Coffee, S. Liu, D. A. Egger, I. Makasyuk, Q. Zheng, A. Fry, J. S. Robinson, M. D. Smith, B. Guzelturk, H. I. Karunadasa, X. Wang, X. Zhu, L. Kronik, A. M. Rappe, and A. M. Lindenberg, "Light-induced picosecond rotational disordering of the inorganic sublattice in hybrid perovskites," *Science Advances*, vol. 3, pp. 1–7, 2017.

[154] A. A. Bakulin, O. Selig, H. J. Bakker, Y. L. Rezus, C. Müller, T. Glaser, R. Lovrincic, Z. Sun, Z. Chen, A. Walsh, J. M. Frost, and T. L. Jansen, "Real-Time Observation of Organic Cation Reorientation in Methylammonium Lead Iodide Perovskites," *Journal of Physical Chemistry Letters*, vol. 6, pp. 3663–3669, 2015.

[155] O. Selig, A. Sadhanala, C. Müller, R. Lovrincic, Z. Chen, Y. L. Rezus, J. M. Frost, T. L. Jansen, and A. A. Bakulin, "Organic Cation Rotation and Immobilization in Pure and Mixed Methylammonium Lead-Halide Perovskites," *Journal of the American Chemical Society*, vol. 139, pp. 4068–4074, mar 2017.

[156] V. C. Taylor, D. Tiwari, M. Duchi, P. M. Donaldson, I. P. Clark, D. J. Fermin, and T. A. Oliver, "Investigating the Role of the Organic Cation in Formamidinium Lead Iodide Perovskite Using Ultrafast Spectroscopy," *Journal of Physical Chemistry Letters*, vol. 9, pp. 895–901, 2018.

[157] M. Park, N. Kornienko, S. E. Reyes-Lillo, M. Lai, J. B. Neaton, P. Yang, and R. A. Mathies, "Critical Role of Methylammonium Librational Motion in Methylammonium Lead Iodide (CH3NH3PbI3) Perovskite Photochemistry," *Nano Letters*, vol. 17, pp. 4151–4157, 2017.

[158] F. Ambrosio, J. Wiktor, F. De Angelis, and A. Pasquarello, "Origin of low electron-hole recombination rate in metal halide perovskites," *Energy and Environmental Science*, vol. 11, pp. 101–105, 2018.

[159] Y. Zhang, F. Huang, and Q. Mi, "Preferential facet growth of methylammonium lead halide single crystals promoted by halide coordination," *Chemistry Letters*, vol. 45, pp. 1030–1032, 2016.

[160] N. K. Noel, S. N. Habisreutinger, B. Wenger, M. T. Klug, M. T. HïÂ¿Â½rantner, M. B. Johnston, R. J. Nicholas, D. T. Moore, and H. J. Snaith, "A low viscosity, low boiling point, clean solvent system for the rapid crystallisation of highly specular perovskite films," *Energy and Environmental Science*, vol. 10, pp. 145–152, 2017.

[161] J. M. Richter, F. Branchi, F. Valduga De Almeida Camargo, B. Zhao, R. H. Friend, G. Cerullo, and F. Deschler, "Ultrafast carrier thermalization in lead iodide perovskite probed with two-dimensional electronic spectroscopy," *Nature Communications*, vol. 8, pp. 1–7, 2017.

[162] D. M. Monahan, L. Guo, J. Lin, L. Dou, P. Yang, and G. R. Fleming, "Room-Temperature Coherent Optical Phonon in 2D Electronic Spectra of CH3NH3PbI3Perovskite as a Possible Cooling Bottleneck," *Journal of Physical Chemistry Letters*, vol. 8, pp. 3211–3215, 2017.

[163] V. Butkus, D. Zigmantas, L. Valkunas, and D. Abramavicius, "Vibrational vs. electronic coherences in 2D spectrum of molecular systems," *Chemical Physics Letters*, vol. 545, pp. 40–43, 2012.

[164] D. Egorova, "Self-analysis of coherent oscillations in time-resolved optical signals," *Journal of Physical Chemistry A*, vol. 118, pp. 10259–10267, 2014.

[165] H.-G. Duan, V. Tiwari, A. Jha, G. R. Berdiyorov, A. Akimov, O. Vendrell, P. K. Nayak, H. J. Snaith, M. Thorwart, Z. Li, M. E. Madjet, and R. J. D. Miller, "Photoinduced Vibrations Drive Ultrafast Structural Distortion in Lead Halide Perovskite," *JACS*, vol. 142, pp. 16569–16578, 2020.

[166] M. Park, A. J. Neukirch, S. E. Reyes-Lillo, M. Lai, S. R. Ellis, D. Dietze, J. B. Neaton, P. Yang, S. Tretiak, and R. A. Mathies, "Excited-state vibrational dynamics toward the polaron in methylammonium lead iodide perovskite," *Nature Communications*, vol. 9, pp. 1–9, 2018.

[167] P. Guo, A. Mannodi-Kanakkithodi, J. Gong, Y. Xia, C. C. Stoumpos, D. H. Cao, B. T. Diroll, J. B. Ketterson, G. P. Wiederrecht, T. Xu, M. K. Chan, M. G. Kanatzidis, and R. D. Schaller, "Infrared-pump electronic-probe of methylammonium lead iodide reveals electronically decoupled organic and inorganic sublattices," *Nature Communications*, vol. 10, pp. 1–8, 2019.

[168] M. Sendner, P. K. Nayak, D. A. Egger, S. Beck, C. Müller, B. Epding, W. Kowalsky, L. Kronik, H. J. Snaith, A. Pucci, and R. Lovrinčić, "Optical phonons in methylammonium lead halide perovskites and implications for charge transport," *Materials Horizons*, vol. 3, pp. 613–620, 2016.

[169] I. Salzmann and G. Heimel, "Toward a comprehensive understanding of molecular doping organic semiconductors (review)," *Journal of Electron Spectroscopy and Related Phenomena*, vol. 204, pp. 208–222, 2015.

[170] I. Salzmann, G. Heimel, M. Oehzelt, S. Winkler, and N. Koch, "Molecular Electrical Doping of Organic Semiconductors: Fundamental Mechanisms and Emerging Dopant Design Rules," *Accounts of Chemical Research*, vol. 49, no. 3, pp. 370–378, 2016.

[171] I. E. Jacobs and A. J. Moulé, "Controlling Molecular Doping in Organic Semiconductors," *Advanced Materials*, vol. 29, pp. 1–39, 2017.

[172] W. Gao and A. Kahn, "Controlled p-doping of zinc phthalocyanine by coevaporation with tetrafluorotetracyanoquinodimethane: A direct and inverse photoemission study," *Applied Physics Letters*, vol. 79, pp. 4040–4042, 2001.

[173] K. H. Yim, G. L. Whiting, C. E. Murphy, J. J. Halls, J. H. Burroughes, R. H. Friend, and J. S. Kim, "Controlling electrical properties of conjugated polymers via a solution-based p-type doping," *Advanced Materials*, vol. 20, pp. 3319–3324, 2008.

[174] D. T. Duong, C. Wang, E. Antono, M. F. Toney, and A. Salleo, "The chemical and structural origin of efficient p-type doping in P3HT," *Organic Electronics*, vol. 14, pp. 1330–1336, 2013.

[175] P. Pingel and D. Neher, "Comprehensive picture of p-type doping of P3HT with the molecular acceptor F4TCNQ," *Physical Review B - Condensed Matter and Materials Physics*, vol. 87, p. 115209, 2013.

[176] I. E. Jacobs, E. W. Aasen, J. L. Oliveira, T. N. Fonseca, J. D. Roehling, J. Li, G. Zhang, M. P. Augustine, M. Mascal, and A. J. Moulé, "Comparison of solution-mixed and sequentially processed P3HT:F4TCNQ films: Effect of doping-induced aggregation on film morphology," *Journal of Materials Chemistry C*, vol. 4, pp. 3454–3466, 2016.

[177] J. Fuzell, I. E. Jacobs, S. Ackling, T. F. Harrelson, D. M. Huang, D. Larsen, and A. J. Moulé, "Optical Dedoping Mechanism for P3HT:F4TCNQ Mixtures," *Journal of Physical Chemistry Letters*, vol. 7, pp. 4297–4303, 2016.

179

[178] F. M. McFarland, C. M. Ellis, and S. Guo, "The Aggregation of Poly(3-hexylthiophene) into Nanowires: With and without Chemical Doping," *Journal of Physical Chemistry C*, vol. 121, pp. 4740–4746, 2017.

[179] H. Hase, K. O'Neill, J. Frisch, A. Opitz, N. Koch, and I. Salzmann, "Unraveling the Microstructure of Molecularly Doped Poly(3-hexylthiophene) by Thermally Induced Dedoping," *Journal of Physical Chemistry C*, vol. 122, pp. 25893–25899, 2018.

[180] J. Gao, E. T. Niles, and J. K. Grey, "Aggregates promote efficient charge transfer doping of Poly(3- hexylthiophene)," *Journal of Physical Chemistry Letters*, vol. 4, pp. 2953–2957, 2013.

[181] B. Neelamraju, K. E. Watts, J. E. Pemberton, and E. L. Ratcliff, "Correlation of Coexistent Charge Transfer States in F 4 TCNQ-Doped P3HT with Microstructure," *Journal of Physical Chemistry Letters*, vol. 9, pp. 6871–6877, 2018.

[182] H. Méndez, G. Heimel, S. Winkler, J. Frisch, A. Opitz, K. Sauer, B. Wegner, M. Oehzelt, C. Röthel, S. Duhm, D. Többens, N. Koch, and I. Salzmann, "Charge-transfer crystallites as molecular electrical dopants," *Nature Communications*, vol. 6, pp. 1–11, 2015.

[183] W. C. Tsoi, D. T. James, J. S. Kim, P. G. Nicholson, C. E. Murphy, D. D. Bradley, J. Nelson, and J. S. Kim, "The nature of in-plane skeleton Raman modes of P3HT and their correlation to the degree of molecular order in P3HT:PCBM blend thin films," *Journal of the American Chemical Society*, vol. 133, pp. 9834–9843, 2011.

[184] N. Kayunkid, S. Uttiya, and M. Brinkmann, "Structural model of regioregular poly(3-hexylthiophene) obtained by electron diffraction analysis," *Macromolecules*, vol. 43, pp. 4961–4967, 2010.

[185] I. E. Jacobs, C. Cendra, T. F. Harrelson, Z. I. Bedolla Valdez, R. Faller, A. Salleo, and A. J. Moulé, "Polymorphism controls the degree of charge transfer in a molecularly doped semiconducting polymer," *Materials Horizons*, vol. 5, pp. 655–660, 2018.

[186] L. Müller, D. Nanova, T. Glaser, S. Beck, A. Pucci, A. K. Kast, R. R. Schröder, E. Mankel, P. Pingel, D. Neher, W. Kowalsky, and R. Lovrincic, "Charge-Transfer-Solvent Interaction Predefines Doping Efficiency in p-Doped P3HT Films," *Chemistry of Materials*, vol. 28, pp. 4432–4439, 2016.

[187] J. E. Cochran, M. J. Junk, A. M. Glaudell, P. L. Miller, J. S. Cowart, M. F. Toney, C. J. Hawker, B. F. Chmelka, and M. L. Chabinyc, "Molecular interactions and ordering in electrically doped polymers: Blends of PBTTT and F4TCNQ," *Macromolecules*, vol. 47, pp. 6836–6846, 2014.

[188] A. Jha, H. G. Duan, V. Tiwari, P. K. Nayak, H. J. Snaith, M. Thorwart, and R. J. Dwayne Miller, "Direct Observation of Ultrafast Exciton Dissociation in Lead Iodide Perovskite by 2D Electronic Spectroscopy," *ACS Photonics*, vol. 5, pp. 852–860, 2018.

[189] V. I. Prokhorenko, A. Picchiotti, S. Maneshi, and R. J. Dwayne Miller, "Broadband electronic two-dimensional spectroscopy in the deep UV," in *Optics InfoBase Conference Papers*, p. 09, Optical Society of America (OSA), jul 2014.

[190] F. D. Fuller and J. P. Ogilvie, "Experimental Implementations of Two-Dimensional Fourier Transform Electronic Spectroscopy," *Annual Review of Physical Chemistry*, vol. 66, pp. 667–690, 2015.

[191] A. Jha, H. G. Duan, V. Tiwari, M. Thorwart, and R. J. Miller, "Origin of poor doping efficiency in solution processed organic semiconductors," *Chemical Science*, vol. 9, pp. 4468–4476, 2018.

[192] D. A. Horke, G. M. Roberts, and J. R. Verlet, "Excited states in electron-transfer reaction products: Ultrafast relaxation dynamics of an isolated acceptor radical anion," *Journal of Physical Chemistry A*, vol. 115, pp. 8369–8374, 2011.

[193] J. Wang, R. M. Wolf, J. W. Caldwell, P. A. Kollman, and D. A. Case, "Development and testing of a general Amber force field," *Journal of Computational Chemistry*, vol. 25, pp. 1157–1174, 2004.

[194] K. Kang, S. Watanabe, K. Broch, A. Sepe, A. Brown, I. Nasrallah, M. Nikolka, Z. Fei, M. Heeney, D. Matsumoto, K. Marumoto, H. Tanaka, S. I. Kuroda, and H. Sirringhaus, "2D coherent charge transport in highly ordered conducting polymers doped by solid state diffusion," *Nature Materials*, vol. 15, pp. 896–902, 2016.

[195] J. Mei and Z. Bao, "Side chain engineering in solution-processable conjugated polymers," 2014.

[196] D. Kiefer, A. Giovannitti, H. Sun, T. Biskup, A. Hofmann, M. Koopmans, C. Cendra, S. Weber, L. J. Anton Koster, E. Olsson, J. Rivnay, S. Fabiano, I. McCulloch, and C. Müller, "Enhanced n-Doping Efficiency of a Naphthalenediimide-Based Copolymer through Polar Side Chains for Organic Thermoelectrics," *ACS Energy Letters*, vol. 3, pp. 278–285, 2018.

[197] B. L. Vallee and R. J. Williams, "Metalloenzymes: the entatic nature of their active sites.," *Proceedings of the National Academy of Sciences of the United States of America*, vol. 59, pp. 498–505, 1968.

[198] R. J. Williams, "Catalysis by metallo-enzymes: The entatic state," *Inorganica Chimica Acta Reviews*, vol. 5, pp. 137–155, 1971.

[199] B. G. Malmström, "Structural control of electron-transfer properties in metalloproteins," *Biology of Metals*, vol. 3, pp. 64–66, 1990.

[200] J. Stanek, A. Hoffmann, and S. Herres-Pawlis, "Renaissance of the entatic state principle," *Coordination Chemistry Reviews*, vol. 365, pp. 103–121, 2018.

[201] P. Comba, "Coordination compounds in the entatic state," *Coordination Chemistry Reviews*, vol. 200-202, pp. 217–245, may 2000.

[202] M. Elias and D. S. Tawfik, "Divergence and convergence in enzyme evolution: Parallel evolution of paraoxonases from quorum-quenching lactonases," *Journal of Biological Chemistry*, vol. 287, pp. 11–20, 2012.

[203] O. Herzberg and J. Moult, "Analysis of the steric strain in the polypeptide backbone of protein molecules," *Proteins: Structure, Function, and Bioinformatics*, vol. 11, pp. 223–229, 1991.

[204] P. Wittung-Stafshede, M. G. Hill, E. Gomez, A. J. Di Bilio, B. G. Karlsson, J. Leckner, J. R. Winkler, H. B. Gray, and B. G. Malmström, "Reduction potentials of blue and purple copper proteins in their unfolded states: A closer look at rack-induced coordination," *Journal of Biological Inorganic Chemistry*, vol. 3, pp. 367–370, 1998.

[205] K. M. Lancaster, S. D. George, K. Yokoyama, J. H. Richards, and H. B. Gray, "Type-zero copper proteins," *Nature Chemistry*, vol. 1, pp. 711–715, 2009.

[206] A. Hoffmann, S. Binder, A. Jesser, R. Haase, U. Flörke, M. Gnida, M. Salomone Stagni, W. Meyer-Klaucke, B. Lebsanft, L. E. Grünig, S. Schneider, M. Hashemi, A. Goos, A. Wetzel, M. Rübhausen, and S. Herres-Pawlis, "Catching an entatic state - A pair of copper complexes," *Angewandte Chemie - International Edition*, vol. 53, pp. 299–304, 2014.

[207] G. Chaka, J. L. Sonnenberg, H. B. Schlegel, M. J. Heeg, G. Jaeger, T. J. Nelson, L. A. Ochrymowycz, and D. B. Rorabacher, "A definitive example of a geometric "entatic state" effect: Electron-transfer kinetics for a copper(ll/l) complex involving a quinquedentate macrocyclic trithiaether - Bipyridine ligand," *Journal of the American Chemical Society*, vol. 129, pp. 5217–5227, 2007.

[208] B. Xie, T. Elder, L. J. Wilson, and D. M. Stanbury, "Internal reorganization energies for copper redox couples: The slow electron-transfer reactions of the [CuII/I(bib)2]2+/+ couple," *Inorganic Chemistry*, vol. 38, pp. 12–19, 1999.

[209] R. D. Hancock and A. E. Martell, "Ligand Design for Selective Complexation of Metal Ions in Aqueous Solution," *Chemical Reviews*, vol. 89, pp. 1875–1914, 1989.

[210] E. W. Dahl and N. K. Szymczak, "Hydrogen Bonds Dictate the Coordination Geometry of Copper: Characterization of a Square-Planar Copper(I) Complex," *Angewandte Chemie*, vol. 128, pp. 3153–3157, 2016.

[211] L. Garcia, S. Maisonneuve, J. Xie, R. Guillot, P. Dorlet, E. Rivière, M. Desmadril, F. Lambert, and C. Policar, "Sugars to control ligand shape in metal complexes: Conformationally constrained glycoligands with a predetermination of stereochemistry and a structural control," *Inorganic Chemistry*, vol. 49, pp. 7282–7288, 2010.

[212] B. Dicke, A. Hoffmann, J. Stanek, M. S. Rampp, B. Grimm-Lebsanft, F. Biebl, D. Rukser, B. Maerz, D. Göries, M. Naumova, M. Biednov, G. Neuber, A. Wetzel, S. M. Hofmann, P. Roedig, A. Meents, J. Bielecki, J. Andreasson, K. R. Beyerlein, H. N. Chapman, C. Bressler, W. Zinth, M. Rübhausen, and S. Herres-Pawlis, "Transferring the entatic-state principle to copper photochemistry," *Nature Chemistry*, vol. 10, pp. 355–362, 2018.

[213] D. R. McMillin, M. T. Buckner, and B. T. Ahn, "A Light-Induced Redox Reaction of Bis(2,9-dimethyl- 1, IO-phenanthroline)copper(I)," vol. 16, pp. 943–945, 1977.

[214] J. Ayache, L. Beaunier, J. Boumendil, G. Ehret, and D. Laub, *Sample Preparation Handbook for Transmission Electron Microscopy*. Springer New York, 2010.

[215] D. V. Scaltrito, D. W. Thompson, J. A. O'Callaghan, and G. J. Meyer, "MLCT excited states of cuprous bis-phenanthroline coordination compounds," *Coordination Chemistry Reviews*, vol. 208, pp. 243–266, 2000.

[216] W. L. Parker and G. A. Crosby, "Assignment of the charge-transfer excited states of bis(N-heterocyclic) complexes of copper(I)," *Journal of Physical Chemistry*, vol. 93, pp. 5692–5696, 1989.

[217] Z. A. Siddique, Y. Yamamoto, T. Ohno, and K. Nozaki, "Structure-dependent photophysical properties of singlet and triplet metal-to-ligand charge transfer states in copper(I) bis(diimine) compounds," *Inorganic Chemistry*, vol. 42, pp. 6366–6378, 2003.

[218] M. Z. Zgierski, "Cu(I)-2,9-dimethyl-1,10-phenanthroline: Density functional study of the structure, vibrational force-field, and excited electronic states," *Journal of Chemical Physics*, vol. 118, pp. 4045–4051, mar 2003.

[219] W. T. Eckenhoff and T. Pintauer, "Bis(2,9-dimethyl-1,10-phenanthroline)copper(I) tetra-phenyl-borate dichloro-methane solvate," *Acta Crystallographica Section E: Structure Reports Online*, vol. 63, 2007.

[220] L. X. Chen, G. B. Shaw, I. Novozhilova, T. Liu, G. Jennings, K. Attenkofer, G. J. Meyer, and P. Coppens, "MLCT state structure and dynamics of a copper(I) diimine complex characterized by pump-probe x-ray and laser spectroscopies and DFT calculations," *Journal of the American Chemical Society*, vol. 125, pp. 7022–7034, 2003.

[221] A. C. Samia, J. Cody, C. J. Fahrni, and C. Burda, "The Effect of Ligand Constraints on the Metal-to-Ligand Charge-Tranfer Relaxation Dynamics of Copper(I)-Phenanthroline Complexes: A Comparative Study by Femtosecond Time-Resolved Spectroscopy," *Journal of Physical Chemistry B*, vol. 108, pp. 563–569, 2004.

[222] M. Iwamura, S. Takeuchi, and T. Tahara, "Real-time observation of the photoinduced structural change of bis(2,9-dimethyl-1,10-phenanthroline)copper(I) by femtosecond fluorescence spectroscopy: A realistic potential curve of the Jahn-Teller distortion," *Journal of the American Chemical Society*, vol. 129, pp. 5248–5256, 2007.

[223] M. Iwamura, S. Takeuchi, and T. Tahara, "Ultrafast Excited-State Dynamics of Copper(I) Complexes," *Accounts of Chemical Research*, vol. 48, pp. 782–791, 2015.

[224] M. Iwamura, H. Watanabe, K. Ishii, S. Takeuchi, and T. Tahara, "Coherent nuclear dynamics in ultrafast photoinduced structural change of Bis(diimine)copper(I) complex," *Journal of the American Chemical Society*, vol. 133, pp. 7728–7736, 2011.

[225] L. X. Chen, G. B. Shaw, I. Novozhilova, T. Liu, G. Jennings, K. Attenkofer, G. J. Meyer, and P. Coppens, "MLCT state structure and dynamics of a copper(I) diimine complex characterized by pump-probe x-ray and laser spectroscopies and DFT calculations," *Journal of the American Chemical Society*, vol. 125, pp. 7022–7034, 2003.

[226] G. B. Shaw, C. D. Grant, H. Shirota, E. W. Castner, G. J. Meyer, and L. X. Chen, "Ultrafast structural rearrangements in the MLCT excited state for copper(I) bis-phenanthrolines in solution," *Journal of the American Chemical Society*, vol. 129, pp. 2147–2160, 2007.

[227] F. Milota, V. I. Prokhorenko, T. Mancal, H. Von Berlepsch, O. Bixner, H. F. Kauffmann, and J. Hauer, "Vibronic and vibrational coherences in two-dimensional electronic spectra of supramolecular J-aggregates," *Journal of Physical Chemistry A*, vol. 117, pp. 6007–6014, 2013.

[228] A. Cohen and J. Kovacevic, "Mathematical Background," *1996*, vol. 84, pp. 514–522.

[229] J. D. Harrop, S. N. Taraskin, and S. R. Elliott, "Erratum: Instantaneous frequency and amplitude identification using wavelets: Application to glass structure [Phys. Rev. E 66, 026703 (2002)]," *Physical Review E*, vol. 68, p. 19904, 2003.

[230] V. der Berg, "Wavelets in Physics," *Cambridge University press*, 1999.

Publication List

○ A. Jha*, H. -G. Duan*, **V. Tiwari**, P. Nayak, H. J. Snaith, M. Thorwart, and R. J. D. Miller, Direct Observation of the Coherent Exciton Dissociation in Lead-iodide Perovskite by 2D Electronic Spectroscopy. ACS Photonics **5**, 852 (2018).

○ A. Jha*, Hong-Guang Duan*, **V. Tiwari**, Michael Thorwart, and R. J. Dwayne Miller, Origin of poor doping efficiency in solution processed organic semiconductors. Chem. Sci. **9**, 4468 (2018).

○ **V. Tiwari***, H.-G. Duan, A. Jha, P. K. Nayak, M. Thorwart, H. J. Snaith and J. Dasgupta, Evidence and implications for exciton dissociation in lead halide perovskites. EPJ Web of Conferences **205**, 06018 (2019).

○ H.-G. Duan*, A. Jha, **V. Tiwari**, R. J. D. Miller and M. Thorwart, Dissociation and localization dynamics of charge transfer excitons at a donor-acceptor interface. Chem. Phys. **528**, 110525 (2020).

○ H.-G. Duan*, **V. Tiwari***, A. Jha*, G. R. Berdiyorov, Z. Li, P. K. Nayak, H. J. Snaith, M. Thorwart, M. E. Madjet and R. J. D. Miller, Photoinduced vibrations driving ultrafast structural distortions in hybrid halide perovskite. JACS **142**, 16569 (2020).

○ H.-G. Duan*, A. Jha*, X. Li, **V. Tiwari**, H. Ye, P. K. Nayak, Z. Li, T. J. Martinez, M. Thorwart and R. J. D. Miller, Intermolecular vibrations mediate ultrafast singlet fission. Sci. Adv **142**, eabb0052 (2020).

Manuscript under preparation:

○ G. Chatterjee*, A. Jha*, A. B. González*, **V. Tiwari**, M. Sugath, H.-G. Duan, V. Prokhorenko, J. Dasgupta, M. Olivucci, R. J. D. Miller, Vibrational excitation initiates biomimetic charge-coupled motions in the electronic ground state. *submitted to Nature Chem.*

○ Y. Yan*, C. Liu, Y. Yang, W. Peng, **V. Tiwari**, A. Jha, H.-G. Duan, F. Tellkamp, Y. Ding, S. Dai, W. Shi, S. Yuan, R. J. D. Miller, W. Ma, J. Zhao, Deprotonation of TiO2 electron transport layer for efficient perovskite solar cells. *under revision.*

○ **V. Tiwari***, X. Li*, Z. Li, H.-G. Duan, I. Jacobs, H. Sirringhaus, A. Jha and R. J. D. Miller, Unraveling bimodal electronic interactions in precursor solutions of molecular doped semiconducting polymer.

○ **V. Tiwari***, A. Jha*, H.-G. Duan, I. Jacobs, H. Sirringhaus and R. J. D. Miller, Direct observation of differential electronic interactions in solution and sequential processed molecular doped semiconducting polymer films.

○ **V. Tiwari***, H.-G. Duan*, A. Jha, Michael Thorwart and R. J. D. Miller, Unraveling the charge separation in PSII reaction center at 20 K by global analysis.

○ **V. Tiwari***, A. Jha, H.-G. Duan, P. K. Nayak, H. J. Snaith, and R. J. D. Miller, Tailored photo-excitations in highly specular perovskite films unraveled by two-dimensional electronic photon-echo spectroscopy.

Erklärung

Die hier vorgelegte Dissertation habe ich eigenständig und ohne unerlaubte Hilfe ange-
fertigt. Die Dissertation wurde in der vorgelegten oder in ähnlicher Form noch bei
keiner anderen Institution eingereicht. Ich habe bisher keine erfolglosen Promotion-
versuche unternommen.

_____

Vandana Tiwari

Hamburg, den 13.10.2020